Numerical Study of Light Confinement with Metallic Nanostructures in Organic Solar Cells

Numerieke studie van lichtopsluiting met metallische nanostructuren in organische zonnecellen

Honghui Shen

Promotoren: prof. dr. ir. B. Maes, prof. dr. ir. P. Bienstman
Proefschrift ingediend tot het behalen van de graad van
Doctor in de Ingenieurswetenschappen: Fotonica

Vakgroep Informatietechnologie
Voorzitter: prof. dr. ir. D. De Zutter
Faculteit Ingenieurswetenschappen en Architectuur
Academiejaar 2011 - 2012

UNIVERSITEIT GENT

ISBN 978-90-8578-529-3
NUR 924, 959
Wettelijk depot: D/2012/10.500/55

Universiteit Gent
Faculteit Ingenieurswetenschappen en Architectuur
Vakgroep Informatietechnologie

Numerical Study of Light Confinement with Metallic Nanostructures in Organic Solar Cells

Numerieke studie van lichtopsluiting met metallische nanostructuren in organische zonnecellen

Honghui Shen

Proefschrift tot het bekomen van de graad van
Doctor in de Ingenieurswetenschappen:
Fotonica
Academiejaar 2011-2012

Promotoren:

Prof. Dr. Ir. Bjorn Maes
Prof. Dr. Ir. Peter Bienstman

Examencommissie:

Prof. Dr. Ir. Daniël De Zutter (voorzitter)	UGent, INTEC
Prof. Dr. Ir. Bjorn Maes (promotor)	UGent, INTEC & UMONS
Prof. Dr. Ir. Peter Bienstman (promotor)	UGent, INTEC
Prof. Dr. Jaime Gomez Rivas	AMOLF & TU/e
Prof. Dr. Ir. Marc Burgelman (secretaris)	UGent, ELIS
Dr. Branko Kolaric	UMONS

Universiteit Gent
Faculteit Ingenieurswetenschappen en Architectuur

Vakgroep Informatietechnologie
Sint-Pietersnieuwstraat 41, B-9000 Gent, België

Tel.: +32-9-264.33.16
Fax.: +32-9-264.35.93

UNIVERSITEIT GENT

Acknowledgements

Time flies!! After almost 4 years at the Photonics Research Group (PRG), Ghent University for my PhD, this dissertation as a period is dedicated to the end of my some 20 years student life.

My PhD years at PRG and this thesis has had guidance and help from several outstanding individuals both from within the group and outside of it. First of all I would like to thank Prof. Björn Maes and Prof. Peter Bienstman for giving me the opportunity to have this PhD position. I want to express my deep gratitude to Prof. Björn Maes for his patience and supervision. Thanks to Prof. Peter Bienstman for his supervision and discussions now and then throughout my PhD years. Without their help none of my results would have seen their DOIs.

I would like to thank all the colleagues involved in the Polyspec project from different universities and institutes. We have had a very good time during the collaborations. Thanks to Bjoern Niesen at imec for discussions and collaborations. I should also mention Prof. Marc Burgelman, Dr. Samira Khelifi, Aimi Abass for their help and discussions.

Hereby I should also thank Barry P. Rand at imec for discussions and help at the beginning of my PhD and David Cheyns at imec for measuring and providing organic materials data.

I would like to express my special thanks to Jeroen Allaert for his endless assistance. Without his help with the servers for COMSOL I would not have had any results. Moreover I thank the colleagues at HPC (high performance computing center) UGent for their help with simulations on the cluster. Thanks to Martin Fiers and Emmanuel Lambert for their help with (Python-) Meep.

I have to say PRG is a really good group with a pleasant atmosphere, it is a big family. I still remember vividly all the activities we have had during these years. Definitely thanks to Prof. Roel Baets. I also want to thank Ilse Van Royen, Kristien De Meulder, Mike Van Puyenbroeck for their assistance. I also thank the colleagues seating in the same office, I have had really good times with all of you.

I would like to thank people from Kaneka at imec for letting me join the Mul-

tihit project, which was working on light trapping for Si thin-film solar cells. I thank the people involved in this project, Ichikawa Mitsuru, Ivan Gordon, Andrea Feltrin and so on, for their help and discussions.

I would like to thank people from UMONS for giving me the opportunity to work with them.

Without my beloved and lovely Chinese friends, I could not have had such a memorable time during the 4 years at Ghent. Thanks to all the Chinese friends whom I have had a wonderful time with. I am thinking of the unforgettable travels and parties with card games, video games, food and so on.

In addition, I thank my parents and sister for their understanding, support and encouragement.

And yes, thank you...

Ghent, April 2012
Honghui Shen

Table of Contents

List of Figures

List of Acronyms

B

BHJ	Bulk Heterojunction

C

CdTe	Cadmium Telluride
CIS or CIGS	Copper Indium Gallium Selenide
CuPc	Copper Phthalocyanine

D

D-A	Donor-Accepter
DSSC	Dye-Sensitized Solar Cell

E

EOT	Extraordinary Optical Transmission

F

FDTD	Finite Difference Time Domain
FEM	Finite Element Method
FP	Fabry-Perot

H

HOMO	Highest Occupied Molecular Orbital

I

ICBA	Indene-C_{60} Bisadduct
ITO	Indium Tin Oxide
I-V	Current-Voltage

L

LSP	Localized Surface Plasmon
LUMO	Lowest Unoccupied Molecular Orbital

M

MIM	Metal-Insulator-Metal
MNP	Metallic Nanoparticle

N

NP	Nanoparticle

O

OSC	Organic Solar Cell

P

PCBM	[6,6]-phenyl-C_{61} butyric acid methyl ester
$PC_{70}BM$	[6,6]-phenyl-C71-butyric acid methyl ester
PCPDTBT	Poly[2,6-(4,4- bis-(2-ethylhexyl)-4H-cyclopenta[2,1-b;3,4-b'] dithiophene)-alt-4,7-(2,1,3- benzothiadiazole)]
P3HT	Poly(3-exylthiophene)
PEDOT	Poly(3,4-ethylenedioxythiophene):poly(styrenesulfonate)
PML	Perfectly Matched Layer
PPV	Poly(Phenylene Vinylene)
PSBTBT	Poly[(4,40-bis(2-ethylhexyl)dithieno[3,2-b:20,30-d] silole)-2,6-diyl-alt-(2,1,3-benzothiadiazole)-4,7-diyl]
PV	Photovoltaics

S

SPP	Surface Plasmon Polariton
SubPc	Chloro [subphthalocyaninato] Boron

T

TE	Transverse Electric
TM	Transverse Magnetic

U

UV	Ultraviolet

Z

ZnPc	Zinc Phthalocyanine

Nederlandse samenvatting –Summary in Dutch–

Organische zonnecellen hebben een sterk potentieel in vergelijking met anorganische zonnecellen, omdat ze de mogelijkheid hebben tot fabricage van goedkope, lichtgewicht componenten. Echter, belangrijke problemen zoals de relatief lage efficiëntie en stabiliteit moeten aangepakt worden. Momenteel bedraagt het efficiëntie record 10.6% (Yang Yang lab, UCLA). Deze efficiëntie wordt sterk gelimiteerd door de korte exciton diffusie lengte in organische materialen, typisch van de orde 10nm. Deze diffusie lengte is veel kleiner dan de licht absorptie lengte, van de orde 100–200nm. Dit leidt tot een belangrijke afweging tussen optische en elektronische eigenschappen. Het is bijgevolg een uitdaging om zoveel mogelijk licht te absorberen in een zo dun mogelijke laag. Dit betekent dat nanofotonische opsluitingstechnieken voor licht een belangrijke rol kunnen spelen.

Een grote verscheidenheid aan opsluitingstechnieken wordt momenteel theoretisch en experimenteel onderzocht: gevouwen structuren, fotonische kristallen, nanodeeltjes, roosters etc. Binnen de context van dit werk, dat zich kaderde in het IWT-SBO PolySpec project, focusten we op metallische nanostructuren, omdat deze elementen zeer compact zijn, en compatibel lijken met de relatief dunne organische zonnecellen. Hier berichten we over onze numerieke resultaten die handelen over het gebruik van metallische structuren om de absorptie in organische zonnecellen te verbeteren.

Licht-opsluitingstechnieken zorgen ervoor dat het zonlicht gekoppeld wordt naar optische modes, zodat de optische weglengte vergroot, hetgeen leidt tot een langer ‘verblijf’ in het absorberende materiaal en dus een grotere kans op absorptie. Metallische structuren genereren speciale modes, ‘plasmonische’ modes, die men kan opsplitsen in twee soorten: gelokaliseerde en propagerende plasmonen. De lokale plasmonen zijn geassocieerd met zeer lokale excitaties, zoals rond nanodeeltjes. De propagerende plasmonen komen voor bij oppervlakken, waarlangs de mode propageert. Beide soorten modes creëren hoofdzakelijk twee effecten: grotere nabije velden en een sterkere diffusie van het licht. Beide effecten worden gebruikt bij de plasmonische opsluitingstech-

nieken in dit werk.

Metallische nanodeeltjes

Metallische deeltjes kunnen lokale plasmonen exciteren, die mogelijks leiden tot sterke diffusie of versterking van het nabije-veld. Men vindt bv. via Mie theorie dat voor kleine deeltjes (diameter kleiner dan 30nm) het nabije-veld effect domineert. Voor grotere deeltjes (meer dan 50nm) wordt diffusie belangrijker. Voor nog grotere deeltjes kan men tevens hogere orde modes waarnemen. De verschillende regimes impliceren verschillende toepassingen. Sterke diffusie kan gebruikt worden om licht te heroriënteren in een meer horizontale richting. De versterkte nabije-velden zorgen voor een lokale vertraging van het licht.

Het nabije-veld kan in principe op twee manieren gebruikt worden, men kan de deeltjes in of net naast de actieve laag positioneren, bv. in een nabije PEDOT:PSS bufferlaag, zodat het veld voor een deel koppelt naar de eigenlijke actieve laag. Onze berekeningen tonen dat kleine deeltjes in de bufferlaag (kleiner dan 30nm) geen absorptie voordeel opleveren. Dit komt inderdaad omdat diffusie zeer klein is, en omdat het nabije-veld zich hoofdzakelijk in de zijwaartse richting uitstrekt, met slechts een kleine, exponentieel krimpende component in de actieve laag. Slechts voor zeer dunne lagen kan dit effect nuttig zijn, zeker wanneer er interactie met een metallische elektrode mogelijk is aan de andere kant van de actieve laag.

Vele experimenten in de literatuur gebruiken deeltjes met grootte-orde 10nm, die dus enkel optisch effectief kunnen zijn binnenin de actieve laag. Onze simulaties wijzen inderdaad op een dergelijk potentieel, met een versterking van de absorptie met een factor 1.5–1.7, echter met de voorwaarde dat de actieve laag zeer dun is, grootte-orde 30–50nm. Optisch gezien moeten de deeltjes relatief dicht bijeen zitten, hetgeen moeilijk is voor de elektronische eigenschappen. Dit elektronisch probleem kan verzacht worden via een coating rond de deeltjes, om exciton-recombinatie te verminderen. Simulaties tonen dan weer dat dit het absorptie-potentieel snel vermindert. Sommige artikels wijzen er echter op dat bepaalde aanpassingen deze afweging mogelijks minder streng maken.

Een andere techniek gebruikt de versterkte diffusie bij plasmonische resonanties van relatief grotere deeltjes. We bestudeerden dergelijke deeltjes aan het bovenste oppervlak van de zonnecel, hetgeen inderdaad kan leiden tot diffusie in de actieve laag. Verdere verbeteringen zijn mogelijk door de ruimte tussen de deeltjes met een geschikt medium te vullen. Een stroom-toename met een factor 1.12 is hiermee mogelijk.

Aan de start van dit werk was het onduidelijk welke metalen het meest nuttig zijn. Zilver en goud waren de klassieke kandidaten, en het meest bekend

voor fabricage. In dit werk werd vooral Ag, Al en Au onderzocht. Zilver heeft interband transities (en dus een sterke absorptie) slechts bij kleinere golflengtes, zodat een grote bandbreedte beschikbaar is. Plasmonische modes kunnen bovendien voorkomen van 350nm tot in het infrarood, en deze resonanties zijn goed regelbaar. Goud heeft transities rond ~ 330nm en ~ 470nm, en de modes worden geëxciteerd bij golflengtes groter dan 500nm. Bij de meeste metalen geldt dat de absorptie beneden de resonantie-golflengte belangrijk is. Aluminium heeft aanvaardbare verliezen in het zichtbare gebied, maar heeft grotere verliezen dan Ag en Au voor grotere golflengtes. De plasmonische resonantie is dan weer in het ultra-violet gebied. Numerieke studies tonen aan dat zowel Al als Ag deeltjes leiden tot vergelijkbare absorptie toenames, terwijl Au teveel absorptie-verliezen vertoont.

Gecombineerde roosters

Behalve deeltjes kunnen roosterstructuren ook zorgen voor plasmonische licht-opsluiting. Vele verschillende structuren zijn onderzocht: 2D roosters met gaten of uitstulpingen aan het reflecterende achter-contact, roosters aan de voorzijde van de cel etc. Dergelijke roosters kunnen leiden tot een preciezere en gemakkelijkere fabricage, vergeleken met deeltjes-technologie, waar clustering een vaak voorkomend probleem vormt. Tevens wordt de actieve laag minder verstoord bij roosters, dan wanneer men deeltjes in de laag zelf mengt. Om deze redenen hebben we het potentieel van roosters grondig onderzocht.

Verscheidene optische effecten zijn beschikbaar in roosters: koppelen naar gelokaliseerde of propagerende plasmonen, koppelen naar traditionele 'fotonische' golfgeleider modes, diffractie etc. Hun respectievelijke contributies hangen sterk af van materiaal- en rooster-parameters. Voor kleine rooster-periodes (<300nm) zijn lokale plasmon modes het belangrijkst. Mode-koppeling wordt mogelijk bij grotere periodes, waarbij de specifieke resonantie bepaald wordt door de periode en de Bloch-mode dispersie. De plasmon modes in dit geval hebben vaak hybride eigenschappen, zowel lokale als propagerende karakteristieken zijn merkbaar, en beide kunnen leiden tot sterkere absorptie.

Om deze modes ten volle te gebruiken, hebben we een gecombineerde structuur geïntroduceerd, met zowel een rooster aan de voorzijde, als een rooster-elektrode aan de achterzijde. In plaats van de roosters exact boven elkaar uit te lijnen, blijkt het beter om een horizontale afwijking te gebruiken, hetgeen een meer onafhankelijke superpositie van modes (en dus absorptie) bewerkstelligt. De berekeningen concluderen dat de gecombineerde structuur beter werkt dan de enkele roosters. Opnieuw moet een dunne actieve laag (50nm) gebruikt worden, zodat men een vergelijkbaar potentieel bekomt als bij de deeltjes, maar met minder verstoring van het absorberende materiaal.

De mode-koppeling is, zoals vermeld, sterk afhankelijk van de dispersie en dus van de band-structuur, hetgeen interessante gevolgen heeft voor de absorptie-afhankelijkheid van de licht-invalshoek. Het bestaan van symmetrische en asymmetrische modes speelt hierbij een belangrijke rol. Asymmetrische modes zijn namelijk enkel beschikbaar voor niet-loodrechte lichtinval. Berekeningen tonen aan dat deze extra modes kunnen zorgen voor een absorptie-versterking die zich over een groter hoekbereik uitstrekt.

Om de polarisatie-afhankelijkheid te verminderen van voorgaande structuren, hebben we tevens 2D roosters onderzocht. Roosters met nano-schijven in Ag geïntegreerd in een bufferlaag leiden hier ook tot een toename van de stroomsterkte, met een factor van ongeveer 1.2.

Roosters met graduele openingen

Het effect genaamd buitengewone optische transmissie (Extraordinary Optical Transmission–EOT) werd geobserveerd in 1998 doorheen een metallische film met een rooster van sub-golflengte gaten. Gelijkaardige fenomenen werden waargenomen in roosters met lineaire spleten. EOT biedt de mogelijkheid van versterkte lokale velden, gekoppeld met een belangrijke transmissie. Echter, door het resonante caviteits-effect gekoppeld aan spleten, bekomt men vaak een beperkte bandbreedte, hetgeen ongunstig is voor bepaalde applicaties zoals zonnecellen.

In dit werk stellen we roosters voor met graduele, 'getaperde' spleten bij TM polarisatie. Doordat de impedantie doorheen deze structuren geleidelijk aan verandert, verdwijnen de caviteits-effecten, hetgeen leidt tot een niet-resonante, breedbandige transmissie, zowel voor golflengte als voor invalshoek. Rigoureuze berekeningen en een transmissielijn-model beschrijven het proces in detail. Bovendien is de veld-lokalisatie beperkt tot het uitgangsvlak, nabij de scherpe hoeken, hetgeen ook contrasteert met de klassieke, rechtwandige structuren. Dit type roosters kan bijgevolg nuttig zijn voor niet-lineaire optica, licht absorptie, sensors, emissie etc. De transmissie neemt verder toe bij toename van de invalshoek, door wisselwerking met een plasmonisch Brewster-type effect. Tevens werd een polarisatie-onafhankelijke 2D versie berekend met gekruiste spleten, waarbij het graduele effect behouden blijft.

English summary

Organic solar cells (OSCs) enjoy a strong potential compared to inorganic solar cells, because of the possibility of low-cost fabrication of lightweight, large-area devices. However, important issues such as low efficiencies and stability need to be addressed. So far the highest efficiency achieved for OSCs is 10.6% by Yang Yang Laboratory at the University of California, Los Angeles. The low efficiency limitation is mainly imposed by the short exciton diffusion length (in addition to other material properties such as the large bandgap of polymers) in organic materials, which is typically around 10nm. This diffusion length is much smaller than the light absorption length in organic materials, usually 100–200nm. Therefore there is an important tradeoff between optical and electronic properties, leading to the challenge to absorb as much light as possible in an active layer as thin as possible. To achieve this, nanophotonic light trapping schemes offer help.

A number of light trapping schemes have been proposed and investigated theoretically and experimentally, such as folded structures, photonic crystals, metallic nanoparticles, periodic metallic gratings etc. The IWT-SBO Polyspec project, which was the context for this work, focused on the use of metallic nanostructures, as these elements tend to be very compact, and seem at first sight compatible with OSCs. Here we summarize our numerical findings on the use of metallic nanostructures to enhance light absorption in OSCs.

In essence, light trapping means that the incoming sunlight is coupled to optical modes which enhance the 'path length' of the light, thus the light stays longer in the absorbing layer and has a larger chance to be absorbed. Metallic structures generate modes, called 'plasmonic modes', which can, in general, be classified into two categories: localized surface plasmons (LSPs) and propagating surface plasmon polaritons (SPPs). The former are associated with very local excitations, such as around nanoparticles. The latter are associated with surfaces, along which a mode can propagate. Both LSPs and SPPs create mainly two effects: enhanced near-fields and enhanced scattering of light. Both features are exploited in the plasmonic light-trapping schemes discussed here.

Metallic nanoparticles

Metallic nanoparticles (MNPs) tend to excite LSPs, with possibly a very strong scattering or near-field enhancement. From Mie theory one finds that for particles with size smaller than around 30nm, the near-field enhancement dominates. For particles with size larger than 50nm the scattering effect is more significant. For even larger particles with size comparable to the wavelength retardation will come into effect, so that higher order modes can be excited.

The different size regimes point to two different ways to take advantage of LSPs. First, the strong scattering can be used to redirect light more horizontally into the active layer. Second, we can use enhanced near-fields, so that light spends more time around a particle.

For utilization of the enhanced near-fields, this leads to two schemes to exploit the near-field effects: embedding nanoparticles inside or outside the active layer. When the particles are not inside the active layer, they are most often integrated immediately next to it, usually the PEDOT:PSS buffer layer. In this way the near-field can couple into the active layer. In the end, our calculations show that this configuration provides no absorption enhancement for small particles (size smaller than 30nm). Indeed, scattering is negligible, and the near-field enhancement is mainly localized in the lateral direction, decaying rapidly into the active layer. An effective decay distance is roughly 0.26 times the radius of the particle. For thinner active layers, this may still be useful, especially when the particles can couple to a metallic back-contact on the other side of the active layer.

In many experiments the particles in OSCs have a size on the order of 10nm, thus these can only be effective when incorporating inside the active layer. There are some recent reports about embedding silver nanoparticles directly or partially into the active layer. Our numerical studies both for metallic nanowire and spherical MNPs verified the optical potential. This type of configuration can lead to an absorption enhancement factor around 1.5–1.7, however provided that the active layer is very thin, about 30–50nm thick. The optical optimum means that the particles are quite close to each other, which is not promising from the electronic point-of-view. To alleviate this problem, one can consider coatings around the nanoparticles, in order to reduce exciton quenching. However, this coating has a very strong negative influence on the absorption enhancement, as the near-field will contribute less to absorption in the active layer. Note that it has been reported that some coatings with larger effective indices can reduce this problem, so some engineering may be possible.

Another light-trapping approach with MNPs is to employ them as scatterers, which takes advantage of the enhanced scattering via plasmonic excitations in larger nanoparticles. We examined MNPs as scatterers on the top surface of

OSCs (with 100nm thick active layer), which can effectively scatter light into the active layer. Further improvement is achieved by filling the space between the particles with a certain medium (with refractive index 1.41). A modest current density enhancement around 1.12 is achievable.

At the onset of this work, it was not clear which metal could prove most useful for plasmonic devices. In the literature silver and gold appear the most promising candidates, and the most straightforward for fabrication. In this work we performed studies for three metals: Ag, Al and Au. Ag has interband transitions (leading to absorption losses) only for low wavelengths around 300nm. This means that at higher wavelengths the losses for silver are relatively small. In addition, plasmonic modes can be generated across the spectrum starting from around 350nm to the infrared range. The resonances are tunable by changing size, shape and the surrounding material of the particles. Gold has two interband transitions at ~330nm and ~470nm and the modes are always excited at wavelengths larger than 500nm. In addition, most metals will offer a large absorption in the wavelength range below the plasmonic resonance. Al has lower loss in the visible light range, however the loss in Al overrides Ag and Au at larger wavelengths. Meanwhile the plamonic modes for Al tend to be in the ultraviolet (UV) range. Finally, our numerical studies with spherical MNPs in the active layer showed that Al and Ag lead to a comparable absorption and current density enhancement. In contrast, Au gives a small enhancement because its LSP tends to be excited at larger wavelengths, while a large loss in Au particles is observed due interband transitions.

Combined gratings

Besides the configurations mentioned above, the corrugated surfaces or gratings can also be used as plasmonic light trapping structures. Many different gratings have been investigated, such as 2D square lattice arrays of nanoholes on the back contact, rectangular/triangular gratings on the back contact, and gratings on the front side of solar cells. Compared with the light trapping schemes using metallic nanoparticles, grating structures may be easier to fabricate and to control the size and structure by nanofabrication technology. In the nanoparticle case, aggregation e.g. is a common problem, often leading to a negative impact on the absorption enhancement. In addition, grating device fabrication can lead to unharmed active layers, which is in stark contrast with mixing of particles into the layer. For these reasons we have strongly investigated the grating potential.

With gratings a variety of phenomena are available: coupling to plasmonic modes (LSPs or SPPs), coupling to the more traditional 'photonic' waveguide modes, diffraction etc. The contribution of these effects depends strongly on

the material and grating parameters. For small periods (<300nm) localized plasmonic modes are the main factor for the light harvesting improvement. Since the period is so small there is only the specular zero-order 'diffracted' mode. Therefore the light cannot be coupled to lateral direction modes, such as SPPs or waveguide modes, because of the mismatch of momentum. Scattering into propagating surface plasmon modes comes into effect for larger grating periods. The position of the resonances is strongly influenced by the period and the Bloch mode dispersion. At the same time these propagating modes can have a more localized character, especially when nano-scale features are involved. In the end, the localized and propagating modes contribute to a potentially significant absorption enhancement.

Here to make full use of LSPs and SPPs, we proposed a combined grating composite of a 1D front (on top of active layer) and back (integrated with reflector) grating. We include a lateral (half period) offset, targeting independent, but superimposed enhancements. Simulations show that indeed the combined grating offers more absorption enhancement than a single grating case. A mixed character of the LSP and SPP modes is observed, contributing to the spectral absorption enhancement. Again, the thickness of the active layer was limited (50nm) in these studies, leading to a similar enhancement potential as with particles inside the active layer, but without disturbing the absorbing material so strongly.

Since a grating is a periodic structure, it can couple the sunlight into laterally propagating modes, which one explains via calculating the band structure. This complex band structure plays an important role in the angular response of the solar cell. In our work with combined gratings we discuss this response in detail. Two different symmetry modes exist in the grating structure, i.e. bright and dark plasmonic Bloch modes. Because of the net dipole moment along the interface, only the bright mode can be exited with normal incident light, while the dark mode can only be excited with tilted incident light. Our simulations show that the modal interplay even makes it possible to obtain larger absorption enhancement at an angle deviating from normal incidence.

The polarization dependence has a strong influence on the light absorption enhancement, especially for 1D gratings, as the plasmonic modes only correspond to Transverse Magnetic (TM) polarized light. Therefore, the behavior for Transverse Electric (TE) polarization is often less effective. This negative effect can be overcome provided that the period of the grating and the thickness of the active layer are large enough to support guide modes in the solar cell structure. Another solution is to use 2D gratings with sufficient symmetry for polarization independence. Therefore we have investigated OSCs with 2D Ag nanodisk arrays integrated into a buffer layer, where a considerable current density enhancement factor around 1.2 was observed.

Gratings with tapered slits

The extraordinary optical transmission (EOT) phenomenon was first observed in an opaque metallic film with a periodic array of subwavelength holes in 1998. Later on similar phenomena were observed in metallic gratings with linear slits. EOT offers strongly localized field enhancements, in addition to a large transmission. However, due to the resonant Fabry-Perot (FP) mechanism involved in structure with slits, often a relatively narrow bandwidth is affected, which is unsuitable for some applications.

In our work, we propose metallic gratings with tapered slits for TM polarized light, which offers a much broader transmission window. By gradually varying the impedance from input to output plane, we effectively destroy the FP type resonant conditions of plasmonic modes in the slit, yielding a non-resonant and thus broadband and wide-angle large transmission in the infrared. We attribute this transmission to the impedance matching between the tapered slit entrance and surrounding. This can be explained well by a transmission line model. In addition, the localization of the field is confined to one plane of the structure, instead of over the whole lossy waveguide as in the traditional structures with straight sidewalls. This could be useful for applications such as nonlinear optics, light harvesting, sensing, emission enhancement etc. The transmission at smaller wavelengths is further improved by tilting the incident light, giving rise to a plasmonic Brewster type effect. Finally, we demonstrated a polarization independent 2D grating with normally crossing slits, where we show that the tapering effects remain valid.

1 Introduction

1.1 World energy consumption

Entering the 21th century with an increasing world population of around 7 billion we are faced with a bundle of global challenges, such as how to realize a sustainable development for both economics and societies. How to develop the economy with depletable resources and environmental protection is a primary problem. In this development energy problems remain a principle preoccupation of not only developing countries, where energy demands increase quickly, but also of the developed countries.

The operation of our modern industrial civilization is wholly dependent on a large amount of energy of various types. Fig. 1.1 shows the world energy consumption measured in quadrillion Btu (quad) from the international energy outlook by the U.S. Energy Information Administration [1]. World energy consumption keeps increasing, and in 2008 it amounted to 504.7 quad (~ 532.5EJ). Fossil fuels (liquids, coal and natural gas) were always and are still the most popular energy type. The usage of fossil fuels in 2008 were (estimation based on data in [1]): 1) Liquids (173 quad): 53.48% goes to transportation, 32.56% to industry, 8.14% to buildings, 5.82% to electricity; 2) Coal (139 quad): 60% to electricity, 36% to industry, the rest to residential and commercial sectors; 3) Gas (114.3 quad): 35.6% to electricity, 29.3% to industry, the rest to others (eg. residential). Therefore in summary, fossil fuels are mainly used in transporta-

tion (~92.5 quad), electricity generation (~134.1 quad) and for industry (~130.1 quad).

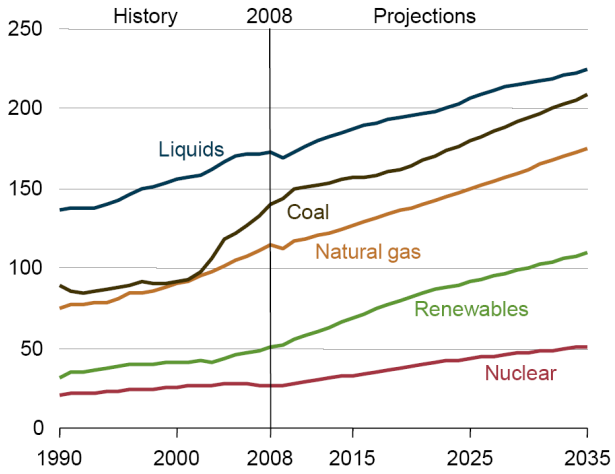

Figure 1.1: World energy consumption: past and outlook [1]. In 2008, liquids: 173 quad, coal: 139 quad, gas: 114.3 quad, renewable: 51.3 quad, nuclear: 27.2 quad. Liquids include the crude oil, coal-to-liquid, and others transformed from other fuels, renewable includes hydropower, wind, biomass, solar and so on. (Unit: quadrillion Btu (quad). $1quad = 1.055EJ = 1.055 \times 10^{15} J$).

As known the price of fossil fuels keeps increasing since they were formed many hundreds of millions of years ago and are non renewable resources with limited amount. Meanwhile an environmental issue with fossil fuels is that they are the main source of greenhouse gas emissions, eg. 90% gas emission in United States is from the use of fossil fuels, and produce many other pollutants like nitrogen oxides, sulfur dioxide, heavy metals, ash and so on. Therefore to tackle the high price of fossil fuels and environmental issues, renewable energy receives more and more attention, government support and preferential policies because they are clean and environmentally friendly. As projected in Fig. 1.1 the amount of renewable energy will increase rapidly in the following decades.

Electricity is not only an important part of our modern daily life, it also plays a significant role for modern industries. As shown in Fig. 1.2, in 2008 world net electricity generation was about 19.1PWh (~ 68EJ) with 12.9PWh by fossil fuels, 3.7PWh by renewable energy and 2.6PWh by nuclear. Hydroelectricity and wind are the two largest contributors to the increase in global renewable electricity generation, with hydropower accounting for 55% of the total increment and wind 27% [1]. Electricity from solar energy is currently a small portion,

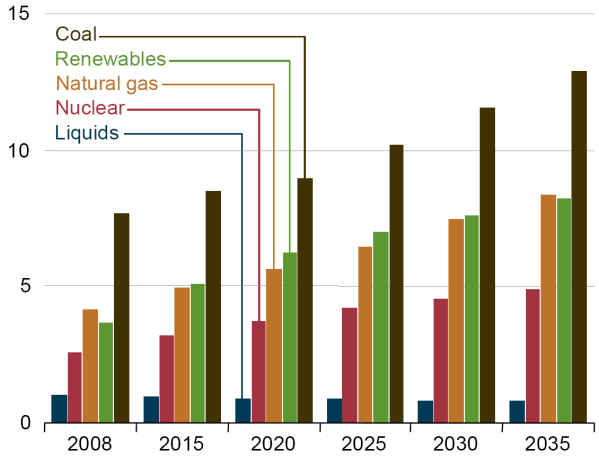

Figure 1.2: World net electricity generation by fuel type [1]. (Unit: PWh. $1PWh = 3.6EJ = 3.412quad$).

about 0.013PWh (0.047EJ). However, solar energy is a plentiful, ceaseless and clean supply, and therefore one of the promising renewable power sources. In fact the sun delivers around 3.85 million EJ energy to the earth yearly. More precisely the sun can meet the world energy consumption in 2008 just within around one hour.

One of the attractive technologies utilizing solar energy is the photovoltaic technology. Photovoltaic technology has many strong points: direct conversion of solar energy into electricity, no noise during generation, no high temperature, no pollution and so on [2]. By developing sophisticated photovoltaic technology, the sun can offer abundant electricity, so that we do not have to use other methods leading to greenhouse gas emissions. Furthermore, solar energy can also replace fossil fuels used in other applications (eg. replace liquids for transportation). A bright future would be when fossil fuels are only used as material resources instead of as energy resources.

1.2 Photovoltaics

1.2.1 Solar cell principles and characteristics

Photovoltaics (PV) is a technology capable of converting solar energy into electricity directly by devices called photovoltaic cells (also known as solar cells (SCs)) and is based on the photovoltaic effect. The conventional (crystalline

silicon) solar cells[1] typically consist of a p-n junction (formed by p- and n-type semiconductors into contact) with a single bandgap E_g where voltages are developed by absorbing light.

Figure 1.3(a) shows the energy-band diagram for a single p-n junction solar cell. When light illuminates the cell, photons with energy $h\nu$ (ν is the frequency and h is the planck constant) larger than the bandgap will be absorbed. Note that not all of the light that satisfies the energy requirement ($h\nu > E_g$) is completely absorbed, its absorption characteristic is determined by the intrinsic absorption coefficient and the thickness of the semiconductor. Meanwhile excess energy of the absorbed photon is wasted as heat due to thermalization in the conduction band. By absorbing a photon an electron in the valence band is excited into the conduction band, leaving a hole behind and creating an electron-hole (e-h) pair. These free carriers, e and h, will be swept across the junction by the electric field, collected at the electrodes and can power the external load. The electron and hole will transport in the n- and p-type semiconductor, respectively. During transport to the electrodes recombinations are possible which will reduce the photocurrent.

Therefore the photovoltaic process in solar cells is generally divided into four steps: light absorption, charge generation, charge transport and charge collection. An efficiency can be defined to qualify each step. The product of these four efficiencies yields the external quantum efficiency (η_{EQE}), whereas the product of them excluding the absorption efficiency is the internal quantum efficiency (η_{IQE}). For a good cell the η_{EQE} should be as large as possible by engineering each step.

For solar cells the most important measure for their performance is how much current and voltage they can supply. This can be estimated from the relationship between current and voltage, the current-voltage (I-V) characteristic (also known as I-V curve). The I-V curves of solar cells are complex. Ideally the I-V curve with illumination can be derived from solid state physics. It is given by [3]:

$$I = I_0 \left(\exp\left(\frac{V}{V_T} \right) - 1 \right) - I_L \tag{1.1}$$

where V_T is the thermal voltage with a constant value of kT/q, I_L is the photocurrent and is identical to the short-circuit current (I_{SC}), I_0 is the ideal reverse saturation current. The first term on the right represents the current without illumination.

Figure 1.3 (b) shows the typical I-V curve. From this figure we can extract several important parameters to characterize solar cell performance: the open-circuit voltage V_{OC}, the short-circuit current I_{SC}, the maximum power output

[1] The operational principle of organic solar cells is similar, however differences are explained in section 1.3.1.

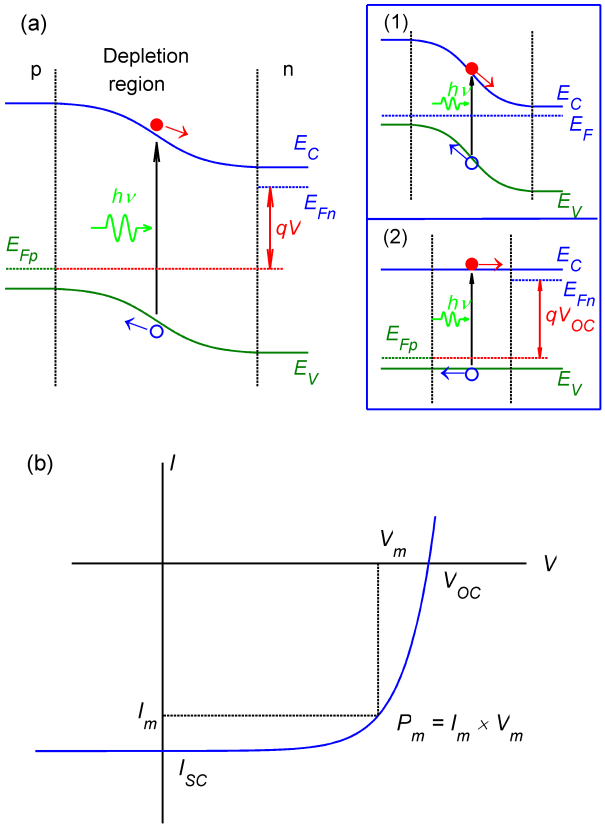

Figure 1.3: (a) Energy-band diagram of a single pn junction solar cell. Photons with energy $h\nu$ larger than the bandgap E_g ($= E_C - E_V$) can be absorbed and generate an electron-hole pair. The insets (1) and (2) show the diagrams for short and open circuit cases. (The electrodes are not shown. The anode should attach to p-type semiconductor, while cathode to n-type.) (b) Typical current-voltage ($I-V$) characteristics of solar cells. I_{SC} is the short-circuit current, V_{OC} is the open-circuit voltage. While V_m and I_m are the voltage and current with maximum output power P_m.

P_m, and the filling factor FF. The maximum power output P_m is achievable with an appropriate external load. The open-circuit voltage V_{OC} is the available maximum voltage of solar cells and qualitatively the built-in potential of the p-n junction. It is somewhat smaller than the bandgap, as seen in Fig. 1.3 (a). Therefore using semiconductor materials with large bandgap can increase the V_{OC}, however the photocurrent will decrease since a larger E_g limits the light absorption. The short-circuit current I_{SC} is the current when the external circuit is shorted by an ideal conductor. It can be directly calculated by integrating the photogenerated charges under solar irradiance, and is given by

$$I_{SC} = A \cdot J_{SC} = \frac{Ae}{hc} \int \lambda \eta_A(\lambda) S(\lambda) d\lambda \tag{1.2}$$

where A is the area of the electrode in contact with the semiconductor, $S(\lambda)$ is the solar irradiance spectrum, $\eta_A(\lambda)$ is the absorption spectrum of the active layer in the solar cell, and e is the elementary charge (1.6×10^{-19} C). Instead of I_{SC}, the short circuit current density J_{SC} is commonly used since it is independent of the area A. The filling factor FF is the ratio of P_m to the product of I_{SC} and V_{OC}:

$$FF = \frac{V_m \cdot I_m}{V_{OC} \cdot I_{SC}}. \tag{1.3}$$

For a good conventional solar cell a filling factor as high as 80% can be achieved.

The power conversion efficiency is the most important figure of merit, defined as the ratio of photo-generated electric output power to the total incident power on the solar cell. It is given by

$$\eta = \frac{P_m}{P_{in}} = \frac{V_m \cdot I_m}{P_{in}} = \frac{FF \cdot V_{OC} \cdot I_{SC}}{P_{in}}. \tag{1.4}$$

The total power (also called intensity) of incident light P_{in} is given by the integration of the solar spectrum over all wavelengths:

$$P_{in} = \int S(\lambda) d\lambda. \tag{1.5}$$

Eq. 1.4 reveals that the efficiency of a solar cell is influenced by both I_{SC} and V_{OC}, and both are influenced by the semiconductor bandgap. The ideal maximum efficiency achievable for a single junction solar cell with optimized bandgap is ~31% under the AM 1.5G illumination condition with 1 sun at 300K [3].

From Eqs. 1.2 and 1.4 one can see that both the short circuit current and power conversion efficiency are dependent on the light intensity and its irradiance spectrum. Therefore different light sources will result in different characteristics of the solar cell. To have a comparison between different solar cells, a standard light source is need defined. The global air mass 1.5 (AM 1.5G)

spectrum is the commonly used solar irradiance for solar cell characterization (shown in Fig. 1.4). It has a total intensity of 100mW/cm^2 when integrated across the whole solar spectrum.

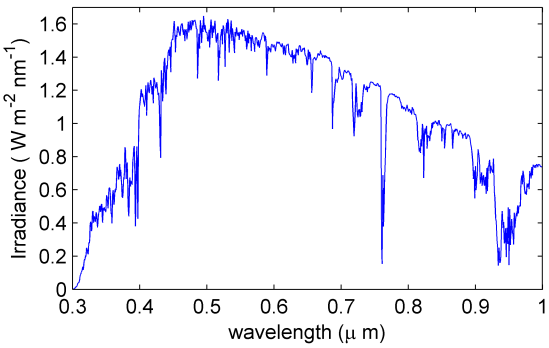

Figure 1.4: AM 1.5G solar irradiance spectrum.

1.2.2 Solar cell generations

The photovoltaic effect was first discovered by Becquerel in 1839 [4] in a junction formed between an electrode and an electrolyte. Since then many efforts have been dedicated to investigate other materials and improve the efficiencies of solar cells. However the efficiencies remained low, until 1954 when there were two breakthroughs. Chapin *et al.* at Bell Laboratories developed the first silicon solar cells with a large efficiency [5], whereas Reynolds *et al.* at Aeronautical Research Laboratory demonstrated cadmium sulfide cells with short circuit currents of 15mA/cm^2 and open circuit voltages of 0.4V under direct sunlight [6]. Over the last 50 years solar cells have received tremendous improvements. To date, solar cells have reached a record efficiency of 28.3% for a single junction cells [7] and 43.5% for multi-junction cells [8]. Since the first Si cell in 1954 solar cells have experienced three generations regarding the materials and technologies used [9].

The first generation solar cells, also called conventional solar cells, are made from silicon, like crystalline silicon (c-Si), multicrystalline silicon (mc-Si) and ribbons. They are currently very efficient and the most dominant solar cells available in the market. In 2009 this kind of solar cells was responsible for around 75% of the worldwide solar cell production. However as known Si is a weakly absorbing material (due to its indirect band gap) so the crystalline silicon wafer based solar cells are always very thick, about 180-300μm. Meanwhile Si crystals are expensive and slow to grow due to the production process.

Therefore the cost of first generation solar cells remains high. Moreover, they are fragile and heavy.

The second generation of solar cells usually refers to thin-film solar cells, which are mainly made from three different semiconductor materials including amorphous silicon (a-Si), cadmium telluride (CdTe) and copper indium gallium selenide (CIS or CIGS). Compared with c-Si based solar cells, thin-film solar cells are at least 100 times thinner, which make them very light so they are deposited on a (possibly flexible) substrate for mechanical support. They can be produced on a much larger scale with no requirement for high temperature processes (~ 200°). As a consequence they have attractive properties over c-Si and are eventually much cheaper, which to some extent can balance the lower efficiency of thin-film solar cells.

Most of the third generation solar cells are in the research phase, and also belong to the thin-film class with respect to their ultrathin active layer thickness. Two representative technologies are the dye-sensitized solar cells (DSSCs) and organic solar cells (OSCs). DSSCs currently seem to be the most efficient third generation cells with a demonstrated efficiency around 13% [10]. OSCs have a slightly lower efficiency, so far the record cell has an efficiency of 10.6% with a tandem structure by Yang Yang Laboratory at the University of California, Los Angeles [11]. Meanwhile some companies like Mitsubishi Chemical and Heliatek also reported cells with efficiency around 10% in 2011 [12, 13]. Compared with conventional cells OSCs are a potentially cheap and simple alternative energy source with good mechanical flexibility, feather-weight, and easy production. However the stability of OSCs remains a problem, and their efficiencies depend on the morphology of the active layer.

1.3 Organic solar cells

A typical OSC usually consists of four layers: an ITO coated substrate (glass or flexible materials), followed by a layer of poly(3,4-ethylenedioxythiophene):poly (styrenesulfonate) (PEDOT:PSS), then the active layer and reflector (usually as anode). The PEDOT:PSS layer serves as a hole transport and exciton blocking layer. Similar to conventional cells the active layer of OSCs is made from two different organic semiconductor materials, one is an electron donor (D) and the other is an electron acceptor (A). The donors can be divided into two different categories, small molecule and polymers. Some commonly used small molecules are Copper phthalocyanine (CuPc), chloro [subphthalocyaninato] boron (SubPc), Zinc phthalocyanine (ZnPc) and so on. While some well developed polymers are poly(3-exylthiophene) (P3HT), poly[(4,40-bis(2-ethylhexyl)dithieno[3,2-b:20,30-d] silole)-2,6-diyl-alt-(2,1,3- benzothiadiazole)-4,7-diyl] (PSBTBT), poly[2,6-(4,4- bis-(2-ethylhexyl)-4H-cyclopenta[2,1-

b;3,4-b'] dithiophene)-alt-4,7-(2,1,3- benzothiadiazole)] (PCPDTBT) and so on [14–16]. Good electron acceptors are buckminster fullerene C_{60} and its derivatives like indene-C_{60} bisadduct (ICBA), [6,6]-phenyl-C71-butyric acid methyl ester ($PC_{70}BM$), [6,6]-phenyl-C_{61} butyric acid methyl ester (PCBM) and so on [14–16]. The small molecule solar cells are usually fabricated with thermal evaporation processes. In contrast polymer solar cells are usually made via solution based technologies, such as spin coating, doctor blading and printing [17].

1.3.1 General working principles

Figure 1.5 shows the operation mechanism of an OSC [18]. There are several steps involved for photocurrent generation [16–18]: 1) Generation of excitons in donor and/or acceptor from light absorption by exciting an electron from the highest occupied molecular orbital (HOMO) to the lowest unoccupied molecular orbital (LUMO). Different from the weakly Coulomb bound electron-hole pairs generated in inorganic solar cells, the exciton is a strongly bound electron-hole pair; 2) Excitons have to diffuse to a D-A interface; 3) Exciton dissociation at the D-A interface, transferring to charge carriers, i.e. free electron and hole; 4) Charge transport to and collection by the electrodes. For each step an efficiency factor can be defined [16–18]:

1. Absorption efficiency η_A, defined as the ratio of the number of photo-generated excitons to that of incident photons.

2. Exciton diffusion efficiency η_{ED}, defined as the ratio of the number of diffusing excitons to a D-A interface to that of photo-generated excitons.

3. Charge transfer efficiency η_{CT}, defined as the ratio of the number of dissociated excitons at a D-A interface to that of diffusing excitons to a D-A interface.

4. Charge collection efficiency η_{CC}, defined as the ratio of the number of free charge carriers collected at electrodes to that of dissociated excitons at a D-A interface.

Then the internal (η_{IQE}) and external (η_{EQE}) quantum efficiencies are given by:

$$\eta_{IQE} = \eta_{ED} \cdot \eta_{CT} \cdot \eta_{CC} \tag{1.6}$$

$$\eta_{EQE} = \eta_A \cdot \eta_{IQE} = \eta_A \cdot \eta_{ED} \cdot \eta_{CT} \cdot \eta_{CC} \tag{1.7}$$

OSCs with η_{IQE} close to 100% have been demonstrated with an active layer (PCPDTBT:$PC_{70}BM$) thickness of 80nm [19]. Therefore the absorption is mainly

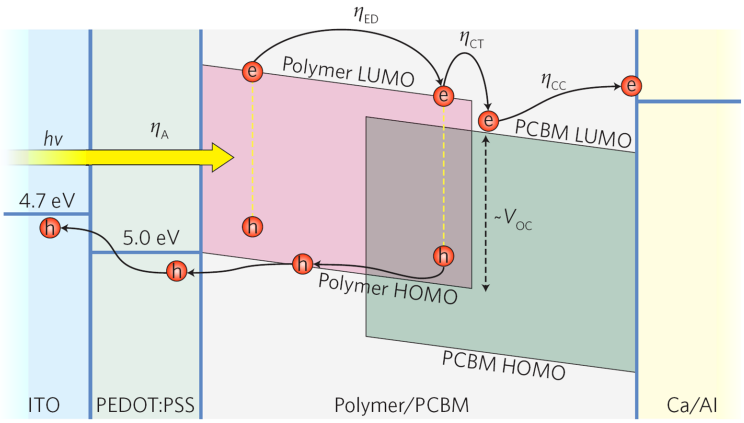

Figure 1.5: Operation mechanism of OSCs [18]. By light absorption an exciton is generated. The exciton diffuses to the polymer/PCBM interface where it dissociates into free charge carriers. Finally, the free charge carriers transport to the electrodes. ©2007 ACS

the constraint for η_{EQE} and the photocurrent I_{SC} (or the current density J_{SC}) in Eq. 1.2. The bandgap of the donor limits the fraction of light that can be absorbed in the active layer. Indeed, the bandgap of polymers is relatively large, e.g. for P3HT around 1.9eV, yielding a limited absorption band. The V_{OC} of OSCs is determined by the energy levels of the LUMO of the acceptor (E^A_{LUMO}) and HOMO of the donor (E^D_{HOMO}). An empirical equation is [20]:

$$V_{OC} = e^{-1} \times \left(|E^D_{HOMO}| - |E^A_{LUMO}| - 0.3eV\right). \tag{1.8}$$

For instance an OSC comprised of P3HT and PCBM has a low V_{OC} around 0.6eV. Thus a donor polymer with low bandgap and deeper HOMO energy level[2] is required to get good J_{SC} and V_{OC}.

1.3.2 History of organic solar cells

Single layer OSCs

A single layer of organic material is sandwiched between two different metallic electrodes, one with high work function and another with low work function. Singlet excitons are created by absorption of light when electrons are excited to the LUMO, leaving holes in the HOMO. To generate photocurrent these have to be dissociated by thermal energy or the built-in potential

[2] More precisely one needs to enlarge the energy level difference between the LUMO of the acceptor and the HOMO of the donor.

overcoming the binding energy. The built-in potential can be either from the difference of work function between the electrodes or from a Schottky contact at the metal/organic contacts [21, 22]. However the built-in potential setup by the difference of work function of electrodes, for instance indium tin oxide, ITO, and Al, is not high enough to obtain efficient dissociation. In most cases it uses the Schottky contact cell structure formed between a p-type organic material and a metal with low work function [14, 23]. The exciton will be dissociated at the depletion region of the Schottky contact.

Upon light absorption excitons are generated in the whole organic material. However dissociation can only happen at the depletion region near the metal contact. Due to the short diffusion length of excitons (typically on the order of 10nm) [24–26], most of them get recombined before their dissociation during diffusion to the depletion region. Meanwhile, after dissociation both electrons and holes have to travel in the same material before reaching the electrodes, leaving a large possibility for bimolecular recombination [17]. Therefore this type of OSCs has limited power conversion efficiencies, much less than 1% [27–29].

Bilayer OSCs

The next breakthrough was achieved by applying donor-accepter (D-A) concepts. In 1984 Tang reported a novel bilayer OSC with about 0.95% power conversion efficiency under simulated AM2 illumination conditions, fabricated from CuPc (donor, as the p-type semiconductor) and a perylene tetracarboxylic derivative (acceptor, as n-type semiconductor) [30]. The improved efficiency compared with single layer structures is mainly due to a more efficient charge dissociation. These two layers of materials have differences in electron affinity and ionization energy. The energy level offset at the interface between the two layers can be very large (by choosing proper materials) and yield strong local electric fields. Excitons generated by light absorption dissociate more efficiently at the interface, compared with dissociation by the built-in potential in a single layer structure. After dissociation charge carriers are transported in different organic materials, holes in the donor and electrons in the acceptor. This can reduce bimolecular recombination to a great extent.

Later on by using new materials like buckminster fullerene, C_{60} conjugated polymer poly(phenylene vinylene) (PPV) and their derivatives, the conversion efficiencies of bilayer structure solar cells have improved up to 1–4%. However the bilayer structure still suffers from the limited exciton diffusion range in organic materials.

Bulk heterojunction OSCs

Although the bilayer structure is a big improvement, still a considerable

amount of excitons recombine during diffusion to the D-A interface. Usually thicknesses of OSCs are on the order of 100nm, whereas the diffusion length is typically on the order of 10nm. Therefore, an advanced OSC structure called bulk heterojunction (BHJ) was invented. The BHJ is formed by intimately mixing the donor and the accepter. This concept was first developed for the small molecule solar cells in 1992 by Hiramoto *et al.* by co-evaporating donor and acceptor molecules under high-vacuum conditions [31]. Later this concept was extended to polymer solar cells in 1995 by Heeger's group [32]. Relatively high efficiencies around 4–5% have been demonstrated using a polymer mixture of P3HT and PCBM [33–35]. For polymer solar cells several solution processing techniques can be used to fabricate BHJ OSCs, such as spin coating, screen printing, spray coating and so on. As shown in Fig. 1.6 the D-A interface in a BHJ is spatially distributed throughout the whole active layer, instead of a planar D-A heterojunction in the bilayer structure. The benefit is that excitons can be efficiently and ideally dissociated within their lifetime. Similar with bilayer structures the charge carriers are separated and transported within organic materials, which results in a good conversion efficiency. The morphology of the active layer is critical for the performance of BHJ OSCs, since only excitons created within the diffusion length contribute. Therefore several morphology control methods have been developed, such as thermal annealing [34, 36, 37] and the addition of processing additives [38, 39].

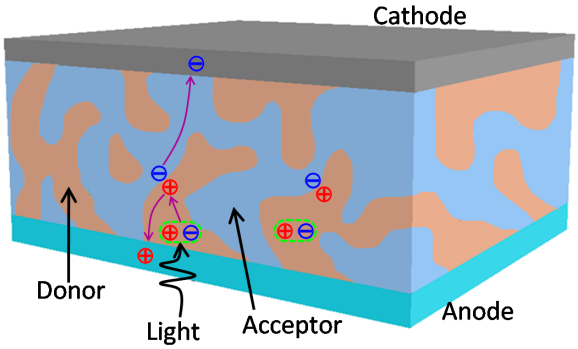

Figure 1.6: Schematic diagram of bulk heterojunction structure of OSCs together with the processes involved. Signs '⊕' and '⊖' denote hole and electron.

1.4 Light trapping

A key challenge for crystalline silicon cells remains that the absorption is always relatively weak in the near infrared, due to the indirect band gap. In order to get considerable efficiency solar cells have to absorb sunlight as much as possible. This consequently requires a thick active layer, a few hundred microns, before light gets absorbed. Together with the concomitant increasing carrier diffusion length requirement, material cost is driven higher. Therefore it is always a trade-off between efficiency and material cost for traditional solar cells. On the other hand, organic materials have a lower carrier mobility and require exciton dissociation, which limits the active layer thickness. However thin active layers have poor light absorption. Therefore light trapping is needed in order to bring down the thickness, yet to still provide a quite efficient absorption.

For traditional solar cells, light trapping is usually achieved by introducing micrometer scale pyramid-like surface textures to increase surface roughness. From ray optics theory, the light path compared to a single pass can be enhanced up to a limiting factor of $4n^2$ [40], where n is the refractive index of the active material. This limit is applicable in the framework of ray optics, where wave effects like diffraction and interference are negligible. To achieve this limit a Lambertian roughness has to be introduced which has an isotropic response. Meanwhile it is mainly valid for an active layer of about a few hundred microns, and for wavelengths near the band edge where the intrinsic absorption coefficient is low. The enhancement factor drops tremendously at wavelengths where a large absorption coefficient is present.

This $4n^2$ limit becomes invalid for thin-film solar cells such as OSCs which have thin active layers comparable with the wavelength, usually only 100–200nm thick, and have a high absorption coefficient. Since for thin-film solar cells the wave character of light becomes significant, trapping approaches have to be considered in the framework of wave optics. Recently, theoretical studies based on statistical coupled mode theory have shown the possibility to surpass the $4n^2$ limit in a thin-film Si solar cell (with a few micron thickness) by a grating structure in the wave optics regime [41]. In [41] they have derived that a maximum absorption enhancement limit of $4\pi n^2$ can be achieved by 2D gratings with a square lattice, for $0 < s < 1$, where s is the ratio of grating period to the wavelength. For a triangular lattice this enhancement limit can be as high as $8\pi n^2/\sqrt{3}$ for $0 < s < 2/\sqrt{3}$. The maximum enhancement converges to the limit of $4n^2$ for large values of s (corresponding to the Lambertian limit).

In general any photonic structure or phenomenon that exhibits energy confinement is potentially useful for light trapping. Many trapping schemes are proposed and investigated theoretically and experimentally for thin-film solar cells (both inorganic and organic), such as 2D or 3D photonic crystals [42–45],

dielectric gratings [46–52], folded structures [53, 54], metallic nanoparticles [55–68], metallic gratings [69–85] and so on. All of these schemes try to increase the photon density in solar cells, specifically in the active layer, by exploiting some photonic phenomena like diffraction, interference, cavity resonances, guided modes, surface plasmons and so on.

Recently, metallic nanostructures, such as metallic nanoparticles and gratings, have received considerable attention for their ability to concentrate and manipulate light at the nanoscale, and thus for light trapping. Plasmonic modes can, in general, be classified into two categories: localized surface plasmons (LSPs) and propagating surface plasmon polaritons (SPPs). The former are associated with very local excitations, such as around nanoparticles. The latter are associated with surfaces, along which a mode can propagate. Both LSPs and SPPs create mainly two effects: enhanced near-field intensities and enhanced scattering of light. A recent review by Atwater *et al.* [86] concerning the intersection of plasmonics and photovoltaics has summarized the commonly used plasmonic light trapping schemes (see Fig. 1.7). In general there are three different schemes, one with metallic nanostructures on top of the cells as scattering elements (Fig. 1.7(a)), one with structures inside as antennas (Fig. 1.7(b)), and the last one with structures integrated with the metallic back contact where light can be coupled into SPP modes and other guided modes in the layered device (Fig. 1.7(c)). More details about plasmonic phenomena are provided in chapter 2.

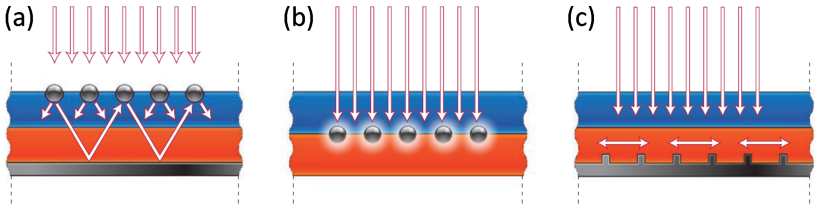

Figure 1.7: Plasmonic light trapping schemes for thin-film solar cells [86]. (a) Light trapping by scattering from metal nanostructures at the surface of the solar cell. (b) Light trapping by excitation of localized surface plasmons in particles embedded in the active layer. (c) Light trapping by the excitation of surface plasmon polaritons at the metal/active layer interface. ©2010 Macmillan Publishers Limited.

1.5 Objectives and thesis outline

Organic solar cells enjoy a strong potential compared to inorganic solar cells, for example because of the possibility of low-cost fabrication of lightweight, large-

area devices. However, important issues such as low efficiencies and stability need to be addressed. So far the efficiency of OSCs is still around the 10% efficiency barrier. In early 2012 Yang's group set a new world record with an efficiency of 10.6% with a tandem device [11].

The low efficiency limitation is mainly imposed by the short exciton diffusion length in organic materials, which is typically around 10nm, and also other aspects such as the relative bandgap and low energy level of the donor HOMO. This diffusion length is much smaller than the light absorption length in organic materials, usually 100–200nm. Therefore there is an important tradeoff between optical and electronic properties, leading to the challenge to absorb as much light as possible in an active layer as thin as possible. To achieve this, nanophotonic light trapping schemes offer help.

The work presented in this thesis is part of the IWT-SBO Polyspec project, which aimed at increasing the energy conversion efficiency of organic bulk heterojunction photovoltaic devices, as well as improving the stability of their nanomorphology, involving material development, morphological analysis and modeling, optical modeling and so on. Our work focused on optical modeling of the use of metallic nanostructures for light harvesting, as these elements tend to be very compact, and seem at first sight compatible with OSCs.

At the onset of this work, only preliminary results on plasmonic enhancement of organic devices, such as solar cells and organic LEDs, were available. Therefore the potential of metallic nanostructures in OSCs remained an open question. Here we summarize our findings using theoretical and numerical approaches, on the use of various metallic nanostructures, such as particles and gratings, to enhance the light absorption in OSCs.

The text is organized as follows. In chapter 2 various basic concepts are explained. There we introduce the surface plasmon mode at interfaces, the analytical Mie theory for plasmonic modes in spheroid metallic nanoparticles, and the numerical modeling tools we use throughout this work. In chapter 3 we focus on utilizing metallic nanoparticles for light absorption enhancement. We start with a simplified 2D model to analyze the absorption enhancement mechanism. Then we extend to a more concrete 3D model. In chapter 4 we examine metallic gratings by exploiting both SPPs and LSPs for an efficiency boost. We combine front and back gratings together, to have an additive enhancement from each grating. In chapter 5 gratings with tapered slits are examined. By tapering we see an enhanced and broadened transmission, which may be useful for light harvesting in solar cells. Finally chapter 6 provides conclusions and perspectives for the future work.

1.6 Publications

Publications in international journals

1. B. Niesen, B.P. Rand, P. Van Dorpe, D. Cheyns, H. Shen, B. Maes, and P. Heremans. *Near-field interactions between metal nanoparticle surface plasmons and molecular excitons in thin-films. Part I: absorption.* 2012. (Submitted)

2. H. Shen, and B. Maes. *Enhanced optical transmission through tapered metallic gratings.* Applied Physics Letters, 100(24):241104, June 2012.

3. R. Morarescu, H. Shen, R. A. L. Vallée, B. Maes, B. Kolaric, and P. Damman. *Exploiting the Localized Surface Plasmon Modes in Gold Triangular Nanoparticles for Sensing Applications.* Journal of Materials Chemistry, 22(23):11537-11542, May 2012

4. H. Shen, and B. Maes. *Combined plasmonic gratings in organic solar cells.* Optics Express, 19(S6):A1202-A1210, November 2011.

5. A. Abass, H. Shen, P. Bienstman, and B. Maes. *Angle insensitive enhancement of organic solar cells using metallic gratings.* Journal of Applied Physics, 109(2):023111, January 2011.

6. B. Niesen, B. P. Rand, P. Van Dorpe, H. Shen, B. Maes, J. Genoe, and P. Heremans. *Excitation of multiple dipole surface plasmon resonances in spherical silver nanoparticles.* Optics Express, 18(18):19032-19038, August 2010.

7. H. Shen, P. Bienstman, and B. Maes. *Plasmonic absorption enhancement in organic solar cells with thin active layers.* Journal of Applied Physics, 106(7):073109, October 2009.

Publications in international conferences

8. H. Shen, A. Abass, M. Burgelman, B. Maes, *Tailored and tapered metallic gratings for enhanced absorption or transmission.* In ICTON (International Conference on Transparent Optical Networks) (invited), United Kingdom, 2012. (to be published)

9. H. Shen, A. Abass, M. Burgelman, B. Maes, *Thin-film solar cells with combined metallic enhancements.* MINAP (Micro- and nano-photonic materials and devices), page 103-104, Italy, 2012.

10. H. Shen, and B. Maes. *Plasmonic enhancement in organic solar cells with metallic gratings.* In 16th Annual Symposium of the IEEE Photonics Benelux Chapter, page 21–24, Ghent, Belgium, December 2011.

11. H. Shen, and B. Maes. *Combined Plasmonic Gratings in Thin Organic Solar Cells*. In Photonics Prague 2011, page 73, Czech Republic, 2011.

12. A. Abass, H. Shen, K. Quang Le, P. Bienstman, and B. Maes. *On the angular dependent nature of absorption enhancement in organic solar cells by metallic nanostructures*. In 8th International Symposium on Modern Optics and Its Applications, page PP-07, Indonesia, 2011.

13. B. Maes, A. Abass, H. Shen, and P. Bienstman. *Plasmonic absorption enhancement in organic photovoltaics*. In ICTON (International Conference on Transparent Optical Networks) (invited), page We.A2.5, Germany, 2010.

14. A. Abass, H. Shen, P. Bienstman, and B. Maes. *Increasing Polymer Solar Cell Efficiency with Triangular Silver Gratings*. In Optical Nanostructures for Photovoltaics (PV) (invited), page PWA5, Germany, 2010.

15. B. Maes, H. Shen, and P. Bienstman. *Plasmonic nanoparticle enhancement in thin organic solar cells*. In ICTON (International Conference on Transparent Optical Networks) Mediterranean Winter - COST MP0702 workshop, page Fr3B.5 ,France, 2009.

16. H. Shen, P. Bienstman, and B. Maes. *Absorption enhancement in organic solar cells by metallic nanoparticles*. In 14th Annual Symposium of the IEEE Photonics Benelux Chapter, page 85–88, Brussels, Belgium, November 2009.

Publications in national conferences

17. H. Shen, and B. Maes. *Metallic grating enhanced absorption in organic solar cells*. In 12th FEA PhD Symposium, page 98, Ghent, Belgium, December 2011.

18. H. Shen, P. Bienstman, and B. Maes. *Absorption enhancement in organic solar cells by metallic nanoparticles*. In 10th UGent-FirW PhD Symposium, pages 290-291, Ghent, Belgium, December 2009.

References

[1] U.S. Energy Information Administration. *International Energy Outlook 2011*, September 2011.

[2] A. Goetzberger and V. U. Hoffmann. *Photovoltaic Solar Energy Generation*, volume 112. Springer Verlag, 2005.

[3] S. M. Sze and K. K. Ng. *Semiconductor Devices: Physics and Technology*. John Wiley & Sons, third edition edition, 2007.

[4] A. E. Becquerel. *On electric effects under the influence of solar radiation.* Compt. Rend. Acad. Sci., 9:561, 1839.

[5] D. M. Chapin, C. S. Fuller, and G. L. Pearson. *A New Siliconp-n Junction Photocell for Converting Solar Radiation into Electrical Power*. Journal of Applied Physics, 25:676, 1954.

[6] D. C. Reynolds, G. Leies, and R. E. Antes, L. L. and. Marburger. *Photovoltaic Effect in Cadmium Sulfide*. Physical Review, 96(2):533–534, 1954.

[7] M. A. Green, K. Emery, Y. Hishikawa, W. Warta, and E. D. Dunlop. *Solar cell efficiency tables (version 39)*. Progress in Photovoltaics: Research and Applications, 20(1):12–20, 2012.

[8] H. Yuen. *High Efficiency Solar Cells at Solar Junction.* In Optics for Solar Energy. Optical Society of America, 2011.

[9] A. Goetzberger, J. Luther, and G. Willeke. *Solar cells : past , present , future.* Solar Energy, 74:1–11, 2002.

[10] A. Yella, H. W. Lee, H. N. Tsao, C. Yi, A. K. Chandiran, M. K. Nazeeruddin, E. W. G. Diau, C. Y. Yeh, S. M. Zakeeruddin, and M. Grätzel. *Porphyrin-Sensitized Solar Cells with Cobalt (II/III)–Based Redox Electrolyte Exceed 12 Percent Efficiency.* Science, 334(6056):629–634, 2011.

[11] W. W. Kromhout. *UCLA engineers create tandem polymer solar cells that set record for energy-conversion.* Technical report, University of California, Los Angeles, February 2012.

[12] http://www.independent.co.uk/environment/sprayon-solar-may-be-future-for-green-energy 2343590.html.

[13] http://www.heliatek.com/.

[14] H. Hoppe and N. S. Sariciftci. *Organic solar cells: An overview.* Journal of Materials Research, 19(7):1924–1945, 2004.

[15] J. Y. Kim, K. Lee, N. E. Coates, D. Moses, T. Q. Nguyen, M. Dante, and A. J. Heeger. *Efficient tandem polymer solar cells fabricated by all-solution processing.* Science, 317(5835):222–225, 2007.

[16] G. Li, R. Zhu, and Y. Yang. *Polymer solar cells.* Nature Photonics, 6(3):153–161, 2012.

[17] T. Soga, editor. *Nanostructured Materials for Solar Energy Conversion.* Elsevier, Amsterdam, The Netherlands, first edition edition, 2006.

[18] X. Yang and J. Loos. *Toward high-performance polymer solar cells: The importance of morphology control.* Macromolecules, 40(5):1353–1362, 2007.

[19] S. H. Park, A. Roy, S. Beaupré, S. Cho, N. Coates, J. S. Moon, D. Moses, M. Leclerc, K. Lee, and A. J. Heeger. *Bulk heterojunction solar cells with internal quantum efficiency approaching 100%.* Nature Photonics, 3(5):297–302, 2009.

[20] M. C. Scharber, D. Mühlbacher, M. Koppe, P. Denk, C. Waldauf, A. J. Heeger, and C. J. Brabec. *Design rules for donors in bulk-heterojunction solar cellsąłTowards 10% energy-conversion efficiency.* Advanced Materials, 18(6):789–794, 2006.

[21] D. Wohrle and D. Meissner. *Organic Solar Cells.* Advanced Materials, 3:129–138, 1991.

[22] C. J. Brabec and N. S. Sariciftci. *Plastic solar cells.* Advanced Functional Materials, (1):15–26, 2001.

[23] G. Chamberlain. *Organic solar cells: A review.* Solar Cells, 8(1):47–83, 1983.

[24] J. J. M. Halls, K. Pichler, R. H. Friend, S. C. Moratti, and A. B. Holmes. *Exciton diffusion and dissociation in a poly (p-phenylenevinylene)/C60 heterojunction photovoltaic cell.* Applied physics letters, 68:3120, 1996.

[25] L. A. A. Pettersson, L.S. Roman, and O. Inganäs. *Modeling photocurrent action spectra of photovoltaic devices based on organic thin films.* Journal of Applied Physics, 86:487, 1999.

[26] P. E. Shaw, A. Ruseckas, and I. D. W. Samuel. *Exciton diffusion measurements in poly (3-hexylthiophene).* Advanced Materials, 20(18):3516–3520, 2008.

[27] A. K. Ghosh and T. Feng. *Merocynanine organic solar cells.* Journal of Applied Physics, 49(12):5982–5989, 1978.

[28] D. L. Morel, A. K. Ghosh, T. Feng, E. L. Stogryn, P. E. Purwin, R. F. Shaw, and C. Fishman. *High-efficiency organic solar cells.* Applied Physics Letters, 32(8):495–497, 1978.

[29] C Brabec. *Organic photovoltaics: technology and market.* Solar Energy Materials and Solar Cells, 83(2-3):273–292, 2004.

[30] C. W. Tang. *Two-layer organic photovoltaic cell.* Applied Physics Letters, 48(2):183, 1986.

[31] M. Hiramoto, H. Fujiwara, and M. Yokoyama. *p-i-n like behavior in three-layered organic solar cells having a co-deposited interlayer of pigments.* Journal of Applied Physics, 72(8):3781–3787, 1992.

[32] G. Yu, J. Gao, J. C. Hummelen, F. Wudl, and A. J. Heeger. *Polymer photovoltaic cells: enhanced efficiencies via a network of internal donor-acceptor heterojunctions.* Science, 270(5243):1789–1791, 1995.

[33] G. Li, V. Shrotriya, J. Huang, Y. Yao, T. Moriarty, K. Emery, and Y. Yang. *High-efficiency solution processable polymer photovoltaic cells by self-organization of polymer blends.* Nature Materials, 4(11):864–868, 2005.

[34] W. Ma, C. Yang, X. Gong, K. Lee, and A. J. Heeger. *Thermally stable, efficient polymer solar cells with nanoscale control of the interpenetrating network morphology.* Advanced Functional Materials, 15(10):1617–1622, 2005.

[35] Y. Kim, S. Cook, S. M. Tuladhar, S. A. Choulis, J. Nelson, J. R. Durrant, D. D. C. Bradley, M. Giles, I. McCulloch, C.-S. Ha, and M. Ree. *A strong regioregularity effect in self-organizing conjugated polymer films and high-efficiency polythiophene:fullerene solar cells.* Nature Materials, 5(3):197–203, 2006.

[36] F. Padinger, R. S. Rittberger, and N. S. Sariciftci. *Effects of postproduction treatment on plastic solar cells.* Advanced Functional Materials, 13(1):85–88, 2003.

[37] H. Hoppe and N. S. Sariciftci. *Morphology of polymer/fullerene bulk heterojunction solar cells.* Journal of Materials Chemistry, 16(1):45–61, 2006.

[38] J. Peet, J. Y. Kim, N. E. Coates, W. L. Ma, D. Moses, A. J. Heeger, and G. C. Bazan. *Efficiency enhancement in low-bandgap polymer solar cells by processing with alkane dithiols.* Nature Materials, 6(7):497–500, 2007.

[39] J. K. Lee, W. L. Ma, C. J. Brabec, J. Yuen, J. S. Moon, J. Y. Kim, K. Lee, G. C. Bazan, and A. J. Heeger. *Processing additives for improved efficiency from bulk heterojunction solar cells.* Journal of the American Chemical Society, 130(11):3619–3623, 2008.

[40] E. Yablonovitch. *Statistical ray optics.* Journal of Optical Society of America, 72(7):899–907, 1982.

[41] Z. Yu, A. Raman, and S. Fan. *Fundamental limit of light trapping in grating structures.* Optics Express, 18(103):A366–A380, 2010.

[42] L. Zeng, Y. Yi, C. Hong, J. Liu, N. Feng, X. Duan, L. C. Kimerling, and B. A. Alamariu. *Efficiency enhancement in Si solar cells by textured photonic crystal back reflector.* Applied Physics Letters, 89(11):111111, 2006.

[43] P. Bermel, C. Luo, L. Zeng, L. C. Kimerling, and J. D. Joannopoulos. *Improving thin-film crystalline silicon solar cell efficiencies with photonic crystals.* Optics Express, 15(25):16986–17000, 2007.

[44] Y. Park, E. Drouard, O. E. Daif, X. Letartre, A. Fave, A. Kaminski, M. Lemiti, and C. Seassal. *Absorption enhancement using photonic crystals for silicon thin film solar cells.* Optics Express, 17(16):14312–14321, 2009.

[45] J. R. Tumbleston, D.-H. Ko, E. T. Samulski, and R. Lopez. *Absorption and quasiguided mode analysis of organic solar cells with photonic crystal photoactive layers.* Optics Express, 17(9):7670–81, 2009.

[46] S. H. Zaidi, J. M. Gee, and D. S. Ruby. *Diffraction grating structures in solar cells.* In Photovoltaic Specialists Conference. Conference Record of the Twenty-Eighth IEEE, pages 395–398. IEEE, 2000.

[47] C. Eisele, C. E. Nebel, and M. Stutzmann. *Periodic light coupler gratings in amorphous thin film solar cells.* Journal of Applied Physics, 89:7722, 2001.

[48] S. H. Zaidi, R. Marquadt, B. Minhas, and J. W. Tringe. *Deeply etched grating structures for enhanced absorption in thin c-Si solar cells.* In Photovoltaic Specialists Conference. Conference Record of the Twenty-Ninth IEEE, pages 1290–1293. IEEE, 2002.

[49] M. Niggemann, M. Glatthaar, A. Gombert, A. Hinsch, and V. Wittwer. *Diffraction gratings and buried nano-electrodesąłarchitectures for organic solar cells.* Thin Solid Films, 451:619–623, 2004.

[50] F. Llopis and I. Tobias. *The role of rear surface in thin silicon solar cells.* Solar Energy Materials and Solar Cells, 87(1):481–492, 2005.

[51] S. I. Na, S. S. Kim, J. Jo, S. H. Oh, J. Kim, and D. Y. Kim. *Efficient polymer solar cells with surface relief gratings fabricated by simple soft lithography.* Advanced Functional Materials, 18(24):3956–3963, 2008.

[52] A. Raman, Z. Yu, and S. Fan. *Dielectric nanostructures for broadband light trapping in organic solar cells.* Optics Express, 19(20):7670–7681, 2011.

[53] S.-B. Rim, S. Zhao, S. R. Scully, M. D. McGehee, and P. Peumans. *An effective light trapping configuration for thin-film solar cells.* Applied Physics Letters, 91(24):243501, 2007.

[54] V. Andersson, K. Tvingstedt, and O. Inganäs. *Optical modeling of a folded organic solar cell.* Journal of Applied Physics, 103(9):094520, 2008.

[55] K. Kim and D. L. Carroll. *Roles of Au and Ag nanoparticles in efficiency enhancement of poly(3-octylthiophene)/C[sub 60] bulk heterojunction photovoltaic devices.* Applied Physics Letters, 87(20):203113, 2005.

[56] A. J. Morfa, K. L. Rowlen, T. H. Reilly, M. J. Romero, and J. van de Lagemaat. *Plasmon-enhanced solar energy conversion in organic bulk heterojunction photovoltaics.* Applied Physics Letters, 92(1):013504, 2008.

[57] H. Shen, P. Bienstman, and B. Maes. *Plasmonic absorption enhancement in organic solar cells with thin active layers.* Journal of Applied Physics, 106(7):073109–073109, 2009.

[58] J. H. Lee, J. H.and Park, J. S. Kim, D. Y. Lee, and K. Cho. *High efficiency polymer solar cells with wet deposited plasmonic gold nanodots.* Organic Electronics, 10(3):416–420, 2009.

[59] K. Topp, H. Borchert, F. Johnen, A. V. Tunc, M. Knipper, E. von Hauff, J. Parisi, and K. Al-Shamery. *Impact of the incorporation of Au nanoparticles into polymer/fullerene solar cells.* The Journal of Physical Chemistry. A, 114(11):3981–9, 2010.

[60] J.-L. Wu, F.-C. Chen, Y.-S. Hsiao, F.-C. Chien, P. Chen, C.-H. Kuo, M. H. Huang, and C.-S. Hsu. *Surface plasmonic effects of metallic nanoparticles on the performance of polymer bulk heterojunction solar cells.* ACS Nano, 5(2):959–67, 2011.

[61] I. Diukman, L. Tzabari, N. Berkovitch, N. Tessler, and M. Orenstein. *Controlling absorption enhancement in organic photovoltaic cells by patterning Au nano disks within the active layer.* Optics Express, 19(S1):A64–71, 2011.

[62] Y. A. Akimov and W. S. Koh. *Design of Plasmonic Nanoparticles for Efficient Subwavelength Light Trapping in Thin-Film Solar Cells.* Plasmonics, 6(1):155–161, 2010.

[63] D. H. Wang, D. Y. Kim, K. W. Choi, J. H. Seo, S. H. Im, J. H. Park, O. O. Park, and A. J. Heeger. *Enhancement of Donor-Acceptor Polymer Bulk Heterojunction Solar Cell Power Conversion Efficiencies by Addition of Au Nanoparticles.* Angewandte Chemie International Edition, 50(24):5519–523, 2011.

[64] D. H. Wang, K. H. Park, J. H. Seo, J. Seifter, J. H. Jeon, J. K. Kim, J. H. Park, O. O. Park, and A. J. Heeger. *Enhanced Power Conversion Efficiency in PCDTBT/PC70BM Bulk Heterojunction Photovoltaic Devices with Embedded Silver Nanoparticle Clusters.* Advanced Energy Materials, 1(5):766–70, 2011.

[65] X. Wang, J. W. Ho, Q. Yang, H. L. Tam, G. X. Li, K. W. Cheah, and F. Zhu. *Performance enhancement in organic photovoltaic devices using plasma-polymerized fluorocarbon-modified Ag nanoparticles.* Organic Electronics, 12(11):1943–1947, 2011.

[66] J. Zhu, M. Xue, H. Shen, Z. Wu, S. Kim, J.-J. Ho, A. Hassani-Afshar, B. Zeng, and K. L. Wang. *Plasmonic effects for light concentration in organic photovoltaic thin films induced by hexagonal periodic metallic nanospheres.* Applied Physics Letters, 98(15):151110, 2011.

[67] S.-J. Tsai, M. Ballarotto, D. B. Romero, W. N. Herman, H.-C. Kan, and R. J. Phaneuf. *Effect of gold nanopillar arrays on the absorption spectrum of a bulk heterojunction organic solar cell.* Optics Express, 18(S4):A528–35, 2010.

[68] D. Qu, F. Liu, Y. Huang, W. Xie, and Q. Xu. *Mechanism of optical absorption enhancement in thin film organic solar cells with plasmonic metal nanoparticles.* Optics Express, 19(24):24795–803, 2011.

[69] V. E. Ferry, L. A. Sweatlock, D. Pacifici, and H. A. Atwater. *Plasmonic nanostructure design for efficient light coupling into solar cells.* Nano Letters, 8(12):4391–7, 2008.

[70] V. E. Ferry, M. A. Verschuuren, H. B. T. Li, E. Verhagen, R. J. Walters, R. E. I. Schropp, H. A. Atwater, and A. Polman. *Light trapping in ultrathin plasmonic solar cells.* Optics Express, 18(S2):A237–45, 2010.

[71] A. Abass, K. Le, A. Alù, M. Burgelman, and B. Maes. *Dual-interface gratings for broadband absorption enhancement in thin-film solar cells.* Physical Review B, 85(11):1–8, 2012.

[72] R. A. Pala, J. White, E. Barnard, J. Liu, and M. L. Brongersma. *Design of Plasmonic Thin-Film Solar Cells with Broadband Absorption Enhancements.* Advanced Materials, 21(34):3504–3509, 2009.

[73] W. Wang, S. Wu, K. Reinhardt, Y. Lu, and S. Chen. *Broadband light absorption enhancement in thin-film silicon solar cells.* Nano Letters, 10(6):2012–8, 2010.

[74] C. C. Chao, C. M. Wang, and J. Y. Chang. *Spatial distribution of absorption in plasmonic thin film solar cells.* Optics Express, 18(11):11763–71, 2010.

[75] W. Bai, Q. Gan, F. Bartoli, J. Zhang, L. Cai, Y. Huang, and G. Song. *Design of plasmonic back structures for efficiency enhancement of thin-film amorphous Si solar cells.* Optics Letters, 34(23):3725–7, 2009.

[76] J. N. Munday and H. A. Atwater. *Large integrated absorption enhancement in plasmonic solar cells by combining metallic gratings and antireflection coatings.* Nano Letters, 11(6):2195–201, 2011.

[77] A. Abass, H. Shen, P. Bienstman, and B. Maes. *Angle insensitive enhancement of organic solar cells using metallic gratings.* Journal of Applied Physics, 109(2):023111–023111, 2011.

[78] M. G. Kang, T. Xu, H. J. Park, X. Luo, and L. J. Guo. *Efficiency enhancement of organic solar cells using transparent plasmonic Ag nanowire electrodes.* Advanced Materials, 22(39):4378–83, 2010.

[79] C. Min, J. Li, G. Veronis, J. Y. Lee, S. Fan, and P. Peumans. *Enhancement of optical absorption in thin-film organic solar cells through the excitation of plasmonic modes in metallic gratings.* Applied Physics Letters, 96(13):133302, 2010.

[80] M. A. Sefunc, A. K. Okyay, and H. V. Demir. *Plasmonic backcontact grating for P3HT:PCBM organic solar cells enabling strong optical absorption increased in all polarizations.* Optics Express, 19(15):14200–9, 2011.

[81] M. A. Sefunc, A. K. Okyay, and H. V. Demir. *Volumetric plasmonic resonator architecture for thin-film solar cells.* Applied Physics Letters, 98(9):093117, 2011.

[82] K. Tvingstedt, N. K. Persson, O. Inganäs, A. Rahachou, and I. V. Zozoulenko. *Surface plasmon increase absorption in polymer photovoltaic cells.* Applied Physics Letters, 91(11):113514, 2007.

[83] W. Bai, Q. Gan, G. Song, L. Chen, Z. Kafafi, and F. Bartoli. *Broadband short-range surface plasmon structures for absorption enhancement in organic photovoltaics.* Optics Express, 18(S4):A620–30, 2010.

[84] H. Shen and B. Maes. *Combined plasmonic gratings in organic solar cells.* Optics Express, 19(106):A1202–A1210, 2011.

[85] Y. Liu and J. Kim. *Polarization-diverse broadband absorption enhancement in thin-film photovoltaic devices using long-pitch metallic gratings.* Journal of Optical Society America B, 28(8):1934–1939, 2011.

[86] H. A. Atwater and A. Polman. *Plasmonics for improved photovoltaic devices.* Nature Materials, 9:205–214, 2010.

2 Background

2.1 Introduction

In this chapter some fundamental concepts are introduced concerning plasmonics and optical modeling techniques involved in this work.

Plasmonics is based on the interaction of light and conduction electrons at metallic interfaces or in nanoparticles [1]. Therefore in the field of plasmonics there are mainly two excitations: the propagating surface plasmon polaritons (SPPs) at interfaces and the non-propagating localized surface plasmons (LSPs) around nanoparticles. In this chapter starting from Maxwell's equations (section 2.2) the fundamentals of SPPs and LSPs are described. In section 2.3 we review the properties of SPPs, with discussion of the methods for optical excitation. In section 2.4 we outline the Mie theory for spherical metallic nanoparticles (MNPs) in non-absorbing media. Using the Mie theory we show basic properties, such as enhanced near-fields and scattering, associated with the excitation of LSPs. Furthermore we outline the extended Mie theory for MNPs in absorbing media, which is useful in studying the absorption in solar cells. In section 2.5 we describe shortly the LSP in nanowires.

Subsequently, in section 2.6 we introduce the optical modeling methods used in our investigations. First for a single spherical MNP we introduce the MATLAB implementation of (extended) Mie theory. For simulations of more complicated arrays and structures in OSCs we introduce the basic ideas behind

the finite element method (FEM), a numerical method used in the commercial COMSOL software.

2.2 Light in homogeneous media

In macroscopic electromagnetism all phenomena are governed by the Maxwell equations in matter. These equations are:

$$\nabla \times \mathbf{E} = -\frac{\partial \mathbf{B}}{\partial t} \tag{2.1}$$

$$\nabla \times \mathbf{H} = \mathbf{J} + \frac{\partial \mathbf{D}}{\partial t} \tag{2.2}$$

$$\nabla \cdot \mathbf{D} = \rho \tag{2.3}$$

$$\nabla \cdot \mathbf{B} = 0 \tag{2.4}$$

where **E** and **H** are the electric and magnetic fields, respectively, **D** and **B** are the displacement and magnetic induction fields, ρ and J are the free charge and current densities. Here, homogeneous and linear materials with no charges ($\rho = 0$) and no currents ($J = 0$) will be considered. The following constitutive relations hold:

$$\mathbf{D} = \epsilon \mathbf{E} \tag{2.5}$$

$$\mathbf{B} = \mu \mathbf{H} \tag{2.6}$$

where ϵ and μ are the permittivity and permeability of the material, determined by $\epsilon = \epsilon_0 \epsilon_r$ and $\mu = \mu_0 \mu_r$, respectively. Magnetic materials are not investigated here, so $\mu_r = 1$ and $\epsilon_r = n^2$ (ϵ_r and n are the relative permittivity and refractive index).

Assuming a harmonic time dependence $e^{-i\omega t}$, the curls of Eqs. 2.1 and 2.2, simplified by the vector identity $\nabla \times (\nabla \times \mathbf{A}) = \nabla (\nabla \cdot \mathbf{A}) - (\nabla \cdot \nabla) \mathbf{A}$, are

$$\nabla^2 \mathbf{E} + k^2 \mathbf{E} = 0 \tag{2.7}$$

$$\nabla^2 \mathbf{H} + k^2 \mathbf{H} = 0 \tag{2.8}$$

where $k = \omega \sqrt{\epsilon \mu} = n\omega / c$. Thus **E** and **H** satisfy the vector wave equation. For a given system the solution to the wave equation without external excitation is an eigenfunction solution of the system, sometimes called homogeneous solution.

Any electromagnetic field is required to satisfy the Maxwell equations in a homogenous dielectric material. However when there is a system composed

of several macroscopic domains of homogeneous dielectric materials, there is a discontinuity at the boundary between these different materials. At such boundaries the boundary conditions have to be imposed:

$$(\mathbf{E_1} - \mathbf{E_2}) \times \hat{\mathbf{n}} = 0 \tag{2.9}$$

$$(\mathbf{H_1} - \mathbf{H_2}) \times \hat{\mathbf{n}} = 0 \tag{2.10}$$

where $\hat{n}$ is the outward directed unit vector normal to the boundary, ($\mathbf{E_1}$, $\mathbf{H_1}$) and ($\mathbf{E_2}$, $\mathbf{H_2}$) are the fields at two sides of the same boundary. The boundary conditions require that the tangential components of $\mathbf{E}$ and $\mathbf{H}$ are continuous across the interface. Theoretically most of electromagnetism can be generalized as solving Maxwell's equations or the vector wave equation combined with the boundary conditions.

2.3 Surface plasmon polaritons at metal surfaces

2.3.1 Physics of surface plasmon polaritons

SPPs are trapped surface modes of electromagnetic waves that propagate along the interface between a metal and a dielectric. It is a result of collective oscillation of electrons at the metal-dielectric interface. Typical metals that support surface plasmons are silver and gold.

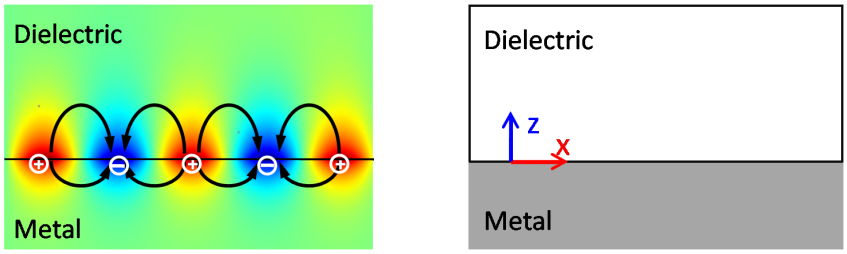

(a) (b)

Figure 2.1: (a) Surface plasmon polaritons at a metal surface. Signs '⊕' and '⊖' denote the positive and negative surface charges, respectively. (b) Schematic diagram of an interface between metal and dielectric.

Fig. 2.1(a) shows the field profile connected to an SPP, the surface wave propagates along the interface between the two media. The field of the wave exponentially decays along the transverse z-axis.

Now let us consider two semi-infinite spaces representing two different media as the schematic shown in Fig. 2.1(b). Since it is known that only TM-light

can excite surface plasmons, we assume a TM-polarized wave at these two domains given by [2]:

$$\text{for} \quad z>0, \quad \mathbf{H_d} = \left(0,\ H_{yd},\ 0\right)\exp\left(i\left(k_{xd}x + k_{zd}z - \omega t\right)\right) \tag{2.11}$$

$$\mathbf{E_d} = \left(E_{xd},\ 0,\ E_{zd}\right)\exp\left(i\left(k_{xd}x + k_{zd}z - \omega t\right)\right) \tag{2.12}$$

$$\text{for} \quad z<0, \quad \mathbf{H_m} = \left(0,\ H_{ym},\ 0\right)\exp\left(i\left(k_{xm}x + k_{zm}z - \omega t\right)\right) \tag{2.13}$$

$$\mathbf{E_m} = \left(E_{xm},\ 0,\ E_{zm}\right)\exp\left(i\left(k_{xm}x + k_{zm}z - \omega t\right)\right) \tag{2.14}$$

where the wavevector components satisfy:

$$k_{xd}^2 + k_{zd}^2 = \epsilon_d k_0^2 \tag{2.15}$$

$$k_{xm}^2 + k_{zm}^2 = \epsilon_m k_0^2. \tag{2.16}$$

Here ϵ_d and ϵ_m are the permittivities of dielectric and metal respectively, the wavevector $k_0 = \omega/c = 2\pi/\lambda_0$, with λ_0 is the vacuum wavelength.

The TM-polarized fields have to satisfy the Maxwell-Faraday equation (Eq. 2.1) and Ampère's law (Eq. 2.2). Meanwhile these fields have to fulfil the boundary conditions (Eqs. 2.9 and 2.10). In this way, a dispersion relation between the wavevector k_{spp} along the propagation direction and the angular frequency ω can be derived as:

$$k_{spp}^2 = k_{xd}^2 = k_{xm}^2 = \frac{\omega^2}{c^2}\frac{\epsilon_d\epsilon_m}{\epsilon_d+\epsilon_m}. \tag{2.17}$$

By substituting into Eqs. 2.15 and 2.16, the normal component of the wavevector can also be obtained

$$k_{zd}^2 = \frac{\omega^2}{c^2}\frac{\epsilon_d^2}{\epsilon_d+\epsilon_m} \tag{2.18}$$

$$k_{zm}^2 = \frac{\omega^2}{c^2}\frac{\epsilon_m^2}{\epsilon_d+\epsilon_m}. \tag{2.19}$$

For simplicity we neglect the imaginary part of the permittivity of media. Therefore in order to have a confined wave that propagates along the interface, k_{spp} has to be real and $k_{spp} > 0$. This requires that the product and the sum of the permittivities of the two media have to be either both positive or both negative. Meanwhile the normal components of the wavevector (k_{zd} and k_{zm}) in these two media have to be purely imaginary values to confine the wave to the surface. This can only be fulfilled if the sum of the permittivities is negative. Therefore we have the conditions for a bound and propagating interface wave

as follows:

$$\epsilon_d \cdot \epsilon_m < 0, \tag{2.20}$$

$$\epsilon_d + \epsilon_m < 0. \tag{2.21}$$

Eqs. 2.20 and 2.21 require that one of the permittivities is negative, with an absolute value larger than that of the other. Metals can fulfil this requirement. Especially for noble metals like Ag and Au the absolute value of the real part of the permittivity is larger than the imaginary part at optical frequencies. So in plasmonics noble metals are always the materials in consideration.

Since this bound mode is propagating along an interface, instead of being localized in 3D, this surface plasmon is called a propagating surface plasmon polartions (SPPs), to distinguish the localized one, which will be introduced in section 2.4.

Now assume the permittivity of the metal to be

$$\epsilon_m = \epsilon'_m + i\epsilon''_m \tag{2.22}$$

where ϵ'_m and ϵ''_m are real values, with $|\epsilon'_m| \gg \epsilon''_m > 0$ for most of the noble metals like Ag and Au at optical frequencies. The permittivity of the dielectric is assumed to be a real value, $\epsilon_d > 0$, with no loss. The wavevector of the SPP propagation constant, k_{spp}, can also be expressed in the complex form $k'_{spp} + ik''_{spp}$, approximately given by:

$$k'_{spp} \approx \sqrt{\frac{\epsilon'_m \epsilon_d}{\epsilon'_m + \epsilon_d}} \frac{\omega}{c}, \tag{2.23}$$

$$k''_{spp} \approx k'_{spp} \frac{\epsilon''_m \epsilon_d}{2\epsilon'_m \left(\epsilon'_m + \epsilon_d\right)}. \tag{2.24}$$

The real part k'_{spp} determines the SPP (effective) wavelength λ_{spp}, whereas the imaginary part k''_{spp} determines the propagation length.

Under the assumption $|\epsilon'_m| \gg \epsilon_d > 0$, it is easy to find that

$$k'_{spp} \approx \sqrt{\frac{\epsilon'_m \epsilon_d}{\epsilon'_m + \epsilon_d}} \frac{\omega}{c} > \sqrt{\epsilon_d} \frac{\omega}{c} = n_d k_0 = k_d, \quad \text{and,} \tag{2.25}$$

$$\lambda_{spp} = \frac{2\pi}{k'_{spp}} \approx \sqrt{\frac{\epsilon'_m + \epsilon_d}{\epsilon'_m \epsilon_d}} \lambda_0 < \lambda_0. \tag{2.26}$$

Here k_d is the wavevector in the dielectric. Eq. 2.25 implies a wavevector mismatch between light in the dielectric and SPP, which means the SPP cannot be excited by free space light directly. Eq. 2.26 reveals that the SPP can shrink the wavelength compared to free space.

2.3.2 Excitation of SPPs at a metal surface

As revealed in the previous section the wavevector for a given wavelength in vacuum λ_0 has to increase a certain amount to couple into the SPP. There are mainly two methods, using grating couplers [3] or prism couplers [4, 5].

Grating coupler

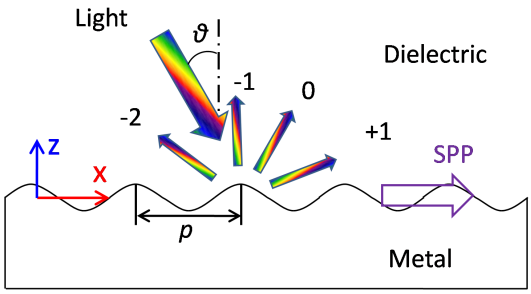

Figure 2.2: Schematic diagram of grating coupler for SPP coupling.

When light hits a grating (grating constant p) at an angle θ_0 (Fig. 2.2), light will be diffracted, giving rise to different diffraction orders. According to the Bragg condition, one obtains for the N^{th} order diffraction along the x axis [2, 6]:

$$k_{xN} = n_d k_0 \sin\theta_0 + NG, \tag{2.27}$$

where N is an integer and the diffraction order, G is the grating vector along the x-axis and its magnitude is given by $2\pi/p$. For a grating in a metal film if we choose the incident angle and the integer N properly, the diffracted light can couple with the SPP by satisfying the following condition:

$$k_x = n_d k_0 \sin\theta_0 + NG = \mathrm{Re}\left(k^g_{spp}\right). \tag{2.28}$$

Here, k^g_{spp} denotes the SPP wavevector along the grating surface. Because of the perturbation of the metal surface k^g_{spp} is different from the one at a plane interface given by Eq. 2.17. However $k^g_{spp} \approx k_{spp}$ if the perturbation is small, hence together with Eq. 2.28 we can estimate the required grating constant, incident angle and diffraction order.

For a larger perturbation the periodicity will introduce a bandgap into the surface plasmon dispersion relation, when the period is equal to half the SPP wavelength, as seen in Fig. 2.3 (a). SPP photonic bandgaps have been observed in experiments [7–9]. The bandgap is formed by the splitting of the SPP into two modes with different symmetry as shown in Fig. 2.3 (b). The symmetrical

one can be excited directly by normal incident light, due to the non-zero dipole moment along the interface, while the asymmetrical one can only be excited with tilted light. More details about these modes will be introduced when we explore the metallic gratings in chapter 4.

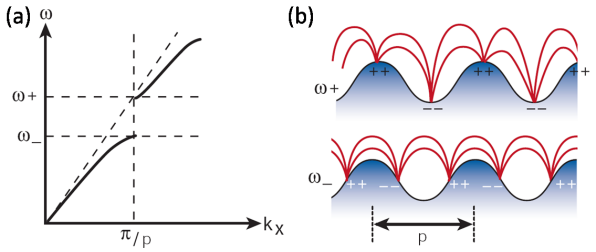

Figure 2.3: (a) A periodic textured metal surface can lead to the formation of an SPP photonic bandgap when the period, p, is equal to half the SPP wavelength. (b) There are two SPP standing wave solutions with different field and surface charge distributions [10]. ©2003 Nature Publishing Group

Prism coupler

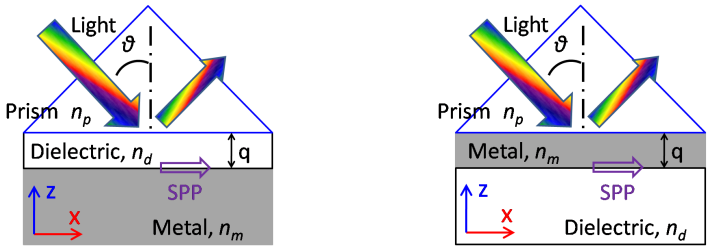

Figure 2.4: Schematic diagram of prism coupler for SPP coupling. (a) Otto configuration, (b) Kretschmann configuration.

Another approach commonly used to excite SPPs is the prism coupler, which makes use of evanescent waves. There are two configurations, Otto [4] and Kretschmann [5], as shown in Fig. 2.4. In the Otto configuration a dielectric is sandwiched between a prism and a metal film. Whereas in the Kretschmann configuration a metal film is sandwiched between a prism and a dielectric. In both cases the refractive index of the dielectric n_d has to be smaller than that of the prism n_p, $n_p > n_d$, to make wavevector matching possible.

In both the Otto and Kretschmann configuration an evanescent wave accomplishes the coupling from free space light into the SPP at the interface between the dielectric and the metal film. Coupling can only show up when the incident angle is larger than the critical angle, since the evanescent wave is only excited when total internal reflection happens. The coupling efficiency is controlled by both the incident angle in the prism θ_0 and the thickness of the middle layer in the sandwich structures. In the Kretschmann configuration the metal film can not be too thick otherwise light cannot penetrate through, usually the thickness remains below 100nm. For the Otto configuration the thickness of the dielectric layer usually varies between a few hundred nanometer and a few microns.

We note the SPP wavevector in the prism coupler as k_{spp}^{p} (the superscript 'p' denotes prism coupler approach). Due to the presence of the prism in the Otto configuration and the thin metal film in the Kretschmann configuration, k_{spp}^{p} is again different from the one of an SPP at the planar interface given by Eq. 2.17. We neglect the complexity of the evanescent wave and only impose that the wavevector along the interface has to be identical, leading to [2, 6]

$$k_x = n_p k_0 \sin\theta_0 = \mathrm{Re}\left(k_{spp}^{p}\right). \tag{2.29}$$

Therefore by tuning the incident angle θ_0 light can be coupled into the SPP. The SPP excitation will take place at the minimum of reflection.

2.4 Localized surface plasmons in spherical metallic nanoparticles

2.4.1 Mie theory

For scattering problems by spherical particles, an analytical solution is available by Mie theory (or the Mie solution) [11]. The basic idea of Mie theory is to expand the plane electromagnetic wave using vector spherical harmonics, which satisfy the vector wave equation, and then using boundary conditions around the particle. Here we outline the main procedure of getting the Mie solution. For simplicity no magnetic materials are considered.

Here only a spherical particle with radius a is considered, so it is convenient to use spherical coordinates as shown in Fig. 2.5. Let us note the field inside the particle by $(\mathbf{E}_1, \mathbf{H}_1)$, the scattered field in the surrounding medium by $(\mathbf{E}_\mathrm{s}, \mathbf{H}_\mathrm{s})$, and the incident field by $(\mathbf{E}_\mathrm{i}, \mathbf{H}_\mathrm{i})$. Therefore by superposition the total

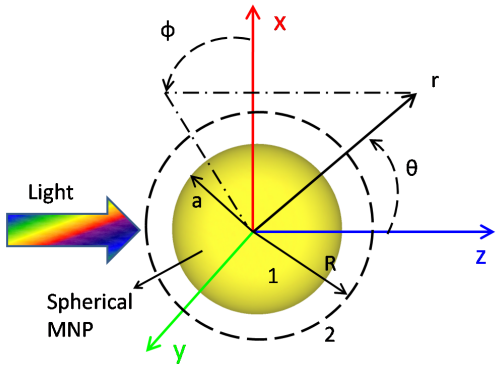

Figure 2.5: Spherical particle (radius a) with spherical coordinates.

field $(\mathbf{E}_2, \mathbf{H}_2)$ in the surrounding medium is given by

$$\mathbf{E}_2 = \mathbf{E}_\mathrm{i} + \mathbf{E}_\mathrm{s} \tag{2.30}$$

$$\mathbf{H}_2 = \mathbf{H}_\mathrm{i} + \mathbf{H}_\mathrm{s} \tag{2.31}$$

The electric and magnetic field components of an incident plane wave can be expressed as

$$\mathbf{E}_\mathrm{i} = E_0 e^{ikr\cos\theta}\hat{\mathrm{e}}_x \tag{2.32}$$

$$\mathbf{H}_\mathrm{i} = \frac{k}{\omega\mu_0} E_0 e^{ikr\cos\theta}\hat{\mathrm{e}}_y \tag{2.33}$$

with E_0 the amplitude of the incident electric field at $z = 0$, k and ω are the wave vector and the frequency of the incident plane wave respectively. μ is the permeability in vacuum, r is the radial coordinate, $\hat{\mathrm{e}}_x$ and $\hat{\mathrm{e}}_y$ are the unit vector in x and y direction. So in order to obtain the total field one needs to solve for the scattered field.

By fourier transform, a scalar wave of any form can be expanded as a plane wave series, which is expressed with harmonics (such as a function of cosine). Plane waves in cosine form are eigenfunction solutions of the homogeneous electromagnetic wave equation in cartesian coordinates. Similarly in spherical coordinates, one can also find eigenfunction solutions to the vector wave equation. These solutions are called vector spherical harmonics, **M** and **N**. For details of the derivation of vector spherical harmonics we refer to Ref [11]. As a consequence, mathematically any kind of wave may also be expressed as an expansion of vector spherical harmonics in spherical coordinates.

A plane wave described by equations 2.32 and 2.33 can be expressed by vec-

tor spherical harmonics as [11]

$$\mathbf{E}_{\mathrm{i}} = E_0 \sum_{n=1}^{\infty} i^n \frac{2n+1}{n(n+1)} \left(\mathbf{M}_{o1n}^{(1)} - i\mathbf{N}_{e1n}^{(1)} \right) \tag{2.34}$$

$$\mathbf{H}_{\mathrm{i}} = -\frac{k}{\omega\mu} E_0 \sum_{n=1}^{\infty} i^n \frac{2n+1}{n(n+1)} \left(\mathbf{M}_{e1n}^{(1)} + i\mathbf{N}_{o1n}^{(1)} \right) \tag{2.35}$$

By applying the boundary conditions

$$(\mathbf{E}_{\mathrm{i}} + \mathbf{E}_{\mathrm{s}} - \mathbf{E}_1) \times \hat{\mathbf{e}}_r = (\mathbf{H}_{\mathrm{i}} + \mathbf{H}_{\mathrm{s}} - \mathbf{H}_1) \times \hat{\mathbf{e}}_r = 0 \tag{2.36}$$

at the boundary between particle and surrounding, the scattered field $\mathbf{E}_{\mathrm{s}}$ and $\mathbf{H}_{\mathrm{s}}$ can be determined as

$$\mathbf{E}_{\mathrm{s}} = E_0 \sum_{n=1}^{\infty} i^n \frac{2n+1}{n(n+1)} \left(i a_n \mathbf{N}_{e1n}^{(3)} - b_n \mathbf{M}_{o1n}^{(3)} \right) \tag{2.37}$$

$$\mathbf{H}_{\mathrm{s}} = \frac{k}{\omega\mu} E_0 \sum_{n=1}^{\infty} i^n \frac{2n+1}{n(n+1)} \left(i b_n \mathbf{N}_{o1n}^{(3)} + a_n \mathbf{M}_{e1n}^{(3)} \right) \tag{2.38}$$

And for the internal fields:

$$\mathbf{E}_1 = E_0 \sum_{n=1}^{\infty} i^n \frac{2n+1}{n(n+1)} \left(c_n \mathbf{M}_{o1n}^{(1)} - i d_n \mathbf{N}_{e1n}^{(1)} \right) \tag{2.39}$$

$$\mathbf{H}_1 = -\frac{k_1}{\omega\mu} E_0 \sum_{n=1}^{\infty} i^n \frac{2n+1}{n(n+1)} \left(d_n \mathbf{M}_{e1n}^{(1)} + i c_n \mathbf{N}_{o1n}^{(1)} \right) \tag{2.40}$$

where superscripts (1) and (3) denote the use of first kind Bessel functions j_n and first kind Hankel functions $h_n^{(1)}$. Subscripts $(e1n)$ and $(o1n)$ are illustrated in Ref [11]. Coefficients a_n, b_n, c_n and d_n are

$$a_n = \frac{m\psi(mx)\psi_n'(x) - \psi(x)\psi_n'(mx)}{m\psi(mx)\xi_n'(x) - \xi(x)\psi_n'(mx)} \tag{2.41}$$

$$b_n = \frac{\psi(mx)\psi_n'(x) - m\psi(x)\psi_n'(mx)}{\psi(mx)\xi_n'(x) - m\xi(x)\psi_n'(mx)} \tag{2.42}$$

$$c_n = \frac{m\psi(x)\xi_n'(x) - m\xi(x)\psi_n'(x)}{\psi(mx)\xi_n'(x) - m\xi(x)\psi_n'(mx)} \tag{2.43}$$

$$d_n = \frac{m\psi(x)\psi_n'(x) - m\xi(x)\psi_n'(x)}{m\psi(mx)\xi_n'(x) - \xi(x)\psi_n'(mx)} \tag{2.44}$$

where the size parameter x and relative refractive index m are

$$x = ka = \frac{2\pi n_s a}{\lambda} \tag{2.45}$$

$$m = \frac{n_p}{n_s} \tag{2.46}$$

n_s and n_p are the refractive indices of surrounding and particle respectively; ψ and ξ are Riccati-Bessel functions:

$$\psi(\rho) = \rho j_n'(\rho) \tag{2.47}$$

$$\xi(\rho) = \rho h_n'(\rho) \tag{2.48}$$

For a non-absorbing surrounding medium, there are usually three main factors used to characterize the properties of a particle: extinction efficiency σ_{ext}, scattering efficiency σ_{sca} and absorption efficiency σ_{abs}. Related factors with dimension of area are obtained by multiplying these three efficiencies with the area of the cross section of the particle (πa^2), i.e. extinction cross section C_{ext}, scattering cross section C_{sca} and absorption cross section C_{abs}. They are determined by the scattering coefficients a_n and b_n, and expressed as

$$\sigma_{sca} = \frac{2}{x^2}\sum_{n=1}^{\infty}(2n+1)\left(|a_n|^2 + |b_n|^2\right) \tag{2.49}$$

$$\sigma_{ext} = \frac{2}{x^2}\sum_{n=1}^{\infty}(2n+1)\,\mathrm{Re}\,(a_n + b_n) \tag{2.50}$$

$$\sigma_{abs} = \sigma_{ext} - \sigma_{sca} \tag{2.51}$$

2.4.2 Basic properties of metallic nanoparticles

Figure 2.6 shows the influence of silver nanoparticle diameter D_{MNP} on LSP resonances, with the particle embedded in a non-absorbing material with refractive index n_{sur} = 1.5. These results are calculated with the Mie theory in section 2.4.1 using MATLAB [12] (more details for MATLAB implementation of Mie theory see later section 2.6.1). There are several features:

1. For small diameter, only the dipole mode is excited, which corresponds to $a_1 \neq 0$, $a_n (n > 1)$ and b_n (for any n) have negligible value.

2. The dipole mode red-shifts as the diameter D_{MNP} increases.

3. Higher order modes show up at lower wavelengths as D_{MNP} increases.

4. Scattering dominates for large particles. In contrast absorption by the particle dominates for small particles.

For the dipole mode, there should be no retardation across the whole particle in the direction of the incident wave. As a consequence, for particles with diameter smaller than the wavelength only the dipole mode can be exited. The

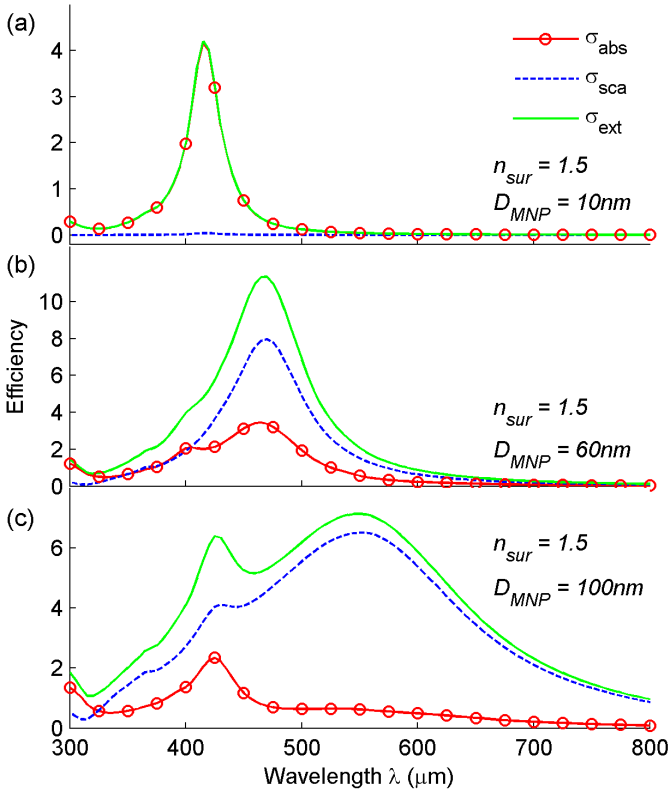

Figure 2.6: Influence of spherical silver nanoparticle size on LSP (calculated with Mie theory in MATLAB). Green lines are the extinction efficiencies, red lines the absorption efficiencies, and blue lines the scattering efficiencies.

dipole mode red-shifts to satisfy the no retardation requirement for larger particles. When the diameter increases further and becomes comparable with the wavelength, a higher order quadrupole shows up (Fig. 2.6 (c)).

Figure 2.7 shows the dependence of the LSP resonance on the surrounding media. Resonances red-shift as the surrounding refractive index increases. Therefore the LSP of metal nanoparticles is quite sensitive to the size of the particle, and to the surrounding material (and also the particle shape, but here we only consider spherical particles).

Figure 2.8 shows near-field distributions (normalized by the incident field) for different MNP sizes at resonance. Compared with larger particles, a stronger enhanced near-field can be observed for small ones. The retardation effects play an increasingly important role as the MNP size increases.

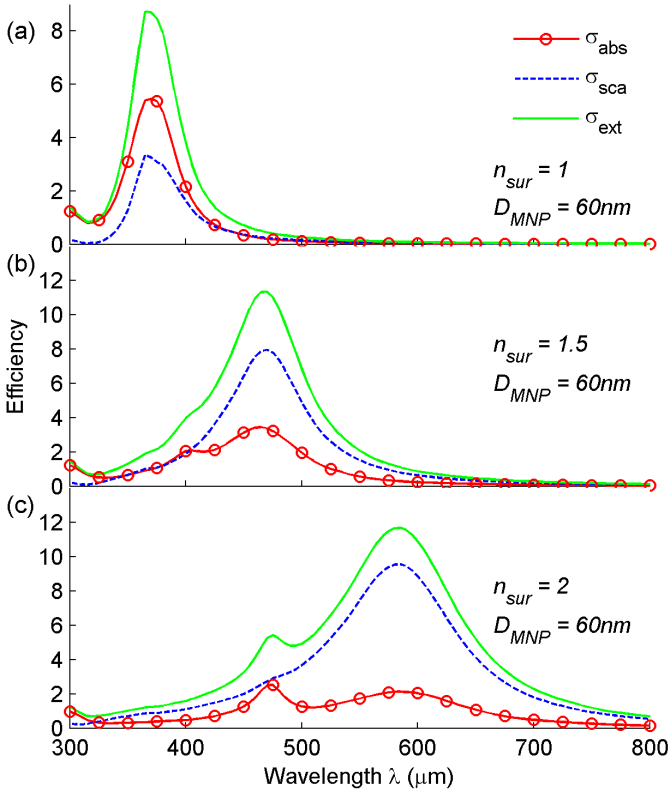

Figure 2.7: Influence of surrounding medium on LSP of spherical silver nanoparticles (calculated with Mie theory in MATLAB). Green lines are the extinction efficiencies, red lines the absorption efficiencies, and blue lines the scattering efficiencies.

For particles smaller than the wavelength, the fields in Eq. 2.37 and 2.38 can be approximated by only including the a_1 terms, yielding:

$$\begin{aligned}\mathbf{E}_s &= E_0 \sum_{n=1}^{\infty} i^n \frac{2n+1}{n(n+1)} \left(i a_n \mathbf{N}^{(3)}_{e1n} - b_n \mathbf{M}^{(3)}_{o1n} \right) \\ &\cong -\frac{3}{2} E_0 a_1 \mathbf{N}^{3}_{e1n} \propto E_0 \frac{n_p^2 - n_s^2}{n_p^2 + 2n_s^2}\end{aligned} \tag{2.52}$$

where we see that the amplitude of $\mathbf{E}_s$ reaches its maximum when

$$\begin{aligned}&n_p^2 + 2n_s^2 = 0, \text{or}: \\ &\epsilon_p + 2\epsilon_s = 0.\end{aligned} \tag{2.53}$$

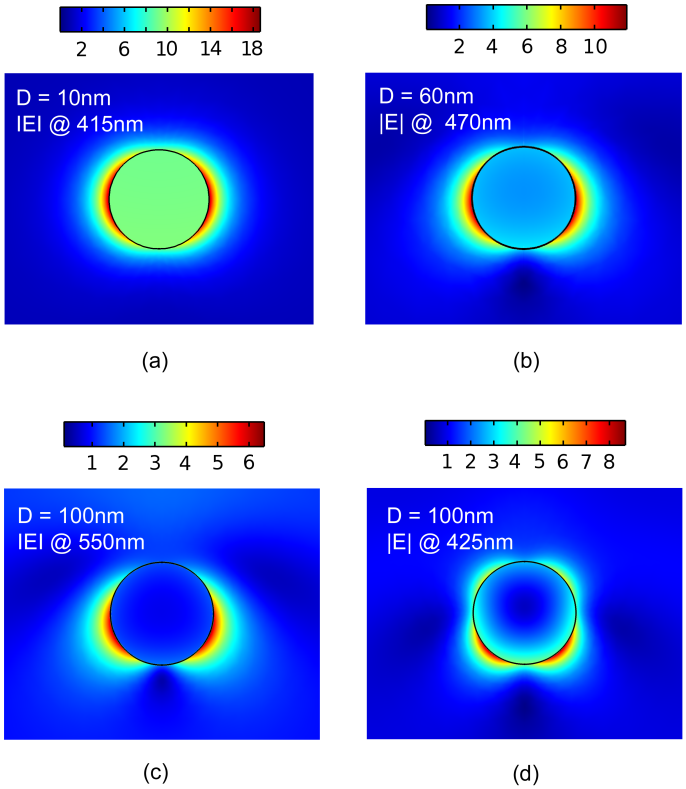

Figure 2.8: Electric field distributions normalized by the incident field for spherical MNPs with different diameter at wavelengths corresponding to peaks in Fig 2.6 (calculated with Mie theory in MATLAB). Plots are across the center of the sphere. A plane wave is incident from the top, and the incident E field is in plane to the plots. (a)–(c) correspond to dipole modes for diameters of 10nm, 60nm and 100nm respectively, (d) is the quadrupole mode for a diameter of 100nm.

Therefore for simplicity one can use Eq. 5.7 to estimate the position of an LSP resonance.

For non-spherical particles, the LSP resonance can be tuned by shape. The LSP resonances of different shapes of Ag nanoparticles have been summarized in [13], the LSP resonance can be tuned in a large wavelength range for different applications.

2.4.3 Extended Mie theory

In the previously discussed classic Mie theory, the surrounding is assumed to be non-absorbing, and only in this case the three efficiency factors (σ_{ext}, σ_{sca} and σ_{abs}) are valid. In lossy media, the previous formulation for Mie theory is still available only if we use the complex refractive index for the surrounding medium [14–21], except that these three factors can not be used any longer. However based on extended Mie theory some interesting rigorous formulations can be derived [18–21].

Let us consider an imaginary sphere with radius R ($R > a$) centered at the origin (also the center of the particle) as shown in Fig. 2.5. The power that crosses the surface A of this imaginary sphere is given by the integral of the time-averaged Poynting vector $\langle \mathbf{S} \rangle$ over the surface A ("$\langle\rangle$" denotes the time-average)

$$\begin{aligned} W_{abs}(R) &= -\int_A \langle \mathbf{S} \rangle \cdot \hat{\mathrm{e}}_r \, dA \\ &= -\frac{1}{2}\mathrm{Re}\int_A \left[(\mathbf{E}_\mathrm{i} + \mathbf{E}_\mathrm{s}) \times \left(\mathbf{H}_\mathrm{i}^* + \mathbf{H}_\mathrm{s}^* \right) \right] \cdot \hat{\mathrm{e}}_r \, dA \\ &= -\frac{1}{2}\mathrm{Re}\int_A \left(\mathbf{E}_\mathrm{i} \times \mathbf{H}_\mathrm{i}^* \right) \cdot \hat{\mathrm{e}}_r \, dA - \frac{1}{2}\mathrm{Re}\int_A \left(\mathbf{E}_\mathrm{s} \times \mathbf{H}_\mathrm{s}^* \right) \cdot \hat{\mathrm{e}}_r \, dA \\ &\quad - \frac{1}{2}\mathrm{Re}\int_A \left(\mathbf{E}_\mathrm{i} \times \mathbf{H}_\mathrm{s}^* + \mathbf{E}_\mathrm{s} \times \mathbf{H}_\mathrm{i}^* \right) \cdot \hat{\mathrm{e}}_r \, dA \\ &= W_i - W_{sca} + W_{ext} \end{aligned} \tag{2.54}$$

where W_i is the incident power, W_{sca} the scattered power and W_{ext} the cross term. If $W_{abs} > 0$, energy is absorbed within the imaginary sphere.

Substituting the scattered field from Eqs. 2.37 and 2.38, and the incident field from Eqs. 2.34 and 2.35, we can get

$$\begin{aligned} W_i(R) &= -\frac{1}{2}\mathrm{Re}\int_A \left(\mathbf{E}_\mathrm{i} \times \mathbf{H}_\mathrm{i}^* \right) \cdot \hat{\mathrm{e}}_r \, dA \\ &= \frac{\pi |E_0|^2}{\omega \mu_0} \sum_{n=1}^{\infty} (2n+1)\,\mathrm{Im}\left(\frac{\psi_n \psi_n'^* - \psi_n' \psi_n^*}{k} \right) \end{aligned} \tag{2.55}$$

$$\begin{aligned} W_{sca}(R) &= \frac{1}{2}\mathrm{Re}\int_A \left(\mathbf{E}_\mathrm{s} \times \mathbf{H}_\mathrm{s}^* \right) \cdot \hat{\mathrm{e}}_r \, dA \\ &= \frac{\pi |E_0|^2}{\omega \mu_0} \sum_{n=1}^{\infty} (2n+1)\,\mathrm{Im}\left(\frac{|a_n|^2 \xi_n' \xi_n^* - |b_n|^2 \xi_n \xi_n'^*}{k} \right) \end{aligned} \tag{2.56}$$

$$
\begin{aligned}
W_{ext}(R) &= -\frac{1}{2}\mathrm{Re}\int_A \left(\mathbf{E}_\mathrm{i}\times\mathbf{H}_\mathrm{s}^* + \mathbf{E}_\mathrm{s}\times\mathbf{H}_\mathrm{i}^*\right)\cdot\hat{\mathbf{e}}_r\, dA \\
&= \frac{\pi|E_0|^2}{\omega\mu_0}\sum_{n=1}^{\infty}(2n+1) \\
&\times \mathrm{Im}\left(\frac{a_n^*\psi_n'\xi_n^* - b_n^*\psi_n\xi_n'^* + a_n\xi_n'\psi_n^* - b_n\xi_n\psi_n'^*}{k}\right)
\end{aligned}
\tag{2.57}
$$

$$
\begin{aligned}
W_{abs}(R) &= W_i - W_{sac} + W_{ext} \\
&= \frac{\pi|E_0|^2}{\omega\mu_0}\sum_{n=1}^{\infty}(2n+1) \\
&\times \mathrm{Im}\left(\frac{\left(b_n\xi_n-\psi_n\right)\left(b_n^*\xi_n'^*-\psi_n'^*\right)-\left(a_n\xi_n'-\psi_n'\right)\left(a_n\xi_n^*-\psi_n^*\right)}{k}\right)
\end{aligned}
\tag{2.58}
$$

Using the formulation above, one can calculate the absorption included inside any sphere in a homogenous medium and other factors to investigate the influence of particles on the absorption in the surrounding [20, 21]. We will show some studies based on this formulation for metallic nanoparticles in the next chapter.

2.5 Localized surface plasmons of a nanowire

Many metallic nanostructures are explored and used in photonic applications, with nanowires being quite common. Therefore it is useful to theoretically analyze the LSP modes associated with a nanowire. We model the nanowire as an infinitely long cylinder, provided that the aspect ratio is large enough. The analysis procedure is similar to spherical particles, except that the wave equation is solved in cylindrical polar coordinates. In the following only the basic idea is outlined. For simplicity the case with incidence direction and E-field polarization perpendicular to the cylinder axis is considered. For more details readers are referred to [11].

Similarly, for the cylindrical case, vector cylindrical harmonics, $\mathbf{M}_n$ and $\mathbf{N}_n$, can be obtained [11]. We can represent the incident plane wave as an expansion of these harmonics [11]:

$$
\mathbf{E}_\mathrm{i} = \sum_{n=-\infty}^{\infty} E_n\mathbf{N}_n^{(1)} \tag{2.59}
$$

$$
\mathbf{H}_\mathrm{i} = \frac{-ik}{\omega\mu}\sum_{n=-\infty}^{\infty} H_n\mathbf{M}_n^{(1)} \tag{2.60}
$$

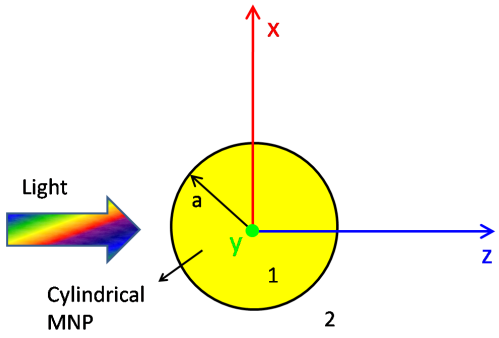

Figure 2.9: Infinitely long cylinder with light incidence normal to its axis.

where $E_n = E_0(-i)^n/k$.

Meanwhile the solution inside the cylinder and for the scattered field is also expanded:

$$\mathbf{E}_s = -\sum_{n=-\infty}^{\infty} E_n\left(b_n\mathbf{N}_n^{(3)} + ia_n\mathbf{M}_n^{(3)}\right) \tag{2.61}$$

$$\mathbf{H}_s = \frac{ik}{\omega\mu}\sum_{n=-\infty}^{\infty} E_n\left(b_n\mathbf{M}_n^{(3)} + ia_n\mathbf{N}_n^{(3)}\right) \tag{2.62}$$

$$\mathbf{E}_1 = -\sum_{n=-\infty}^{\infty} E_n\left(g_n\mathbf{M}_n^{(1)} + f_n\mathbf{N}_n^{(1)}\right) \tag{2.63}$$

$$\mathbf{H}_1 = \frac{ik}{\omega\mu}\sum_{n=-\infty}^{\infty} E_n\left(g_n\mathbf{N}_n^{(1)} + f_n\mathbf{M}_n^{(1)}\right) \tag{2.64}$$

The final step is to couple these expansions together by applying the boundary conditions, in order to get the scattering coefficients. For the case we consider a_n vanishes, and b_n becomes:

$$b_n = \frac{J_n(mx)J_n'(x) - mJ_n'(mx)J_n(x)}{J_n(mx)H_n^{(1)\prime}(x) - mJ_n'(mx)H_n^{(1)}(x)} \tag{2.65}$$

where J_n and $H_n^{(1)}$ are the first kind Bessel function and Hankel function.

For cylinders with a small diameter, one can also get a quasi-static approximation to estimate the resonant wavelength of the LSP:

$$\begin{aligned} &n_p^2 + n_s^2 = 0, \text{or}: \\ &\epsilon_p + \epsilon_s = 0. \end{aligned} \tag{2.66}$$

2.6 Optical modeling

2.6.1 MATLAB implementation of (extended) Mie theory

For a single spherical MNP embedded in a surrounding medium the (extended) Mie theory provides its properties. Algorithms for implementing Mie theory in programs have been reported [22]. MATLAB provides several well implemented functions e.g. for Bessel functions with good performance [12]. One main problem with the implementation is the number of spherical harmonics that needs to be taken into account. Examining the equations in section 2.4.1 there are always infinite sums involved for the coefficients (a_n, b_n, c_n and d_n). A well examined convergence criterion for the number of orders N, is [22]:

$$N = \begin{cases} x + 4x^{1/3} + 1, & x \in [0.02, 8] \\ x + 4.05x^{1/3} + 2, & x \in (8, 4200] \\ x + 4x^{1/3} + 2, & x \in (4200, 20000] \end{cases} \tag{2.67}$$

where x is the size parameter defined in Eq. 2.45.

By applying this convergence criterion we can implement the (extended) Mie theory in MATLAB. We can use it to calculate the efficiencies as shown in Fig. 2.6 and 2.7, field distribution as seen in Fig. 2.8, the influence of MNPs on the absorption in the surrounding as discussed in the next chapter and so on. It provides us with a faster estimation of the properties of MNPs than with other numerical methods like FEM.

2.6.2 Finite element methods and COMSOL

For non-spherical or non-cylindrical particles and complicated optical structures, there is usually no analytical solution for their interaction with light because of the complicated boundaries. Therefore one has to rely on the various numerical methods available. In our work we mainly used the Finite Element Method (FEM), implemented in the commercial package COMSOL [23]. The RF module in COMSOL provides a wide range of modeling capabilities for all kinds of optical systems. It can be used to perform light propagation, eigen-frequency solving and so on.

FEM is a very important numerical method, not only for electromagnetics. Compared with the finite difference time domain (FDTD) method, FEM is much more suitable for some complex geometries with curved boundaries due to its meshing techniques. In FEM triangular (2D) or tetrahedral (3D) meshes are often used, which can approximate curved boundaries much better than the rectangular (2D) and cubic (3D) meshes employed in FDTD. Another advantage over FDTD is that it allows the user to input measured material properties instead of employing fittings via some analytical model (e.g. the Drude model for

optical constants used in FDTD). Since this work uses established FEM software to model solar cells, and does not develop a source code, here we only summarize the basic idea behind FEM for solving Maxwell's equations.

Let us consider a 2D problem, the governing scalar Helmholtz equation in a homogeneous medium is:

$$\nabla^2\phi + k^2\phi = 0. \tag{2.68}$$

In solving for the primary unknown quantity ϕ under certain boundary conditions by FEM, the following general steps are involved:

- Discretization of the geometry under investigation, e.g. triangular meshing as shown in Fig. 2.10(a);

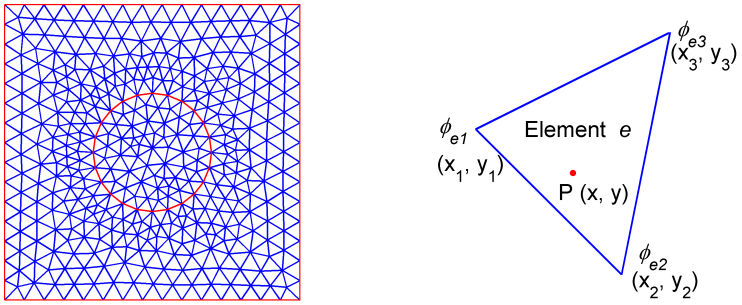

Figure 2.10: (a) Triangular mesh example in a model consisting of shapes of a rectangle and a circle. (b) A single mesh element.

- Find proper interpolation functions (also called shape functions) ϕ_e, usually a set of polynomials. The accuracy of the solution depends on the order of these polynomials, e.g. linear, quadratic or even higher orders. Here for simplicity let us consider linear ones $\phi_e = a + bx + cy$. In each triangular mesh element e, ϕ_e is interpolated based on the values at the nodes or those at edges, depending if nodal elements or edge elements are used. For a nodal element, ϕ_e at any point P inside element e (see Fig. 2.10(b)) can be expressed as:

$$\phi_e = \sum_{i=1}^{3} u_i \phi_{ei}, \tag{2.69}$$

where ϕ_{ei} is the value of ϕ_e at nodes (the vertices of the mesh), u_i is known as a barycentric or area coordinate, a value dependent on the coordinates. Therefore to get the solution of the primary unknown quantity ϕ in the whole geometry domain, one only has to get the numerical solution of its values at nodes.

- To get the numerical solution of ϕ_e, one converts the governing equation Eq. 2.68 to an integro-differential formulation. Usually there are two methods to do so, using a functional or the weighted-residual method. The functional $F(\phi)$ of the governing equation can be obtained by calculating the energy in the system under investigation from the Poynting theorem and one obtains here:

$$F(\phi) = \sum_{e=1}^{N_e} \iint_{A_e} \frac{1}{2} \left[\left(\frac{\partial \phi_e}{\partial x} \right)^2 + \left(\frac{\partial \phi_e}{\partial y} \right)^2 - k^2 \phi_e \right] ds, \tag{2.70}$$

  where N_e is the total number of mesh elements, A_e is the area of element e. The weighted-residual method is obtained directly from the governing equation by transferring all terms of the equation on one side and then multiplying by a weight function w_e:

$$W(\phi) = \sum_{e=1}^{N_e} \iint_{A_e} w_e \left(\nabla^2 \phi_e + k^2 \phi_e \right) ds. \tag{2.71}$$

  By minimizing $F(\phi)$ or $W(\phi)$ one obtains a numerical solution of ϕ_e.

For more details involved in each step we refer to Ref. [24–26].

With FEM one obtains numerical solutions of field distributions (both electric and magnetic) in optical systems such as OSCs. Based on these distributions postprocessing can be performed to calculate parameters of interest. To get accurate solutions the mesh is a very important issue. Usually the maximum mesh size in the medium is determined as $\lambda/6$, where λ is the wavelength in the material. For some special cases in which the field intensity gradient is larger a finer mesh is necessary. For example LSPs and SPPs appear in a very small area and decay very rapidly from the metal interfaces. For these cases a fine mesh on the order of the skin depth has to be adopted along the interfaces. In general, to find a proper mesh size one can always perform a convergence investigation.

In modeling it is often impossible to include the whole solar cell structure in the computational domain. Certain techniques have to be applied to truncate the OSC structure in computations. The RF module of COMSOL provides various boundary conditions to reduce the computational domain. For instance one can apply periodic boundary conditions to use only one unit cell of a periodic structure. There are other boundary conditions for symmetries available, such as perfect electric and magnetic conductors which force the electric and magnetic field perpendicular to the boundaries, respectively. For cases with open boundaries an important trick to reduce the model size is the perfectly matched layer (PML). PML is an artificial absorbing layer enclosing the model to absorb outgoing light from the model. In COMSOL a key point of using PML is to set its material property the same as the one next to it.

Another important issue is the setup of a light source which provides the input excitation. For an optical system enclosed in a homogeneous medium, like a MNP in air, one can use the scattered field formulation in COMSOL, in which a plane wave background field is applied. For an OSC with light illuminating from air, the optically thick glass substrate is usually modeled as semi-infinite, omitting the bottom air/glass interface. In such a system the OSC is enclosed in two semi-infinite media (the glass substrate and the air on the other side) instead of in a single homogeneous medium. Therefore one has to use 'port' together with 'assembly' in COMSOL to introduce a light source to the model. For more techniques for light sources one is referred to the COMSOL documentation and online forum [23].

References

[1] S. A. Maier. *Plasmonics: Fundamentals and Applications.* Springer Verlag, 2007.

[2] H. Raether. *Surface Plasmons on Smooth and Rough Surfaces and on Gratings.* Springer, Berlin, 1988.

[3] R. H. Ritchie, E. T. Arakawa, J. J. Cowan, and R. N. Hamm. *Surface-plasmon resonance effect in grating diffraction.* Physical Review Letters, 21(22):1530–1533, 1968.

[4] A. Otto. *Excitation of nonradiative surface plasma waves in silver by the method of frustrated total reflection.* Zeitschrift für Physik A Hadrons and Nuclei, 216(4):398–410, 1968.

[5] E. Kretschmann and H. Raether. *Radiative decay of non radiative surface plasmons excited by light.* Zeitschrift Fuer Naturforschung, Teil A, 23:2135, 1968.

[6] J. Homola, editor. *Surface Plasmon Resonance Based Sensors*, volume 4. Springer Verlag, 2006.

[7] W. Barnes, T. Preist, S. Kitson, and J. Sambles. *Physical origin of photonic energy gaps in the propagation of surface plasmons on gratings.* Physical Review. B, Condensed matter, 54(9):6227–6244, 1996.

[8] S. C. Kitson, W. L. Barnes, and J. R. Sambles. *Full photonic band gap for surface modes in the visible.* Physical Review Letters, 77(13):2670–2673, 1996.

[9] W. L. Barnes, S. C Kitson, T. W. Preist, and J. R. Sambles. *Photonic surfaces for surface-plasmon polaritons.* Journal of Optical Society of America A, 14(7):1654–1661, 1997.

[10] W. L. Barnes, A. Dereux, and T. W. Ebbesen. *Subwavelength optics.* Nature, 424:824–830, 2003.

[11] C. F. Bohren and D. R. Huffman. *Absorption and Scattering of Light by Small Particles.* John Wiley and Sons, New York, 1983.

[12] MATLAB. http://www.mathworks.com/.

[13] M. Rycenga, C. M. Cobley, J. Zeng, W. Li, C. H. Moran, Q. Zhang, D. Qin, and Y. Xia. *Controlling the synthesis and assembly of silver nanostructures for plasmonic applications.* Chemical Reviews, 111(6):3669–712, 2011.

[14] W. C. Mundy, J. A. Roux, and A. M. Smith. *Mie scattering by spheres in an absorbing medium.* Journal of the Optical Society of America. A, 64(12):1593–1597, 1974.

[15] P. Chýlek. *Light scattering by small particles in an absorbing medium.* Journal of the Optical Society of America. A, 67(4):561–563, 1977.

[16] C. F. Bohren and D. P. Gilra. *Extinction by a spherical particle in an absorbing medium.* Journal of Colloid and Interface Science, 72(2):215–221, 1979.

[17] M. Quinten and J. Rostalski. *Lorenz-Mie Theory for spheres immersed in an absorbing host medium.* Particle and Particle Systems Characterization, 13(2):89–96, 1996.

[18] A. N. Lebedev, M. Gartz, U. Kreibig, and O. Stenzel. *Optical extinction by spherical particles in an absorbing medium: application to composite absorbing films.* The European Physical Journal D, 6(3):365–373, 1999.

[19] I. W. Sudiarta and P. Chylek. *Mie-scattering formalism for spherical particles embedded in an absorbing medium.* Journal of the Optical Society of America A, 18(6):1275–8, 2001.

[20] L. Hu, X. Chen, and G. Chen. *Surface-Plasmon Enhanced Near-Bandgap Light Absorption in Silicon Photovoltaics.* Journal of Computational and Theoretical Nanoscience, 5(11):2096–2101, 2008.

[21] J. Y. Lee and P. Peumans. *The origin of enhanced optical absorption in solar cells with metal nanoparticles embedded in the active layer.* Optics Express, 18(10):10078–87, 2010.

[22] W. J. Wiscombe. *Improved Mie scattering algorithms.* Applied Optics, 19(9):1505–1509, 1980.

[23] Comsol Multiphysics. http://www.comsol.com.

[24] J. Jin. *The Finite Element Method in Electromagnetics.* John Wiley and Sons, New York, 1993.

[25] M. K. Haldar. *Introducing the Finite Element Method in electromagnetics to undergraduates using MATLAB.* International Journal of Electrical Engineering Education, 43(3):232–244, 2006.

[26] A. C. Polycarpou. *Introduction to the Finite Element Method in Electromagnetics.* Morgan & Claypool Publishers, 2005.

3
Metallic nanoparticles

3.1 Introduction

Organic solar cells (OSCs) are of great current interest as they have a strong potential to reduce the cost of photovoltaics [1]. However, OSCs still have low efficiency, up to 10.6% [2], due to the short exciton diffusion length, low charge mobility, limited absorption band and energy levels of polymers. This efficiency is much smaller than for commercial silicon-based solar cells. The short exciton diffusion length in OSCs limits the thickness of the active layer. The advanced BHJ concept was introduced to solve the diffusion length problem and to keep the required thickness of the active layer for sufficient light absorption [3].

However, in spite of using a BHJ, the thickness cannot be too large. Above a certain thickness the conversion efficiency drops because free carrier recombination becomes significant [4]. Meanwhile increased internal resistance with thickness will yield a low filling factor. Several approaches have been proposed and reported to overcome weak absorption of OSCs: folded structures [5], tandem cell architectures [6–8], new materials for the active layer [9, 10], and metallic nanoparticles (MNPs) [6, 8, 11–14, 14–21].

Metallic nanoparticles tend to excite LSPs, with possibly a very strong scattering or near-field enhancement. From Mie theory, as explained in the previous chapter, section 2.4.2, one finds that for particles with size smaller than around 30nm, the near-field enhancement dominates [22] since only the dipole

mode is supported. For particles with size larger than 50nm the scattering effect is more significant [23, 24]. For larger particles with size comparable to the wavelength retardation will come into effect, so that the higher order modes can be excited. Consequently the scattering effects dominate. The different size regimes point to two different ways to take advantage of LSPs. First, the strong scattering can be used to redirect light more horizontally into the active layer. Second, we can use enhanced near-fields, so that light spends more time around a particle.

Several experiments and numerical investigations on the influence of MNPs in inorganic solar cells have been performed [23, 25–37]. In these studies large MNPs are very often used and placed on top of the cells. The main idea is to enhance the light path by exploiting the large forward scattering from MNPs and the guided modes and other effects in the active layer. These cells have layers with thicknesses e.g. in the range of micrometers (for Si thin-film) or ~ 300nm (for amorphous Si), which are compatible with the larger diameter particles demanded for efficient scattering. In addition, these thicker solar cell materials have a lower, wide-band absorption, compared to organic materials.

There were also experiments and simulations conducted to investigate the influence of MNPs on OSCs. Usually in these investigations MNPs were embedded between the anode and the active layer [11–14], between tandem cells [6, 8], between active layer and cathode [14], or inside the active layer [15, 17–21]. In many experiments the particles tend to be incorporated inside the cells, and usually only have a size on the order of 10nm, which is limited by the thin thickness of layers demanded for good internal efficiency. As a result this makes the utilization of the prominent scattering of MNPs with large particles difficult. Therefore absorption and efficiency enhancements observed in these experiments should be mainly attributed to the near-field effects. Indeed, as shown later, incorporating MNPs in the buffer layer (usually PEDOT:PSS) is not that promising from the optics viewpoint.

For small particles only the near-field effects with the dipole mode form a potential for light harvesting. They can only be effective when incorporating inside the active layer. There are some recent reports about embedding silver nanoparticles directly or partially into the active layer [5, 9, 10, 18, 19]. These types of configurations can lead to very good absorption enhancement factors, however provided that the active layer is very thin, about 30–50nm thick [21]. Therefore, we are mainly driven towards near-field enhancement, leading to strong optical fields in the neighborhood of small particles. However recently reports on large MNPs have also shown its promising potential to boost the efficiency [38].

In this chapter we address optical aspects in using MNPs to enhance the efficiency of OSCs by means of Finite Element Method (FEM). These problems

concern such as which metal is the most promising candidate, where should the MNPs be embedded, what mechanism is behind the efficiency enhancement and so on. First in section 3.2 a single particle is studied to illustrate some basic properties of MNPs in absorbing media using Mie theory. In the next three sections, 3.3, 3.4 and 3.5, we will exploit the near-field of MNPs for efficiency enhancements of OSCs. In section 3.3, we reduce the 3D problem to a 2D one, since simulations have shown that a 2D model can give similar results to a 3D model [39]. The advantages of this reduction are of course computational time- and memory saving, and it allows us to investigate a larger parameter space in more detail. We discuss where the nanowire array should be embedded and how different parameters of the MNP array affect the enhancement. In addition we investigate the enhancement mechanism and analyze the absorption spectra in detail. In section 3.4 based on a 3D model we discuss the MNP material choice. In section 3.5, experiments from co-workers together with simulations are presented for Ag islands covered by two different organic materials, CuPc and SubPc respectively. In section 3.6 strong scattering by larger particles is investigated, in order to investigate this alternative approach.

3.2 A single spherical particle

Several different metals (Ag, Au, Al...) have been studied for plasmonic photovoltaic applications. Figure 3.1 shows the permittivities of Ag, Au and Al [40]. For bulk metal Ag and Al have lower loss in the visible light range compared to Au, the loss in a thick metal film is shown in Fig. 3.2(a). Ag has interband transitions (leading to absorption losses) only for low wavelengths (below $\sim$ 350nm) which means that at higher wavelengths the losses for Ag are relatively small. For Au the loss is significant below $\sim$ 550nm due to two interband transitions at $\sim$ 330nm and $\sim$ 470nm. (The interband transitions also play an important role in determining the plasmonic modes in MNPs.) However the loss in Al overrides Ag and Au at large wavelengths.

Now we consider a spherical NP surrounded by an absorbing medium, the same configuration as illustrated in Fig. 2.5. The surrounding is assumed to have a refractive index $2 + 0.1i$ across the whole visible light range (a time dependence of $e^{-i\omega t}$ used to be consistent with Mie theory discussed previously), which is typically the refractive index of a polymer or small molecule material. To calculate the absorbed power, $W_{abs}(R)$, in the surrounding material inside an arbitrary imaginary sphere with a radius of R, the extended Mie theory can be applied. Therefore we define a figure of merit, absorption enhancement (AE), to assess the improvement of light harvesting in the absorbing surround-

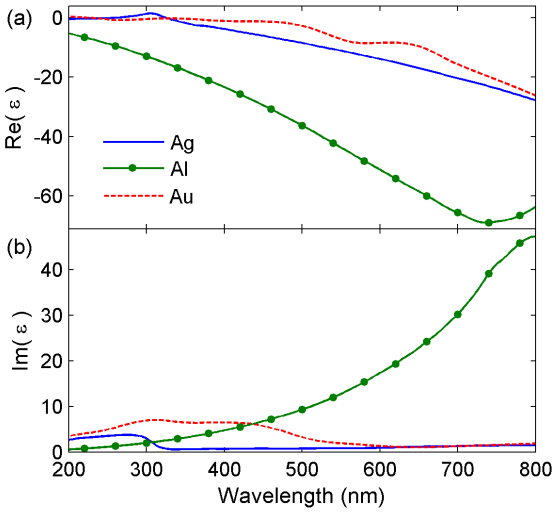

Figure 3.1: Real part (a) and imaginary part (b) of permittivities of Ag, Au and Al.

ing medium:

$$AE = \frac{W^{w}_{abs}(R) - W^{w}_{abs}(a)}{W^{wo}_{abs}(R)} \tag{3.1}$$

where the superscripts w and wo denote the case with and without NP respectively.

Figure 3.3 shows the absorption enhancement for different materials. The radius of the NP is chosen to be 5nm. For the R equal to a, the enhancement is zero since no medium is included. For large R the enhancement should limit to 1 since the enhanced near-field decays very quickly. For small R ($R > a$) due to the enhanced near-field a maximum enhancement can be observed in the range 1.2a–1.6a. The absorption enhancement is largest for silver with an enhancement factor of 30, whereas 15 for Ag and about 6 for Al is observed (in the wavelength range 300nm to 800nm, but at UV it can have a factor of 18). This makes Ag probably the most promising for applications in photovoltaics and other photonic fields. Note that for different materials the maximum absorption enhancement shows in a different wavelength range, where the LSP of each metal is located. Because of the small size of particles, these resonances correspond to the dipole mode. Considering the dipole, the absorption enhancement is mainly located laterally in the vicinity of the NP as the enhanced field profile shown in Fig. 2.8.

Figure 3.2(b) shows the absorbed power (normalized with arbitrary unit) in particles with 10nm diameter for different materials. Loss in particles falls in

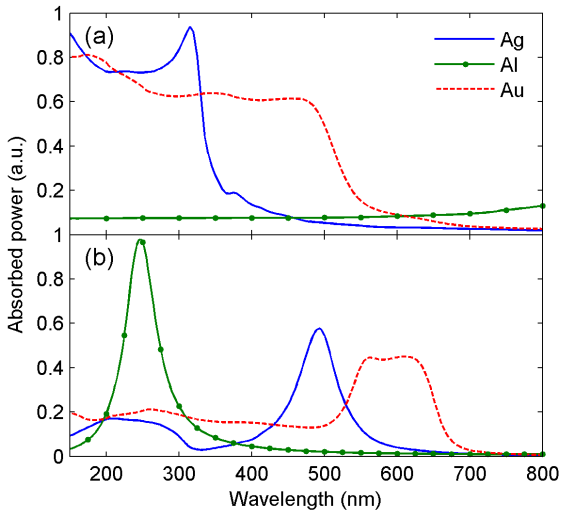

Figure 3.2: (a) Loss (normalized, arbitrary unit) in opaque metal films with different materials in air (calculated by 1-reflection). (b) Loss (normalized, arbitrary unit) in spherical NPs with different materials immersed in a material with refractive index 2+0.1i.

the same range as the maximum absorption enhancement due to the near-field enhancement as seen in Fig. 3.3. For Ag, LSP modes can be generated across the spectrum starting from around 350nm to the infrared range. The resonances are tunable by changing size, shape and the surrounding material of the particles. For other materials like gold the modes are always excited at wavelengths larger than 500nm. Therefore the concomitant loss in particles along with the LSP will also be in the visible range for Ag and Au, which causes light loss as heating, instead of exciton generation in organic materials. This heating loss can have significant negative influence in light harvesting in solar cells, if the particles have a large size and large volume density in/near organic materials. In addition, most metals, especially Ag and Au, will offer a large absorption (due to interband transition as discussed above for bulk metal) in the wavelength range below the resonance [41]. This could generate more heating loss in the particles. Al seems to work better in the ultraviolet (UV) range instead of for visible light, since the plasmonic modes tend to be excited in the UV range. In spite of this the long tail of the plasmonic mode towards larger wavelengths is beneficial for organic materials. In addition the loss in the Al particle will consequently be in the UV range, far away from the visible range where sunlight has much irradiance. Meanwhile there is no large loss in the visible due to interband transitions for Al. This offset can make Al also a good candidate for plasmonic applications

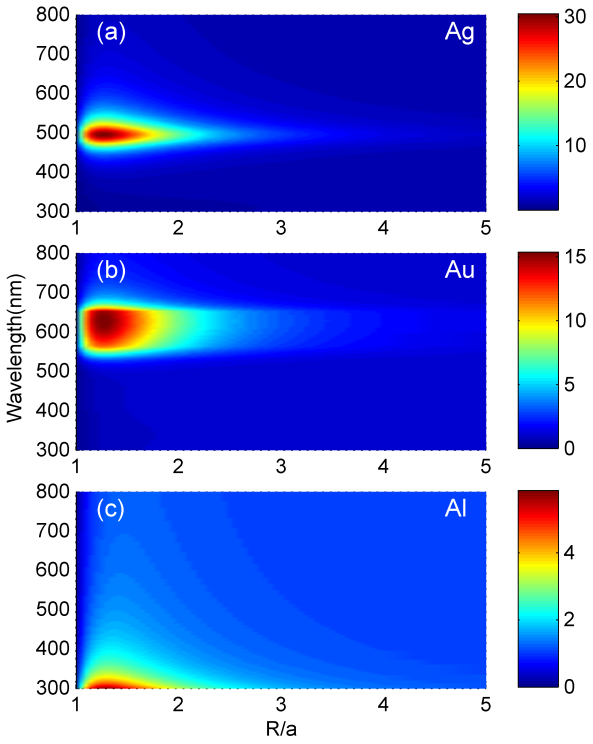

Figure 3.3: Absorption enhancement vs. wavelength and R/a, the ratio of radius of integral imaginary sphere and that of spherical Ag NP, for NPs with different materials.

(more investigations will be shown later).

Figure 3.4 shows the spectral absorption enhancement for Ag NP with a constant $R/a = 1.4$ for different radii. Clearly as shown in the figure, the absorption enhancement decreases quickly as the particle size increases. An enhancement factor around 30 is achieved for the smallest size. For larger particles higher order modes show up due to the considerable retardation. The scattering effect is more significant compared to near-field effect for large particles, which is related to the superposition of different order modes at the particle redistributes the field profile. As a consequence, for particles with 100nm radius the enhancement is very small. Meanwhile a red-shifted dipole resonance is observed out of the wavelength range for larger particles, which also further reduces the absorption enhancement.

The NP size and material control their plasmonic properties. The unique properties of Ag and Al make them considerably promising candidates for ap-

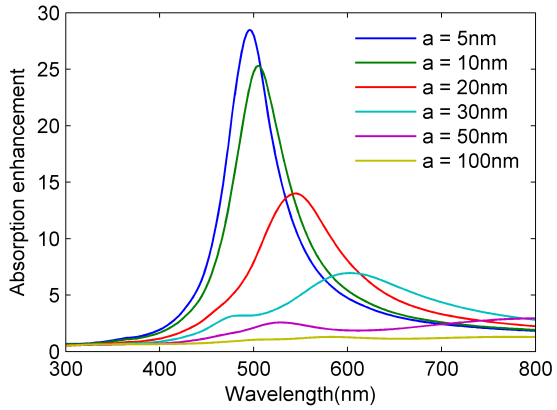

Figure 3.4: Spectral absorption enhancement for Ag NPs with different radii with R chosen to be 1.4a. The absorbing media has a refractive index $2+0.1i$.

plication in photovoltaics. For small particles the near-field effects can be exploited. For large particles the increased scattering effects could be used to diffuse the incident light into solar cells.

3.3 Nanowires

Based on the analytical studies in the previous section, here we exploit the near-field effects of Ag NPs to boost the light harvesting in OSCs. To start we consider nanowire arrays which can be described by a simple 2D model. 3D spherical particles will be considered in the next section.

3.3.1 Simulation setup

In the simulations, due to the indium scarcity, an ITO-free structure [42] was used as shown in Fig. 3.5. The Indium Tin Oxide (ITO) was replaced by a highly conductive polymer, PEDOT:PSS with 20 nm thickness, which is a polymer with good thermal and chemical stability and good flexibility. For the active layer the commonly used polymer, P3HT:PCBM with 1:1 weight ratio was used. The material of the cathode is aluminum and the MNPs are silver. The material properties of PEDOT:PSS, silver, aluminum and P3HT:PCBM are taken from literature [5, 40, 43]. For the silver MNPs the influence of the free path effect [6, 44] on the dielectric constant is taken into account. Figure 3.6 shows the refractive indices of the anode and the active material. For the active material the absorption is mainly between 300nm and 650nm.

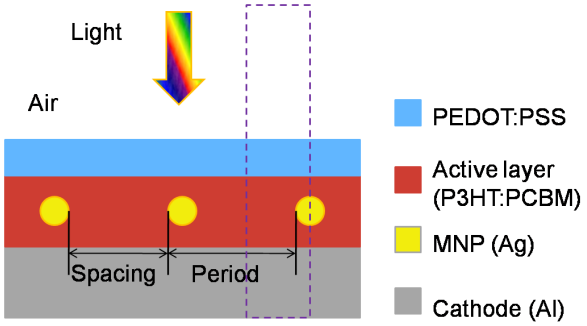

Figure 3.5: Schematic figure of the model of the solar cell with MNPs. In simulations only the dotted domain is used.

Here we use a 2D model, so the MNPs are a periodic array of cylindrical nanowires, which are embedded in the middle of the active layer in all simulations. Computations were performed using the commercial fully vectorial COMSOL software package. Here in order to excite LSPs in the nanowires, light with electric field normal to the nanowires is normally incident from the air into the solar cell (see Fig. 3.5), passing the PEDOT:PSS, the active layer and then reaching the cathode. Some light is absorbed in the anode, the active layer and the cathode, and the rest of it is reflected away from the solar cell.

Due to the periodicity and symmetry of the structure, by applying proper boundary conditions to the vertical boundaries, only part of the solar cell containing half of the MNPs and half of the space between the MNPs is used, as shown by the dotted domain in Fig. 3.5. By this setting, we can save computer memory and computational time yet still give accurate results. In simulations a mesh size of around 0.1 nm in the vicinity of the MNPs is employed. Computations have been performed using monochromatic excitations over the wavelength interval 300–800nm.

The absorption spectrum $\eta_A(\lambda)$ in each domain especially in active material and MNPs can be calculated from the volume integral of the time average of the divergence of the Poynting vector [45],

$$\eta_A(\lambda) = \int \nabla \cdot \langle \mathbf{S} \rangle \, dV = \frac{1}{2} \mathrm{Re} \int \nabla \cdot \left(\mathbf{E} \times \mathbf{H}^* \right) dV = \frac{1}{2} \int \epsilon'' \omega |\mathbf{E}|^2 dV, \tag{3.2}$$

where $\mathbf{E}$ is the electric field distribution in the integrated volume, the ω is the angular frequency, and ϵ'' is the imaginary part of the permittivity of the material in the integrated volume.

Since most of solar cells are usually characterized under AM 1.5G illumination condition, the whole absorption, η_A^{tot}, in active layer over 300-800nm is

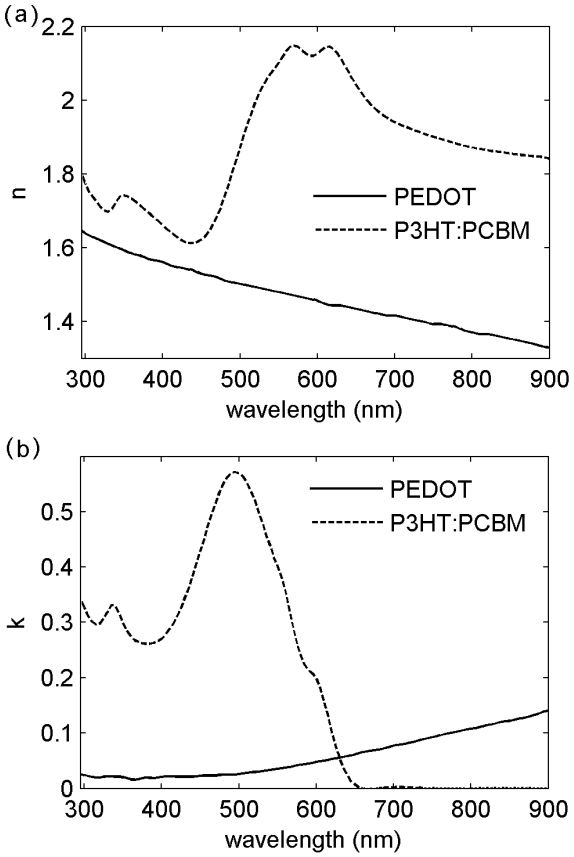

Figure 3.6: Real part (a) and imaginary part (b) of refractive indices of PEDOT and P3HT:PCBM(1:1).

calculated by means of integrating the absorption spectrum weighted by the AM 1.5G solar spectrum, $S(\lambda)$,

$$\eta_A^{tot} = \frac{\int \eta_A(\lambda) S(\lambda) d\lambda}{\int S(\lambda) d\lambda}. \tag{3.3}$$

Another important metric is the short circuit current density, J_{SC}. The J_{SC} achieves its maximum if we assume the internal quantum efficiency (η_{IQE}) of OSCs is 1, which means that all of the excitons are collected at electrodes and transferred into photocurrent. OSCs with (η_{IQE}) close to 100% have been demonstrated [46]. In this ideal case, the J_{SC} is given by:

$$J_{SC} = e \int \frac{\lambda}{hc} \eta_A(\lambda) S(\lambda) d\lambda. \tag{3.4}$$

where h is the Planck constant, c is the velocity of light in vacuum.

To evaluate the efficiency enhancement of OSCs by the MNPs we monitor two metrics, the absorption enhancement and the current density enhancement. The absorption enhancement F_A is a ratio of absorption in the active material with (w) MNPs to that without (wo) MNPs. The current density enhancement $F_{J_{SC}}$ is a ratio of current density with MNPs to that without MNPs.

$$F_A = \frac{\eta_A^{tot,w}}{\eta_A^{tot,wo}} \tag{3.5}$$

$$F_{J_{SC}} = \frac{J_{SC}^{w}}{J_{SC}^{wo}} \tag{3.6}$$

3.3.2 Active layer thickness

As a benchmark, we first study solar cells without MNPs and investigate the influence of the active layer thickness on the absorption. Theoretically, for a infinite thick planar OSC without MNPs in the wavelength range 300–800nm the maximum of the absorption in the active layer is around 68.73% under AM 1.5G illumination condition, given that no light is reflected back into free space and the loss in anode PEDOT:PSS is negligible. Since the active material P3HT:PCBM only absorbs light in the wavelength range from 300–650nm (as the absorption coefficient shows in Fig. 3.6). Figure 3.7 shows the absorption as a function of the active layer thickness. It can be seen that the absorption oscillates in function of thickness due to interference effects (Fabry-Perot (FP) resonances) for active layers thicker than 40nm. For thin active layers interference effects are negligible, therefore the absorption in the active layer increases linearly with the thickness. Maxima are observed at 61nm (50%), 196nm (59%) and 346nm (60%). From the inset of Fig. 3.7, it is clear that solar cells with 196nm active layer can absorb almost all of the incident light over 300–650nm.

Clearly, thick active layers can absorb most of the incident light. However, as the thickness increases, carrier recombination will become significant which reduces the internal quantum efficiency. Thin active layers have the advantages of material-savings and a high carrier collection efficiency, but at the cost of low light harvesting. However, for solar cells with thin active layers, the light harvesting can be increased by introducing MNPs into the structure. In this way by benefiting from the optical effects of MNPs, organic solar cells could combine the advantages of thin and thick active layers, namely high carrier collection efficiency and strong light harvesting, resulting in efficient cells.

In what follows, we investigate the influence of MNPs on absorption enhancement for a thin active layer with a thickness of 33nm. The absorption for this thickness is 30%, and the absorption spectrum is shown in the inset of

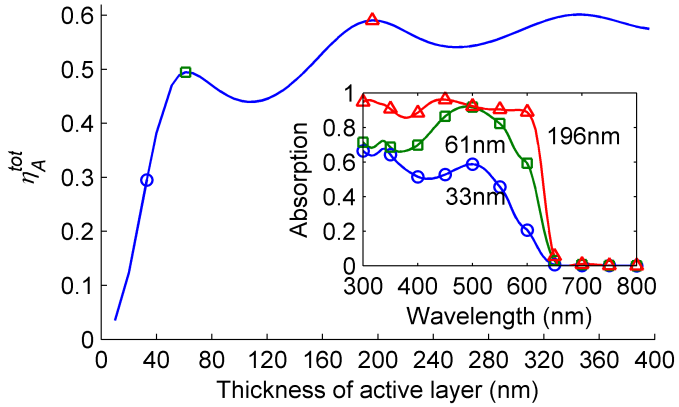

Figure 3.7: Thickness dependence of absorption in the active layer. The inset shows the absorption spectra for active layers with varying thicknesses.

Fig. 3.7.

3.3.3 Optimization

To optimize the structure with MNPs systematic studies have been carried out for various spacings (or periods) and MNP diameters. The absorption enhancement is mapped in Fig. 3.8 (a). Within a broad spacing and diameter an enhancement factor larger than 1.2 can be obtained, which means 20% more light is absorbed compared with the reference OSC without MNPs with an active layer thickness of 33nm. Absorption enhancement reaches its maximum, a factor of 1.56, with optimized parameter values: a diameter of 24nm and a spacing of 40nm. Considering the electrical property the current density enhancement is also mapped in Fig. 3.8 (b) given that the internal efficiency is as high as 1. The current density enhancement has a maximal value of 1.63 with the same optimized parameters as the optimal absorption enhancement. With the optimized parameters, the current density is enhanced from 6.7mA/cm^2 to 10.9mA/cm^2, whereas the absorption is from 30% to 47%.

Figure 3.9 shows the absorption spectrum and the spectral current density for the optimized solar cells with 24nm diameter MNPs and 40nm spacing. For comparison, we also plot the absorption spectra and the spectral current densities for solar cells without MNPs with thicknesses of 33nm and 61nm, respectively. We remark that the absorption spectrum of 33nm active layer with MNPs fits the spectrum of 61nm active layer without MNPs quite well. As a result the absorptions of these cells with (47%) and without (50%) MNPs are similar. Sim-

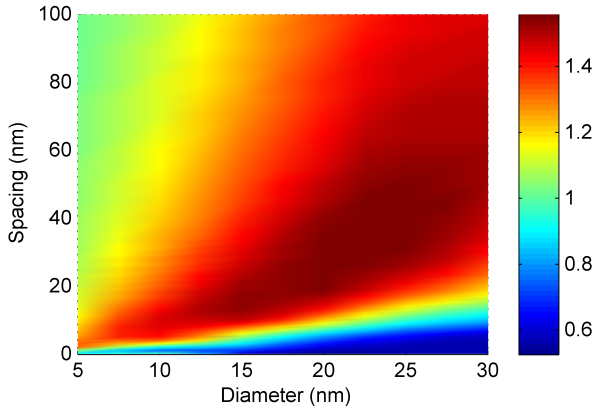

(a)

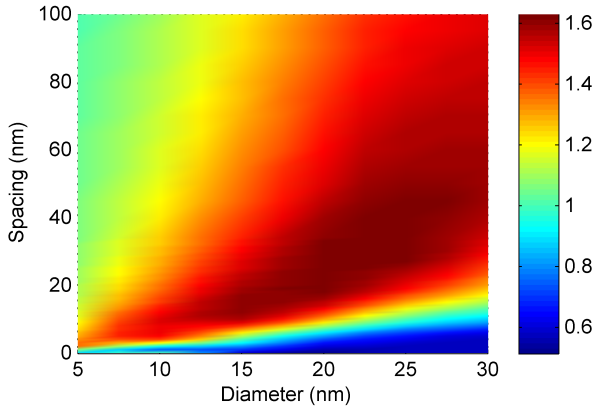

(b)

Figure 3.8: Map of absorption (F_A) (a) and current density ($F_{J_{SC}}$) (b) enhancements with MNPs in the middle of the active layer (33nm thickness) as a function of particle spacing and diameter. Both of them reach the maximum for MNP with diameter 24nm and a spacing of 40nm between MNPs. The absorption is enhanced from 30% to 47%, with an enhancement factor of 1.56. Whereas the current density is enhanced from 6.7 mA/cm^2 to 10.9 mA/cm^2 with an enhancement factor of 1.63.

ilar behavior can be observed for the spectral current densities in the same figure, which means that the optimized OSCs with MNPs and 33nm thick active layer have a similar current density to OSCs without MNPs, 10.9mA/cm^2 for the former vs. 11.6mA/cm^2 for the latter. In the following sections the spacing dependence and the enhancement mechanism will be discussed.

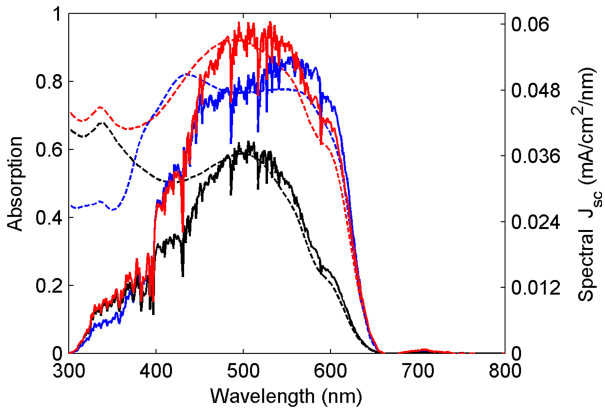

Figure 3.9: The optimized absorption spectrum (dashed) and spectral current density (solid). Both of them reach the maximum for MNP with diameter 24nm and a spacing of 40nm between MNPs. The blue curves (both dashed and solid) correspond to the optimized OSC with MNPs. The black and red curves correspond to the OSCs without MNPs with active layer thicknesses of 33nm and 61 nm respectively.

3.3.4 Particle spacing

In order to reveal the mechanism of absorption enhancement for a representative case the diameter of the MNPs is fixed at 10nm. The diameter influence is discussed in section 3.3.6. Figure 3.10 shows the absorption enhancement (together with current density enhancement) in the active layer in function of MNP spacing. The spacing is the distance between neighboring MNPs as defined in Fig. 3.5. The results of Fig. 3.10 are explained by examining the field profiles.

Figure 3.11 shows the average E field enhancement (E_e) and average mode area (A_m) which is calculated in the active layer (not taking the field inside MNPs into account) over the wavelength interval 300-800nm using a period of the periodic structure shown in Fig. 3.5,

$$E_e = \frac{\int\int\int \frac{|E_w|}{|E_{wo}|} dxdyd\lambda}{S\Delta\lambda} \tag{3.7}$$

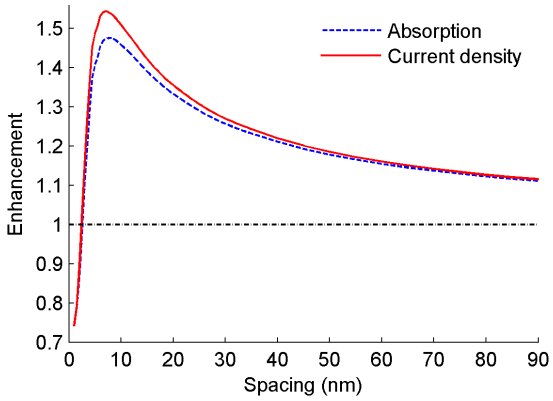

Figure 3.10: Absorption and current density enhancements (F_A and $F_{J_{SC}}$) with MNPs (10nm diameter) in active layer as a function of particle spacing.

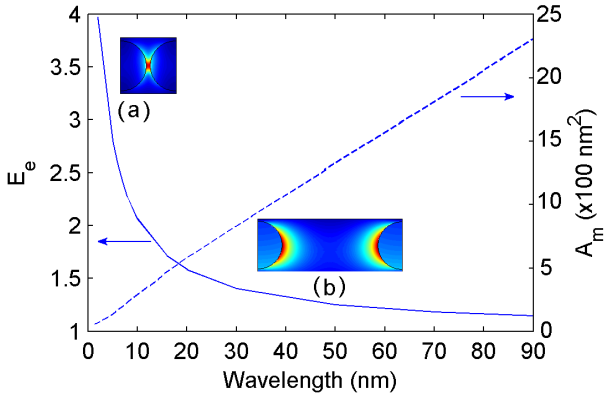

Figure 3.11: Spacing dependence of average E field enhancement (solid line, left y-axis) and average mode size (dashed line, right y-axis). The insets show the E field enhancement at 425 nm with different spacings: (a) 2 nm and (b) 20 nm.

$$A_m = \frac{1}{\Delta\lambda}\int \frac{\left(\int\int |E_w|^2 dxdy\right)^2}{\int\int |E_w|^4 dxdy} d\lambda \tag{3.8}$$

where E_w and E_{wo} are the electric fields with and without MNPs in the active layer, respectively. S denotes the area of active layer except that of MNPs. $\Delta\lambda$ is the wavelength interval and corresponds to 500nm (from 300nm to 800nm).

Figure 3.10 shows that there exists an optimum spacing of 8nm maximizing the absorption enhancement with a factor of around 1.48. This result is clarified by the graphs in Fig. 3.11. As the spacing increases, the electric field enhancement gets smaller and smaller. However, the field enhancement begins to spread out as the surface plasmon average mode area increases (also shown in Fig. 3.11). This is due to the decoupling between neighboring MNPs as illustrated by the insets in Fig. 3.11. When MNPs are far away from each other, the structure converges to the case with no MNPs, meaning that there is no absorption enhancement. As a consequence of these competing effects, there exists an optimum spacing.

3.3.5 Enhancement mechanism

In order to reveal which mechanism is more prominent, near-field enhancement or enhanced scattering, the active layer is divided into three sub-layers: front, middle and back sub-layers, as shown in the inset in Fig. 3.12(a). Figure 3.12(a) shows the absorption spectra. Figure 3.12(b)-(e) depict E field enhancement distributions (ratio of the |E| field with MNPs to that without MNPs) at representative wavelengths.

From Fig. 3.12 (a) one observes that the enhanced absorption is obvious only in the middle sub-layer where the MNPs are. The black dotted line has a broadband enhancement in the range between around 385nm and 650nm. For the other two sub-layers enhanced absorption is only observed in small wavelength ranges while in other ranges the absorption is decreased. These phenomena imply that the absorption enhancement is mainly attributed to near-field enhancement, and not to enhanced scattering effects, which is consistent with Mie results of section 3.2.

Figure 3.12(b)-(e) show the spatial distributions of the E field enhancement for dips and peaks in the black dotted line in (a), at 330nm, 425nm, 485nm and 565nm. At 330nm, due to the small $Re(\epsilon_{Ag})$ at short wavelengths, silver loses its metallic properties, and no dipole-like resonance exists at these short wavelengths. For 425nm, 485nm and 565nm, it is clear that the E field enhancement is mainly localized in the layer where the MNPs are. The maximum enhanced electric field exists in the vicinity of the MNPs in the space between MNPs. Therefore, this also shows that the mechanism of absorption enhancement is mainly due to the enhanced near-field, and not to scattering.

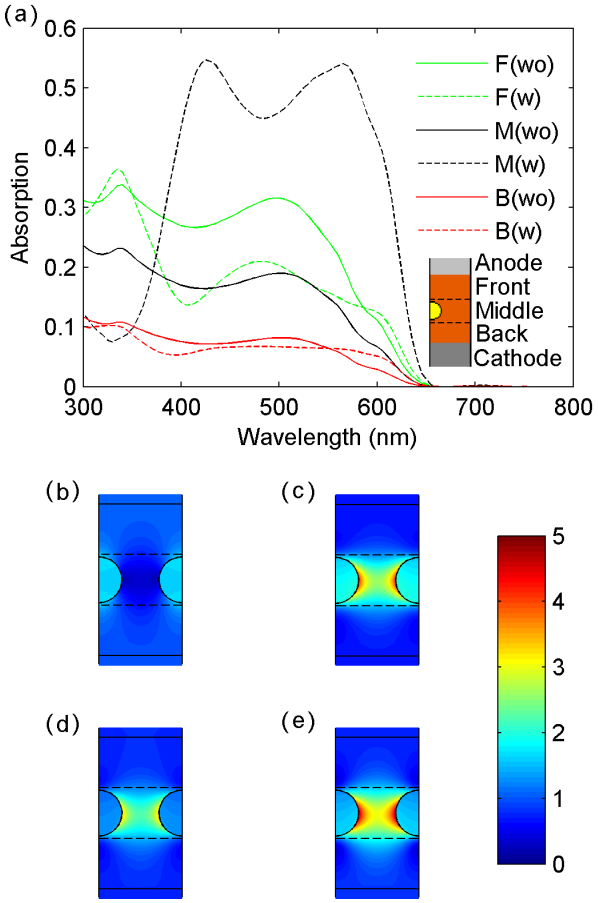

Figure 3.12: (a) Absorption spectra in front (f), middle (m) and back (b) layers with (w) and without (wo) MNPs embedded in the middle layer with 8 nm spacing. Representative figures of electric field enhancement corresponding to 8 nm spacing between MNPs at (b) 330 nm, (c) 425 nm, (d) 485 nm, and (e) 565 nm.

From Fig. 3.12(a) it is also seen that each of the absorption spectra without MNPs (solid lines) has a peak around 485nm (also shown in the inset to Fig. 3.7). This is because, as visible in Fig. 3.6(b), the imaginary part of the P3HT:PCBM index has a peak around 485nm, which corresponds to a strong absorption at this wavelength. However, when there are MNPs present in the active layer, the absorption at 485nm decreases, and two peaks appear around 425nm and 565nm. This can be explained as follows.

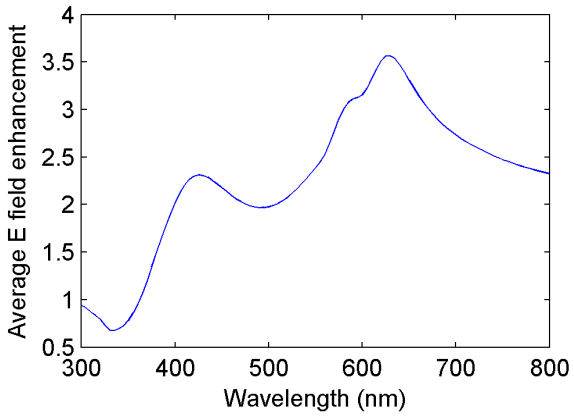

Figure 3.13: Spectrum of the average E field enhancement for 8 nm spacing between MNPs (when integrated over the middle sublayer excluding the MNP area).

For a single cylinder nanowire, the resonance position is at 370nm which is determined by the quasi-static resonance condition: $Re(\epsilon_{Ag}) = -Re(\epsilon_{P3HT:PCBM})$ (when imaginary parts are small, see in section 2.5). As shown in Fig. 3.13, which shows an enhancement spectrum, the peak at 425nm is the red-shifted resonance position due to the coupling between neighboring MNPs. This red-shifted resonance position determines the absorption peak of the MNP spectra in Fig. 3.12 (a).

Furthermore, it was shown that embedding particles in an absorptive material will suppress the near-field intensity enhancement, as less light will reach the particle [6]. The absorption of the active material is large at 485nm. Therefore, the E field enhancement is lower at 485nm than at other wavelengths when introducing MNPs into the active layer (see Fig. 3.13). As a result, the absorption enhancement is also lower there. From 490nm to 630nm, as shown in Fig. 3.13, the E field enhancement gets larger. However, for the active material P3HT:PCBM, as shown in Fig. 3.6(b), the absorption drops in this range. As a consequence, the absorption has another peak around 565nm.

3.3.6 Particle diameter and coating

The dependence of absorption enhancement on the diameter of MNPs has been investigated, as shown by the blue solid lines in Fig. 3.14. The optimum diameter is 24nm with an absorption enhancement around 1.56 for 40nm spacing. With this diameter and spacing, the solar cell can absorb 47%, which is close to one of the maxima in Fig. 3.7: There we obtained 50% with a 61nm active layer without MNPs.

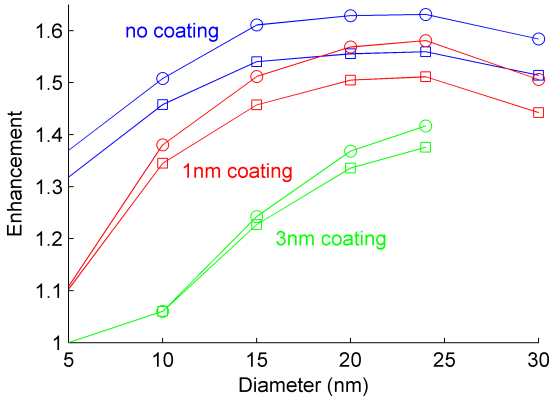

Figure 3.14: Optimized absorption enhancement F_A (square marker) and current density enhancement $F_{J_{SC}}$ (circle marker) as a function of MNP diameter with and without coating.

In Fig. 3.14 the influence of coating on absorption enhancement is also depicted. In previous simulations the MNPs were in direct contact with the active layer, therefore the generated excitons can be quenched at the MNPs. In order to avoid this a coating over the MNPs is required. In our numerics silica (n = 1.46) is used to coat the MNPs with different thicknesses, see Fig.8(a). We notice clearly that a thicker coating decreases the absorption enhancement. For MNPs with 5nm diameter, no enhancement can be observed any more with a 3nm coating. The coating should be thin compared with the MNP diameter in order to obtain the absorption enhancement.

Note that in [47] it is reported that using a coating material with large refractive index can give extra enhancement. The mechanism behind this is that the electric field tends to localize/confine in a material with a lower refractive index right next to the higher index material. Therefore using a material with higher refractive index than the organic material can push more electric field into the organic material yielding high intensity in the vicinity of coated MNPs. However the LSP resonance peak will red-shift due to the increased surrounding effective

index. On this ground extra engineering should be performed to optimize the thickness and the material of the coating layer.

3.4 Nano-spheres

The previous OSC structure is sensitive to the light polarization, since only the TM polarized light can excite the LSP in metallic nanowires. For TE polarization the MNP works as an absorber and will reduce light harvesting in the active layer. Therefore the overall enhancement will be an average value of enhancements under these two polarizations. Here in this section periodic spherical MNPs with square lattice embedded in solar cells will be investigated, which is not very sensitive to the polarization under small incident angle. There are lots of reported simulations and experiments on the utilization of Ag and Au nanostructures for light trapping in OSCs. Recently an increasing number of studies with Al have been carried out. Compared to Ag and Au, Al is more cost-effective and also exhibits attractive plasmonic properties as discussed in section 3.2. Herein we will demonstrate these different materials from optical simulation aspects.

3.4.1 Embedded in the active layer

The structure of OSC investigated here is more concrete, including an ITO coated glass substrate as illustrated in Fig. 3.15. The reflector is chosen to be Ag. To have good internal quantum efficiency the P3HT:PCBM is determined to be 40nm thick. Thicknesses of PEDOT:PSS and ITO layers are 20nm and 100nm respectively. MNPs are embedded in the middle of the active layer. The glass substrate is taken as semi-infinite with light illuminating the structure from glass.

Due to the polarization independence of the structure for normal incidence (in that an array of MNPs in a square lattice is used) only one polarization along x-axis is considered. For unpolarized sunlight the absorption will be the same as the polarized one since sunlight can be decomposed as two orthogonal polarizations. Similar to the previous simulations, to save computational memory and time, only quarter of one unit cell (one period) is modeled due to symmetry and periodicity of the structure. All the optical constants of P3HT:PCBM, PEDOT:PSS and ITO used in simulations are measured by D. Cheyns at imec using a SOPRA GESP-5 spectroscopic ellipsometer and are shown in Fig. 3.15(b).

Figure 3.16 shows the current density enhancement versus the diameter and the ratio of spacing to diameter for Ag, Al and Au NPs. To have an intuitive comparison these three enhancement maps utilize the same enhancement factor color scale with a maximum value of 1.5. Ag and Al have a comparable maximal

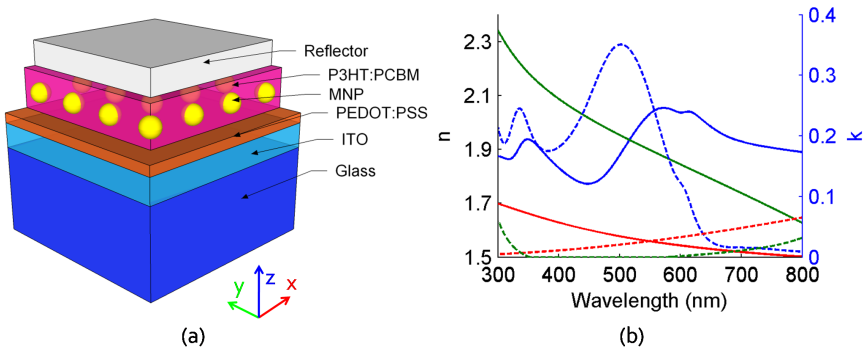

Figure 3.15: (a) Schematic of OSCs with spherical Ag NPs array with square lattice in active layer. (b) Refractive index of different materials. Solid: n. Dash: k. Blue: P3HT:PCBM. Red: PEDOT:PSS. Green: ITO.

enhancement factor, 1.46 for Ag and 1.49 for Al, whereas we obtain only 1.09 for Au. The current density has been boosted from 7.3mA/cm^2 for reference structure with no MNPs to 10.7mA/cm^2 for OSCs with Ag NPs, 10.9mA/cm^2 with Al NPs and 7.9mA/cm^2 with Au NPs. Note that the map of current density enhancement is very similar to the nanowire case as shown in Fig. 3.8(b) previously. For a certain diameter the current density enhancement achieves its maximum at a ratio of spacing to diameter close to one. For smaller spacing the interaction between particles is significant resulting in very localized near-fields in the small range between particles, similar to the nanowire case (section 3.3.4), making the enhancement small. For large spacing the enhancement decreases due to the near-field effects becoming negligible compared to the large domain of active material. The intermediate spacing provides an appropriate plasmonic mode volume to reach the enhancement maximum.

Figure 3.17 shows the optimized absorption spectra and spectral current density of OSCs with MNPs together with that of the reference structure (without particles). Enhanced absorption is only observed above a certain wavelength. Au has the smallest enhanced range, while Al has the largest range and Ag is in between. This is due to enhanced near-field along with the LSP excitation and the concomitant loss in MNPs. The near-field tends to enhance the light harvesting above the resonance because its long tail tends to longer wavelengths instead of towards shorter wavelengths [1]. For Au and Ag the resonance is located in the visible range (> 460nm for Ag and > 550nm for Au, the resonance will red-shift due to the coupling between the particles), whereas the Al one is located in UV. The reduction for Al at short wavelengths is due to the red-

[1] This is because the magnitude of the real part of the epsilon of metal increases with wavelength as shown in Fig. 3.1.

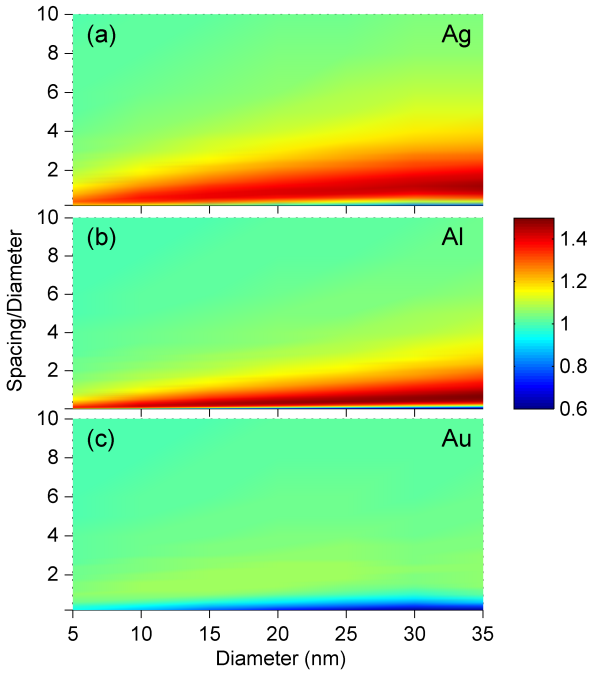

Figure 3.16: Map of current density enhancements $F_{J_{SC}}$ with spherical MNPs, (a) Ag, (b) Al, (c) Au, in the middle of active layer (40nm thickness) vs. diameter and spacing/diameter. For the optimized case, the current density is boosted from 7.3 mA/cm^2 to 10.7 mA/cm^2, 10.9 mA/cm^2, and 7.9 mA/cm^2 with enhancement factors of $\sim$ 1.46, $\sim$ 1.49, and $\sim$ 1.09 for Ag, Al and Au respectively. The optimized parameters (diameter, spacing) are (35nm, 42nm) for Ag, (35nm, 21nm) for Ag and (20nm, 36nm) for Au.

shift resonance (around 350nm) and loss in Al particles. For Au and Ag the loss caused by interband transitions at short wavelengths also plays an important role. Furthermore we note that the reductions in absorption for short wavelengths are significant, however the reduction in spectral current density is negligible. This is due to the solar spectrum which has smaller irradiance at short wavelengths.

So far it is clear that Al and Ag are the more suitable materials for exploiting the near-field effects for light harvesting. From our simulations the Al particles seem a little bit superior to Ag considering the current density enhancement and the material cost. As for Au its loss at short wavelengths and red-shifted LSP resonance make it not a promising choice.

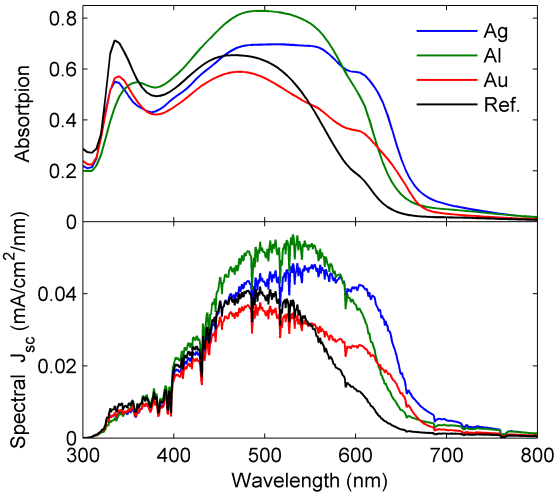

Figure 3.17: Absorption spectra (a) and spectral current densities (b) for OSCs with and without MNPs. The total absorption is boosted from 32% to 44%, 46% and 33% with enhancement factor of ~1.37, ~1.42 and ~1.03 for Ag, Al and Au respectively.

3.4.2 Embedded in the buffer layer

In various reported experiments the particles are not inside the active layer, they are most often integrated immediately next to it, usually the PEDOT:PSS buffer layer [11–14]. The size of the particles always falls in the range of 10nm, as well as the spacing. In this way, the near-field possibly can couple into the active layer. To verify here we simulate an OSC with MNPs inside the buffer layer PEDOT:PSS instead of in the active layer as shown in Fig. 3.15(a). We keep the thicknesses of layers the same as in Fig. 3.15(a). For comparison gold is used for the particles in place of silver since it is always used in experiments. Fig 3.18 shows the current density enhancement for different Au particle sizes and spacings. It is clear that there is no current density enhancement no matter how large the particles and the spacing are. Our extensive simulations for Ag and Al spherical particles also show no enhancement.

Figure 3.19 (a) and (b) show the absorption difference in the active layer (P3HT:PCBM) and buffer layer (PEDOT:PSS) between the situation with and without particles (with 10nm diameter) in the PEDOT:PSS for some selected spacings. We see a positive absorption difference for the PEDOT:PSS layer, which means more light is absorbed in the PEDOT:PSS as heating loss. Meanwhile there is no enhanced light harvesting in the active layer but reduction due to more light absorbed in anode and MNPs (as shown in (c)). The enhanced

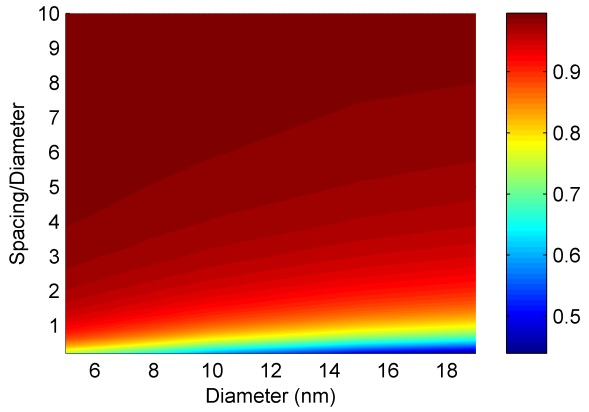

Figure 3.18: Current density enhancement $F_{J_{SC}}$ map with spherical MNPs in the middle of buffer layer (PEDOT:PSS) versus particle spacing and spacing/diameter. The buffer layer is 20nm thick.

absorption in PEDOT:PSS and reduction in the active layer is attributed to the near-field effects located mostly in the lateral direction of MNPs.

Our calculations show that this configuration does not provide (current density or absorption) enhancement for small particles (size smaller than 20nm). Our simulated structures are only slightly different from those in reported experiments, especially concerning the thickness of the active layer. The field distribution in the solar cell will be tuned by the thickness. However no matter how the thickness and the field distribution is, scattering of particles is negligible (for such small particles), and the near-field enhancement is mainly localized in the lateral direction, decaying rapidly in the buffer layer and maybe partly into the active layer. An effective decay distance is roughly 0.26 times the radius of the particle [22]. For thinner active layers, this may still be useful, especially when the particles can couple to a metallic back-contact on the other side of the active layer [48–50]. The coupling with the reflector may be stronger when a nanodisk (cylinder) is used for the particles instead of a spheroid. The near-field tends to localize at the nanodisk corners, instead of sideways as for a spheroid. Therefore the near-field would be more easily coupled to the active layer, and well coupled with the reflector for a thin enough active layer. However the nanodisk has to be larger than 20nm laterally in size and have large spacing (comparable to wavelength in surrounding material) to have efficient coupling with the reflector (see next chapter).

In calculating the current density enhancement a 100% internal quantum efficiency is assumed, which is not the case in reality. This leaves some room for improvement by the particles. Therefore the observed efficiency improvement

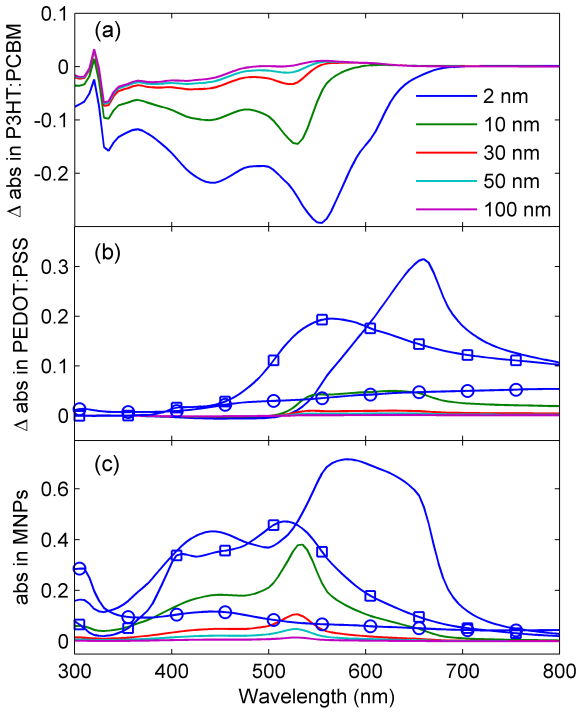

Figure 3.19: Absorption difference in P3HT:PCBM (a) and PEDOT:PSS (b) between with and without Au particles in buffer layer for different spacing. (c) Absorption spectra in Au particles. The Au particles have 10nm radius. As comparison in (b) and (c) curves for Ag (square marker) and Al (circle marker) are also plotted for 2nm spacing. Low loss in Al is observed because of the LSP excited at UV. But enhanced absorption in PEDOT:PSS is still observed for Al particles.

in reported experiments with particles (both Ag and Au) in the buffer layer PEDOT:PSS may be due to improved electronic effects [11, 51] like decreased resistance, improved exciton dissociation [52, 53] or carrier collection.

3.5 Experimental observations of enhanced absorption

3.5.1 Experiments

In order to have a better understanding of how the MNPs contribute to absorption enhancement in active materials, experiments were carried out by col-

leagues B. Niesen *et al.* at imec [54]. They prepared samples with silver and organic small molecule materials, CuPc or SubPc. First a layer of Ag (99.99% purity, Kurt. J. Lesker Company) was deposited at 0.01 nm/s to a thickness of 1 nm on glass substrate, as determined by the quartz-crystal oscillator. As a result, it yields Ag MNPs with a (top view) circular shape, and an average particle diameter of 7 nm and an inter-particle spacing comparable to the particle size as the scanning electron micrograph shows in Fig. 3.20(a). From atomic force microscopy measurements in Fig. 3.20(b), an average NP height of 5 nm was determined. Then organic materials, CuPc or SubPc, were deposited at a rate of 0.1nm/s on top of the Ag MNPs with different thicknesses. As comparison CuPc or SubPc directly on top of glass were also fabricated with the same thicknesses. Samples containing Ag MNPs covered by organic materials and pure organic materials were obtained from samples that were coated in the same deposition run to ensure a minimal thickness variation.

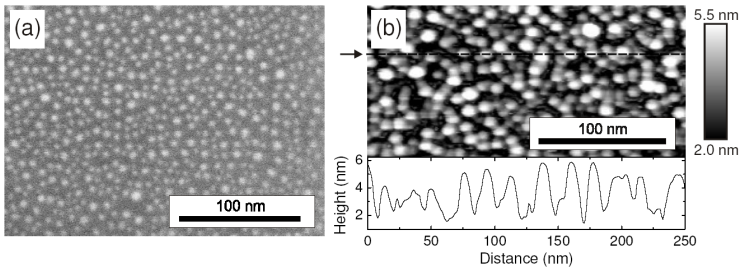

Figure 3.20: SEM (a) and AFM (b) images of Ag MNPs on glass substrate by thermal evaporation. In (b) there is a height-profile (bottom) taken along the dashed line indicated by the arrow. The lateral size of the NPs is overestimated due to convolution of the atomic force microscope tip and the sample features.

Samples were measured by imec using a Bentham PVE 300 photovoltaic device characterization system to determine the reflection and transmission from these samples. The direct light transmission was measured using a Shimadzu UV-1601PC spectrophotometer. The light absorption was defined as absorption = 1 - direct transmission - reflectance. The absorption of the glass substrate was subtracted from all absorption spectra.

3.5.2 Simulation setup

We performed numerical simulations by means of FEM to have a basic understanding of the effects by the deposited Ag MNPs on absorption in organic materials. In our simulations the samples are modeled as a sandwich structure

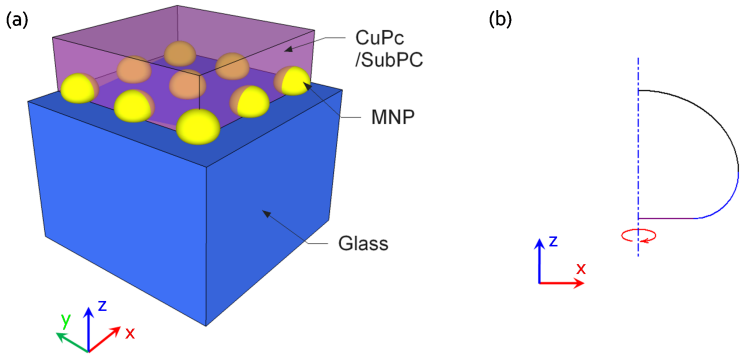

Figure 3.21: (a) Geometry under investigations for MNPs covered with CuPc or SubPc. A square lattice is used for Ag MNPs. The light is incident normally from semi-infinite glass substrate, with E field along x-axis. (b) the profile of a truncated MNP, 5nm high and 7nm wide, consisting of sections of quarter of an ellipse, quarter of a circle and a straight line.

between two semi-infinite spaces, the glass substrate and the air surrounding. It extends infinitely in xy-plane. The arrangement of Ag MNPs on glass was assumed to be a square lattice with a center to center spacing between MNPs of 14nm (illustrated in Fig. 3.21). The geometry of a single MNP has a height of 5nm and a width of 7nm, as the cross section shows in Fig. 3.21. The MNPs are covered with the organic materials with different thicknesses, followed by a semi-infinite air surrounding. As reference situation structures with no Ag MNPs with the same thickness of organic materials were simulated. The dielectric constants of CuPc and SubPc used in the simulations were measured at imec and shown in Fig. 3.22.

Similar as in experiments, the light is incident normally through the semi-infinite glass substrate (n = 1.5), namely with the wavevector k parallel to the z-axis. Due to the polarization independence of the structure under normal incidence, we only consider the polarization with electric field E parallel to the x-axis. The light absorption in the Ag and in organic materials was monitored directly and separately.

Note that this model is an idealized model, since in reality the MNPs do not possess the lattice arrangement, constant spacing, and single size and shape. All of these parameters are quite dispersive. Meanwhile simulation models extend infinitely in 3D, especially in xy-plane. However samples have a finite area. In spite of using a well-arranged model, it still gives quite good predictions as we will see in the following.

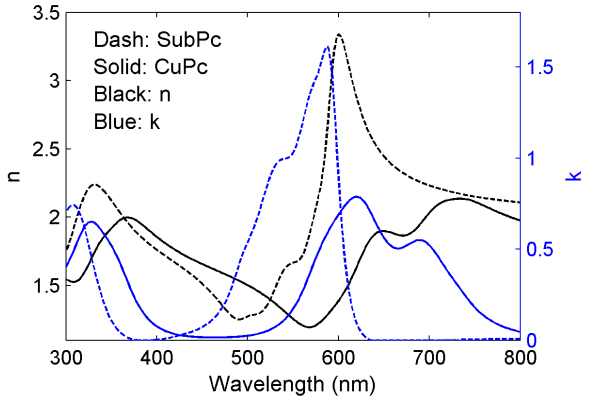

Figure 3.22: Dielectric constants (n and k) of CuPc and SubPc. Black lines for the n, blue for the k. Solids are the dielectric constants of CuPc, dashes for SubPc.

3.5.3 Results

CuPc

To monitor the influence of MNPs on absorption in CuPc, the absorption difference Δabs between samples with MNPs and without MNPs are investigated. In experiments the absorption difference Δabs includes the absorption in Ag MNPs since it is impossible to separate it. However in simulations this can be done.

Figure 3.23(a) shows Δabs from experiments and simulations. The solid lines show the simulated absorption difference with and without silver NPs in CuPc, including the loss in the silver NPs to correspond with measurements. We find that the measured and simulated results have similar curve profiles. For example, the main peaks are all showing up around 470nm in both simulations and experiments. These peaks correspond to the LSP resonance in small Ag MNPs, which can be verified by monitoring the absorption in Ag MNPs as shown in Fig. 3.23(b). Since the particle sizes are much smaller than the wavelength the peak position is directly determined by material properties, given by the quasi-static approximation of Eq. 5.7 if one neglects the limited substrate effects. However, the peaks in simulations are narrower than the measured ones. This could be due to:

1. The MNPs in simulations are periodically distributed, but in experiment they are random;

2. The MNPs in simulations have the same size and shape, but in experiment

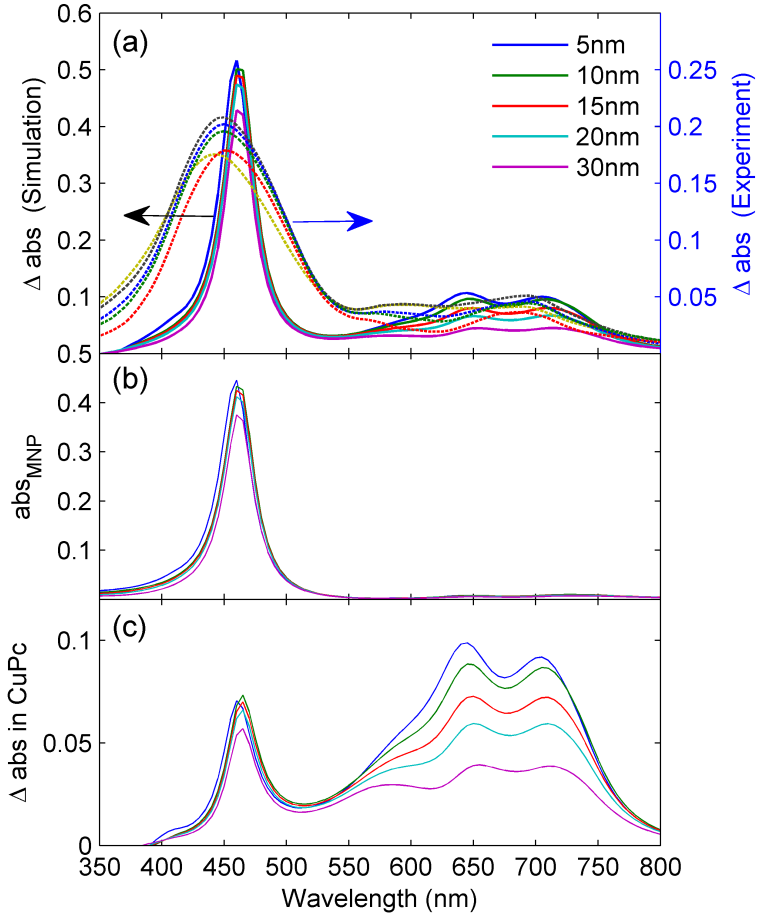

Figure 3.23: (a) Absorption difference between samples with and without Ag MNPs for different thicknesses of CuPc. Absorption in Ag MNPs is included. Solids: simulations. Dashes: experiments. (b) Absorption in Ag MNPs for different thicknesses of CuPc from simulations. The absorption peak corresponds to the LSP resonance in Ag MNPs. (c) Simulated absorption difference in CuPc between samples with and without Ag MNPs for different thicknesses of CuPc.

they have different sizes and shapes;

3. Slight influences might come from the infinite array in simulations compared with the finite sample area, and the absence of the glass-air interface on the incident side in simulations.

All of these aspects could broaden the resonance. As known the size, shape and spacing between particles can influence the LSP resonance. However the particle size and shape of the sample will not vary a lot and the size is already quite small. Therefore among these aspects above distribution may be the most significant.

From Fig. 3.23(b) note that the absorption in Ag MNPs in the wavelength range 550nm–800nm is quite negligible. This implies the absorption difference in Fig. 3.23(a) in corresponding wavelength range is mostly attributed to CuPc in both experiments and simulations. Figure 3.23(c) shows the simulated absorption difference in CuPc excluding the absorption in Ag MNPs. Enhanced absorption can be observed for a broad wavelength range. The enhancement for different thicknesses is quite constant in the vicinity of the resonance, which is caused by the near-field enhancement around MNPs. However in the wavelength range larger than 550nm, the enhancement reduces quickly as the thickness increases. This can be understood because for a thicker organic layer, less material benefits from the near-field enhancement around MNPs.

SubPc

Figure 3.24 shows the results from simulations and experiments. Although again absorption difference results from simulations are overestimated (Fig. 3.24 (a)), they still have similar shapes. The two absorption peaks are well predicted by simulations. These two peaks are two dipole LSP resonances (as verified by absorption in MNPs in Fig. 3.24(b)) in MNPs because the quite dispersive optical refractive index of SubPc as shown in Fig. 3.22 (black dashed curve) results in two wavelengths that satisfy the quasi-static approximation for LSP dipole resonance condition of Eq. 5.7. The broadened peaks should be due to the same reasons as listed previously. The absorption enhancement in SubPc (as shown in Fig. 3.24(a) and (c)) between these two peaks could be directly due to the near-field enhancement, since the loss in Ag MNPs is quite small as shown in Fig. 3.24(b).

Therefore as illustrated above by both simulations and experiments for two different organic materials, Ag MNPs can enhance the absorption in the surrounded organic materials. The absorption enhancement is attributed to the near-field enhancement from the dipole resonance in MNPs. Meanwhile the enhancement is not just limited to the resonance, but extends over larger wavelength range.

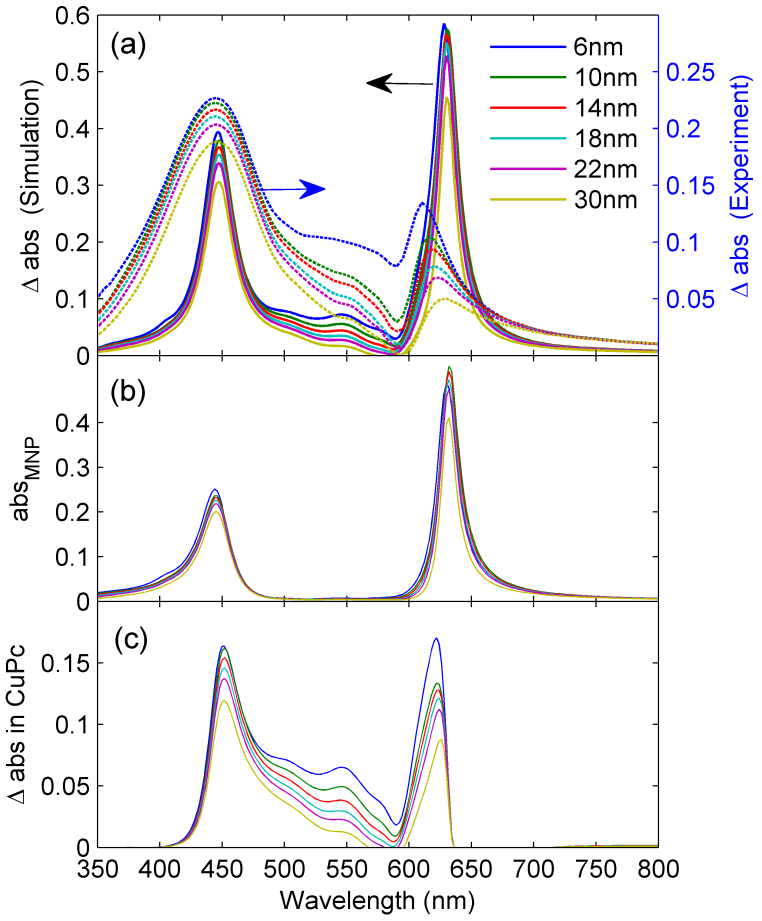

Figure 3.24: (a) Absorption difference between sample with and without Ag MNPs for different thickness of SubPc. Absorption in Ag MNPs is included. Solids: simulations. Dashes: experiments. (b) Absorption in Ag MNPs for different thickness of SubPc from simulations. The absorption peaks correspond to two LSP dipole resonances in Ag MNPs located at different wavelength. (c)Simulated absorption difference in SubPc between sample with and without Ag MNPs for different thickness of SubPc.

3.6 Large particles as scatterers

As shown in Fig. 3.4 the benefit for the absorbing medium from near-field effects around large particles is negligible. However it is possible to have the far-field benefit of large particles, which is enhanced scattering. To exploit scattering it is not ideal to embed large particles directly in organic active materials, since the exciton diffusion length in organic materials is on the order of 10nm which is small compared to the particle size. MNPs as scattering elements in Si thin-film solar cells have been demonstrated, and usually the particles are placed on top of the solar cells [23, 25–37]. Here we present a feasibility study on MNPs as scatterers on top of OSCs. Figure 3.25 shows the structure under investigation.

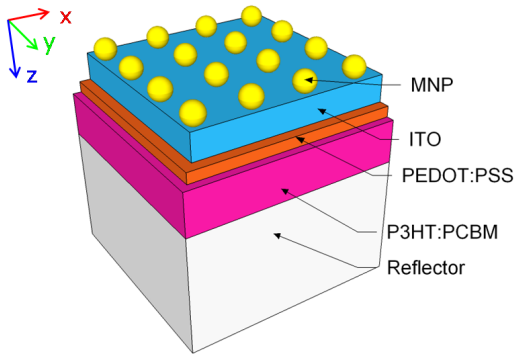

Figure 3.25: Schematic diagram of Ag NP array as scatterers on top of ITO. Light illuminates from the particle side.

To elucidate the basic principle behind MNPs as scatterers, we first examine the properties of a single spherical Ag NP using Mie theory. In chapter 2 we have already commented on this, here we provide a more detailed discussion on scattering. Figure 3.26 shows the scattering and absorption efficiencies for a Ag NPs with different diameters in an air surrounding. One sees that scattering becomes more significant than absorption for larger particles, in addition a quadrupole mode is introduced. Notice that the absorption induced by the dipole mode is smaller than that by the quadrupole. Moreover as the particle size increases the absorption and scattering are separated spectrally, yielding a broadband enhancement scattering over the range where solar irradiance is large. For instance the absorption and scattering are in the same wavelength band for particle diameter 60nm, and the absorption is larger than scattering. Consequently for small particles they will work as absorbers rather than efficient scatterers in the configuration in Fig. 3.25. Therefore these results suggest

that efficient scatterers have to be of large size.

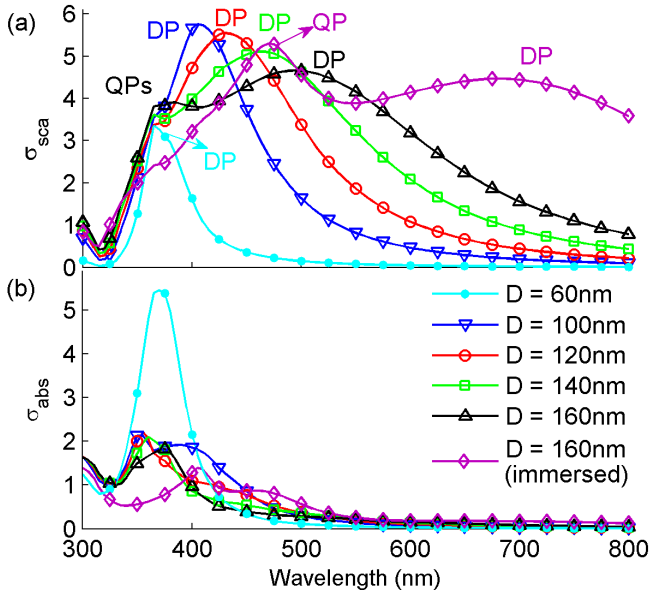

Figure 3.26: (a) Scattering efficiency σ_{sca} and (b) absorption efficiency σ_{abs} versus wavelength for a single Ag NP with different diameters (D). The diamond marked purple line corresponds to the particle immersed in a medium with refractive index 1.41, while others are in air. DP: dipole mode. QP: quadrupole mode.

Now we examine the scenario depicted in Fig. 3.25. Here the thickness of the active layer P3HT:PCBM is fixed at 100nm, for the buffer layer PEDOT:PSS 20nm, and for the ITO anode 100nm. The reflector is in Ag. The Ag NP array with square lattice is directly on top of the ITO. The reference structure is a planar without particle array on top, which gives a total absorption of 44.7% in the wavelength range 300–800nm and a current density of 10.9mA/cm^2. Light is normally incident from the particle side, along the z-axis. We only consider polarization with electric field parallel to the x-axis. The figures of merit are the absorption and current density enhancement defined in Eqs. 3.5 and 3.6. To optimize the enhancement we investigate the particle diameter and the period (the lattice constant) of the array.

Figure 3.27 shows the period dependence of absorption and current density enhancements for different diameters. Note that the maximum enhancements increase with particle diameter, in the range investigated here. This is because the scattering by an individual particle increases with diameter, as discussed

previously. For small periods, indicating a high particle density, the total absorption by the particles due to the plasmonic resonance will be stronger. On the other hand, for large periods, with low particle density, forward scattering effects will decrease. Consequently there is an optimal period for different particle sizes. In the investigated parameter range (four different diameters and periods, respectively) we found as maximum absorption and current density enhancement factors 1.094 and 1.092, respectively, with a diameter of 160nm, and corresponding periods 400nm and 440nm. Slightly higher values may be achievable according to the fitting lines.

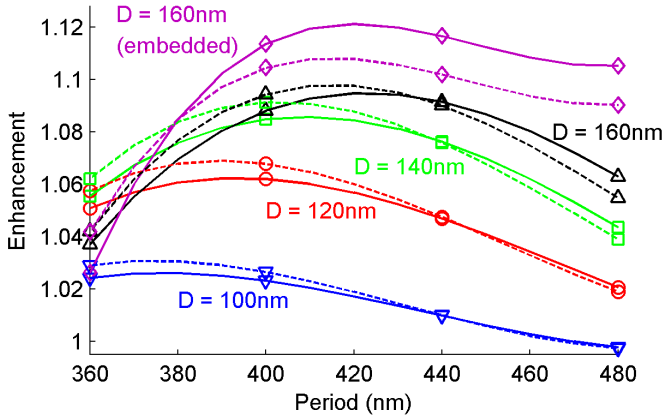

Figure 3.27: Absorption (F_A) and current density ($F_{J_{SC}}$) enhancements versus array period for different NP diameters. The markers are the simulated data points. Solid lines: fitted current density enhancement, dashed lines: fitted absorption enhancement. The purple lines are for the arrays embedded in a medium with refractive index 1.41 (diameter 160nm). The reference structure has an absorption of 44.7% and a current density of 10.9mA/cm^2.

As shown in Fig. 3.26 for the 160nm diameter NP the scattering peak is located around 500nm, with scattering at larger wavelengths 600–800nm relatively non-efficient. To increase the scattering efficiency at larger wavelengths one can enlarge the particle size or change the surrounding medium. Here we consider the latter one by immersing the particle in another medium. From the diamond marked purple curve in Fig. 3.26 we can see that the scattering efficiency is improved dramatically by immersing the particle in the medium with refractive index 1.41.

Now for the OSC case (Fig. 3.25) we fill the space between particles with the higher refractive index medium. The filling layer has a thickness identical to the particle diameter. Above this Ag NP layer is the air surrounding. We give an

example for the particle array with 160nm diameter. The diamond marked purple solid curve in Fig. 3.27 shows the calculated current density enhancements for this case, note that the current density enhancement is improved to around 1.12.

Figure 3.28 shows the spectra for the NP array with 160nm diameter in air and in a medium together with the absorption spectrum for the reference structure. Due to the strong forward scattering by the NP array the absorption in the range 410–600nm is enhanced. A typical field distribution for the case with NP array embedded in a medium at this wavelength range is plotted in Fig. 3.29(a). We can see there is a maximum electric field in the active layer. From the spectrum it is seen that the embedded array offers a broader enhanced absorption range due to more efficient scattering. Meanwhile at a larger wavelength (around 690nm) there are peaks for both cases. Field distributions are plotted in Fig. 3.29(b) and (c) for the embedded case. Examining the magnetic field (b) a SPP character is observed with field confined to the surface of reflector. Meanwhile a guided mode profile in the whole structure is also observable when looking at plot (c). Therefore this peak arises from the mixed photonic mode due to the scattering of light by the NP array.

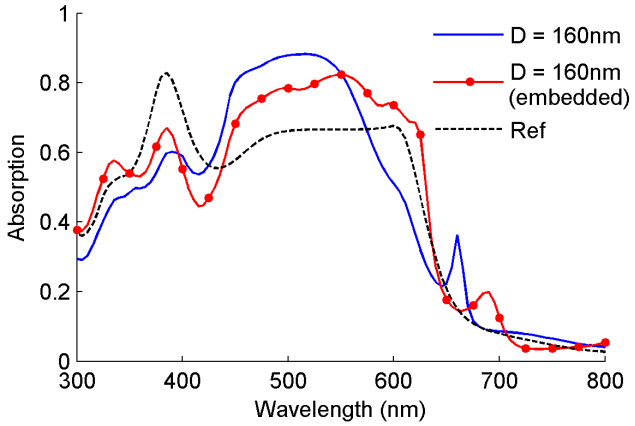

Figure 3.28: Absorption spectra for Ag NP array in air (solid curve) and in a medium (n = 1.41) (dot marked curve) with period 440nm. The dashed curve is for the planar reference without particle array.

3.7 Conclusion

In conclusion, in this chapter we have studied systematically the effects of MNPs on light harvesting in OSCs.

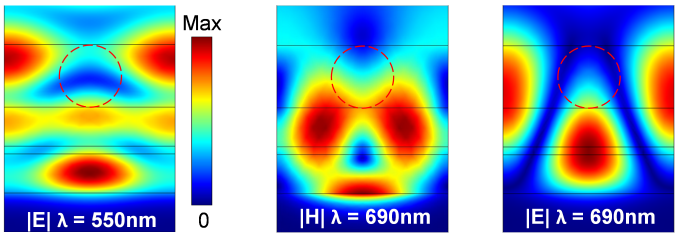

(a) (b) (c)

Figure 3.29: Field distributions (normalized to the incident field) in the yz-plane in the middle of neighboring particles in OSCs with Ag NP array embedded in a medium (corresponding to the dotted red curve in Fig. 3.28). (a) shows the electric field profile at 550nm. (b), (c) are the magnetic and electric field profiles at the peak 690nm. The dashed circle denotes the position of the NP. The maximum normalized field values for (a), (b) and (c) are 1.7, 6 and 4.5, respectively. The layers from the bottom to top are reflector, P3HT:PCBM, PEDOT:PSS, ITO, Ag NP layer with filled medium and the air, respectively.

By analyzing a single spherical particle (in section 3.2) in an absorbing medium we found that the small particles are better for near-field effect applications and large particles for scattering effect applications. In addition we illustrated that silver might be the best candidate for photovoltaic applications.

We performed a detailed numerical study (in section 3.3) on the influence of a metallic nanowire array for light absorption in organic solar cells. We analyzed the influence of particle spacing on the absorption. We found that the near-field enhancement is the main reason for the absorption enhancement in the active layer. For a thin active layer, such as 33nm, we noticed that a reasonable particle diameter of about 24nm is necessary for optimum absorption enhancement. With this diameter we find the best enhancement with a factor of around 1.56 for absorption (from 30% to 47%) and 1.63 for current density (from 6.7mA/cm^2 to 10.9mA/cm^2), bringing the structure close to the performance of a much thicker cell without MNPs. In addition, we noticed a strong decline of absorption enhancement as the particle coating thickness increases. However other researchers have shown that using a coating material with higher refractive index than organic materials could give extra enhancement. Our studies convey a strong interaction between the plasmonic enhancements and the absorption characteristics of the particular active material. Therefore, detailed numerics and experiments for various material configurations are needed to obtain a complete picture of plasmonic enhancement possibilities.

Our 3D simulations (in section 3.4) also confirmed the enhancement ben-

efits from the near-field effects of MNPs embedded in active layer in a more concrete OSC structure. We demonstrated that the current density is improved from 7.3mA/cm^2 to 10.7mA/cm^2 with an enhancement factor of ~ 1.46. Simulations with Au particles embedded in the buffer layer imply that the observed efficiency improvement in reported experiments with particles (both Ag and Au) in the buffer layer may be due to improved electrical effects like decreased resistance, improved exciton dissociation or carrier collection. The experiments (in section 3.5) carried out by colleagues at imec together with our simulations have confirmed that near-field enhancement of particles can boost the light harvesting.

Finally we also demonstrated the feasibility of the enhanced scattering of MNPs in boosting the efficiency of OSCs. By using arrays with larger NPs the light can be scattered into the active layer, improving the light harvesting. Further improvement can be achieved by filling the space between particles in the NP array with a medium.

References

[1] H. Hoppe and N. S. Sariciftci. *Organic solar cells: an overview.* Journal of Materials Research, 19(7):1924–1945, 2004.

[2] W. W. Kromhout. *UCLA engineers create tandem polymer solar cells that set record for energy-conversion.* Technical report, University of California, Los Angeles, February 2012.

[3] G. Yu, J. Gao, J. C. Hummelen, F. Wudl, and A. J. Heeger. *Polymer photovoltaic cells: enhanced efficiencies via a network of internal donor-acceptor heterojunctions.* Science, 270(5243):1789–1791, 1995.

[4] T. Soga. *Nanostructured Materials for Solar Energy Conversion.* Elsevier Science, 2006.

[5] V. Andersson, K. Tvingstedt, and O. Inganäs. *Optical modeling of a folded organic solar cell.* Journal of Applied Physics, 103(9):094520, 2008.

[6] B. P. Rand, S. R. Forrest, and P. Peumans. *Long-range absorption enhancement in organic tandem thin-film solar cells containing silver nanoclusters.* Journal of Applied Physics, 96(9):7519, 2004.

[7] J.Y. Kim, K. Lee, N.E. Coates, D. Moses, T.Q. Nguyen, M. Dante, and A.J. Heeger. *Efficient tandem polymer solar cells fabricated by all-solution processing.* Science, 317(5835):222–225, 2007.

[8] J. Yang, J. You, C.-C. Chen, W.-C. Hsu, H.-R. Tan, X. W. Zhang, Z. Hong, and Y. Yang. *Plasmonic polymer tandem solar cell.* ACS Nano, 5(8):6210–7, 2011.

[9] S. R. Forrest. *The limits to organic photovoltaic cell efficiency.* MRS Bulletin, 30(01):28–32, 2005.

[10] W.Y. Wong, X. Z. Wang, Z. He, B. D. Aleksandra, C. T. Yip, K. Y. Cheung, H. Wang, C. S. K. Mak, and W. K. Chan. *Metallated conjugated polymers as a new avenue towards high-efficiency polymer solar cells.* Nature Materials, 6(7):521–527, 2007.

[11] M. Westphalen, U. Kreibig, J. Rostalski, H. Lüth, and D. Meissner. *Metal cluster enhanced organic solar cells.* Solar Energy Materials and Solar Cells, 61(1):97–105, 2000.

[12] J. W. Wang, X.and Ho, Q. Yang, H. L. Tam, G. X. Li, K.W. Cheah, and F. Zhu. *Performance enhancement in organic photovoltaic devices using plasma-polymerized fluorocarbon-modified Ag nanoparticles.* Organic Electronics, 12(11):1943–1947, 2011.

[13] A.J. Morfa, K. L. Rowlen, T. H. Reilly III, M. J. Romero, and J. V. D. Lagemaat. *Plasmon-enhanced solar energy conversion in organic bulk heterojunction photovoltaics.* Applied Physics Letters, 92:013504, 2008.

[14] S. S. Kim, S. I. Na, J. Jo, D. Y. Kim, and Y. C. Nah. *Plasmon enhanced performance of organic solar cells using electrodeposited Ag nanoparticles.* Applied Physics Letters, 93(7):073307, 2008.

[15] D. Duche, P. Torchio, L. Escoubas, F. Monestier, J. J. Simon, F. Flory, and G. Mathian. *Improving light absorption in organic solar cells by plasmonic contribution.* Solar Energy Materials and Solar Cells, 93(8):1377–1382, 2009.

[16] X. Chen, C. Zhao, L. Rothberg, and M. K. Ng. *Plasmon enhancement of bulk heterojunction organic photovoltaic devices by electrode modification.* Applied Physics Letters, 93(12):123302, 2008.

[17] D. Qu, F. Liu, Y. Huang, W. Xie, and Q. Xu. *Mechanism of optical absorption enhancement in thin film organic solar cells with plasmonic metal nanoparticles.* Optics Express, 19(24):24795–803, 2011.

[18] K. Kim and D. L. Carroll. *Roles of Au and Ag nanoparticles in efficiency enhancement of poly(3-octylthiophene)/C[sub 60] bulk heterojunction photovoltaic devices.* Applied Physics Letters, 87(20):203113, 2005.

[19] D. H. Wang, K. H. Park, J. H. Seo, J. Seifter, J. H. Jeon, J. K. Kim, J. H. Park, O. O. Park, and A. J. Heeger. *Enhanced power conversion efficiency in PCDTBT/PC70BM bulk heterojunction photovoltaic devices with embedded silver nanoparticle clusters.* Advanced Energy Materials, 1(5):766–70, 2011.

[20] D. H. Wang, D. Y. Kim, K. W. Choi, J. H. Seo, S. H. Im, J. H. Park, O. O. Park, and A. J. Heeger. *Enhancement of donor-acceptor polymer bulk heterojunction solar cell power conversion efficiencies by addition of Au nanoparticles.* Angewandte Chemie International Edition, 50(24):5519–523, 2011.

[21] H. Shen, P. Bienstman, and B. Maes. *Plasmonic absorption enhancement in organic solar cells with thin active layers.* Journal of Applied Physics, 106(7):073109–073109, 2009.

[22] L. Hu, X. Chen, and G. Chen. *Surface-plasmon enhanced near-bandgap light absorption in silicon photovoltaics.* Journal of Computational and Theoretical Nanoscience, 5(11):2096–2101, 2008.

[23] Y. A. Akimov, W. S. Koh, and K. Ostrikov. *Enhancement of optical absorption in thin-film solar cells through the excitation of higher-order nanoparticle plasmon modes.* Optics Express, 17(12):10195–205, 2009.

[24] A. Paris, A. Vaccari, A. Calà Lesina, E. Serra, and L. Calliari. *Plasmonic scattering by metal nanoparticles for solar cells.* Plasmonics, 2012.

[25] D. Derkacs, S. H. Lim, P. Matheu, W. Mar, and E. T. Yu. *Improved performance of amorphous silicon solar cells via scattering from surface plasmon polaritons in nearby metallic nanoparticles.* Applied Physics Letters, 89(9):093103, 2006.

[26] S. Pillai, K. R. Catchpole, T. Trupke, and M. A. Green. *Surface plasmon enhanced silicon solar cells.* Journal of Applied Physics, 101(9):093105, 2007.

[27] S. H. Lim, W. Mar, P. Matheu, D. Derkacs, and E. T. Yu. *Photocurrent spectroscopy of optical absorption enhancement in silicon photodiodes via scattering from surface plasmon polaritons in gold nanoparticles.* Journal of Applied Physics, 101(10):104309, 2007.

[28] K. R. Catchpole and A. Polman. *Design principles for particle plasmon enhanced solar cells.* Applied Physics Letters, 93(19):191113, 2008.

[29] S. Mokkapati, F. J. Beck, A. Polman, and K. R. Catchpole. *Designing periodic arrays of metal nanoparticles for light-trapping applications in solar cells.* Applied Physics Letters, 95(5):053115, 2009.

[30] Y. A. Akimov and W. S. Koh. *Resonant and nonresonant plasmonic nanoparticle enhancement for thin-film silicon solar cells.* Nanotechnology, 21(23):235201, 2010.

[31] Y. A. Akimov and K Ostrikov E P Li. *Surface plasmon enhancement of optical absorption in thin-film silicon solar cells.* Physics Reports Review Section Of Physics Letters, pages 107–113, 2009.

[32] F.-J. Tsai, J.-Y. Wang, J.-J. Huang, Y.-W. Kiang, and C. C. Yang. *Absorption enhancement of an amorphous Si solar cell through surface plasmon-induced scattering with metal nanoparticles.* Optics Express, 18(102):A207–20, 2010.

[33] Y. A. Akimov and W. S. Koh. *Tolerance study of nanoparticle enhancement for thin-film silicon solar cells.* Applied Physics Letters, 99(6):063102, 2011.

[34] Y. A. Akimov and W. S. Koh. *Design of Plasmonic Nanoparticles for Efficient Subwavelength Light Trapping in Thin-Film Solar Cells.* Plasmonics, 6(1):155–161, 2010.

[35] Y. C. Chang, F. Y. Chou, P. H. Yeh, H. W. Chen, S.-H. Chang, Y. C. Lan, T. F. Guo, T. C. Tsai, and C. T. Lee. *Effects of surface plasmon resonant scattering on the power conversion efficiency of organic thin-film solar cells.* Journal of Vacuum Science & Technology B: Microelectronics and Nanometer Structures, 25(6):1899, 2007.

[36] S. Mokkapati, F. J. Beck, R. de Waele, A. Polman, and K. R. Catchpole. *Resonant nano-antennas for light trapping in plasmonic solar cells.* Journal of Physics D: Applied Physics, 44(18):185101, 2011.

[37] A. Pors, A. V. Uskov, M. Willatzen, and I. E. Protsenko. *Control of the input efficiency of photons into solar cells with plasmonic nanoparticles.* Optics Communications, 284(8):2226–2229, 2011.

[38] W. Ren, G. Zhang, Y. Wu, H. Ding, Q. Shen, and K. Zhang. *Broadband absorption enhancement achieved by optical layer mediated plasmonic solar cell.* Optics Express, 19(27):26536–26550, 2011.

[39] F. Moreno, J. M. Saiz, and F. González. *Interaction of nanoparticles with substrates : effects on the dipolar behaviour of the particles.* Optics Express, 16(17):2034–2038, 2008.

[40] E. D. Palik. *Handbook of Optical Constants of Solids.* Academic, New York, 1985.

[41] H. Wang, F. Tam, N. K. Grady, and N. J. Halas. *Cu nanoshells: effects of interband transitions on the nanoparticle plasmon resonance.* The Journal of Physical Chemistry. B, 109(39):18218–22, 2005.

[42] B. Zimmermann, M. Glatthaar, M. Niggemann, M. Riede, A. Hinsch, and A. Gombert. *ITO-free wrap through organic solar cells– A module concept for cost-efficient reel-to-reel production.* Solar Energy Materials and Solar Cells, 91(5):374–378, 2007.

[43] F. Monestier, J. Simon, P. Torchio, L. Escoubas, F. Flory, S. Bailly, R. Debettignies, S. Guillerez, and C. Defranoux. *Modeling the short-circuit current density of polymer solar cells based on P3HT:PCBM blend.* Solar Energy Materials and Solar Cells, 91(5):405–410, 2007.

[44] L. Novotny and B. Hecht. *Handbook of Optical Constants of Solids.* Cambridge University Press, Cambridge, 2006.

[45] C. Rockstuhl, S. Fahr, and F. Lederer. *Absorption enhancement in solar cells by localized plasmon polaritons.* Journal of Applied Physics, 104(12):123102, 2008.

[46] S.H. Park, A. Roy, S. Beaupré, S. Cho, N. Coates, J.S. Moon, D. Moses, M. Leclerc, K. Lee, and A.J. Heeger. *Bulk heterojunction solar cells with internal quantum efficiency approaching 100%.* Nature Photonics, 3(5):297–302, 2009.

[47] J. Y. Lee and P. Peumans. *The origin of enhanced optical absorption in solar cells with metal nanoparticles embedded in the active layer.* Optics Express, 18(10):10078–87, 2010.

[48] M. A. Sefunc, A. K. Okyay, and H. V. Demir. *Volumetric plasmonic resonator architecture for thin-film solar cells.* Applied Physics Letters, 98(9):093117, 2011.

[49] M. G. Kang, T. Xu, H. J. Park, X. Luo, and L. J. Guo. *Efficiency enhancement of organic solar cells using transparent plasmonic Ag nanowire electrodes.* Advanced Materials, 22(39):4378–83, 2010.

[50] H. Shen and B. Maes. *Combined plasmonic gratings in organic solar cells.* Optics Express, 19(106):A1202–A1210, 2011.

[51] F. C. Chen, J. L. Wu, C. L. Lee, Y. Hong, C. H. Kuo, and M. H. Huang. *Plasmonic-enhanced polymer photovoltaic devices incorporating solution-processable metal nanoparticles.* Applied Physics Letters, 95(1):013305, 2009.

[52] J. H. Lee, J. H. Park, J. S. Kim, D. Y. Lee, and K. Cho. *High efficiency polymer solar cells with wet deposited plasmonic gold nanodots.* Organic Electronics, 10(3):416–420, 2009.

[53] J. L. Wu, F. C. Chen, Y. S. Hsiao, F. C. Chien, P. Chen, C. H. Kuo, M. H. Huang, and C. S. Hsu. *Surface plasmonic effects of metallic nanoparticles on the performance of polymer bulk heterojunction solar cells.* ACS Nano, 5(2):959–67, 2011.

[54] B. Niesen, B.P. Rand, P. Van Dorpe, H. Shen, B. Maes, J. Genoe, and P. Heremans. *Excitation of multiple dipole surface plasmon resonances in spherical silver nanoparticles.* Optics Express, 18(18):19032–19038, 2010.

4

Metallic gratings

4.1 Introduction

Metallic nanoparticles can provide a decent light harvesting boost by blending them in the active layer, as discussed in the previous chapter. However they suffer experimentally from random distribution and clustering which may decrease the effects of plasmonic modes. As the advances in nanostructure fabrication technologies are developed, another prominent possibility for plasmonic structures are metallic gratings, including nano-structured metallic surfaces and periodic island gratings (both 1D and 2D). The experimental advantage of these types of metallic gratings over nanoparticles is the precise spatial control. The benefits of these gratings for light trapping are due to the strong and localized electromagnetic fields, which is a consequence of the excitation of plasmon polaritons, as we discuss in this chapter.

Various novel structures have been proposed to enhance light harvesting by using periodic metallic gratings in both organic [1–9] and inorganic solar cells [10–17]. In these structures plasmonic mode excitations are divided into localized modes, such as in nanoparticles (Localized Surface Plasmons, LSPs), and propagating modes at interfaces (Surface Plasmon Polaritons, SPPs). In structures with a layer of periodic metallic islands and a nearby metallic surface, mixtures of LSPs and SPPs can be excited depending on the period. For small periods (< 300nm), LSPs are mainly the reason for the light harvesting

improvement [2–5]. Scattering into SPPs comes into effect for larger grating periods [1, 6, 9, 10, 15]. In addition, the angular dependent dispersion behavior of these plasmonic modes is complex [18–22] due to the plasmonic bandgap introduced by the periodic corrugation. For example, two different kinds of modes are observed, the so-called bright and dark modes, with symmetric and antisymmetric field distributions respectively [22, 23]. They have been observed numerically [1] and experimentally [21, 24, 25] in some periodic plasmonic nanostructures. Dark modes are not excitable at the standard perpendicular incidence and need an oblique angle (or an asymmetric structure), so that optimized light trapping becomes more intricate.

In this chapter we mainly focus on metallic gratings to boost light harvesting in organic solar cells. In sections 4.2 to 4.4 we examine the combination of multiple gratings (1D), both on the front and back surface of the absorbing layer (model in Fig 4.1(a)). Most previous works focus on how a single nanophotonic feature can enhance the absorption. The study of combined elements to work towards the ultimate light-trapping configuration is less explored [4, 26, 27]. Indeed, it is an open question which combined structures will provide superposed resonances for maximum absorption enhancement.

Remark that our type of offset gratings can naturally form in fabrication processes with conformal layers, as was observed for example in [2]. Thus, here we complement these types of experiments with detailed numerical calculations. We start from structures with bare front and back gratings and end up with combined gratings. We discuss the modal origin of the enhanced absorption in the active layer. Moreover, to better understand the modes we examine the angle-dependent behavior, which is also important for solar cells in practice. Finally in section 4.5 we provide a preliminary investigation on Ag disk arrays localized in a buffer layer of organic solar cells, which is a 2D version of the 1D front grating.

4.2 Geometry and methodology

4.2.1 Structures and simulation techniques

As the model in Fig 4.1(a) illustrates we propose an OSC structure with front and back silver gratings. The gratings are characterized by the width and height w_{fg}, h_{fg} for front grating, w_{bg}, h_{bg} for back grating, and the period p. Throughout our investigations the thickness of the active layer is chosen to be 50nm, corresponding to the first Fabry-Perot maximum for the integrated absorption in a planar reference structure without gratings. Note that we include a half period offset between the two gratings, so that they operate quasi-independently. If the elements are on top of each other, thus without offset [4], this leads to different resonances than the individual cases, and can in general give stronger

reflections.

Both the excitation of localized modes and Bragg scattering into SPP modes play a role in the grating structures, and are influenced by the dimensions of the front and back grating teeth. Several trade-off mechanisms should be considered. Larger teeth can lead to stronger scattering, but also to more metal absorption, and the possibility of short circuits in experimental devices. In addition, larger front grating elements augment unwanted reflections. On the other hand, larger back gratings reduce the amount of available polymer. To have a better understanding we first perform studies for the structures with only a front and back grating as shown in (b) and (c).

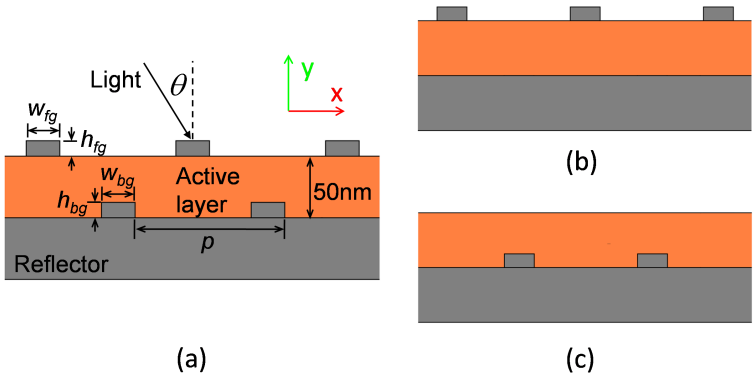

Figure 4.1: Schematic diagram of OSCs with combined gratings (front and back grating) (a), front grating only, (b) and back grating only (c). The gratings are characterized by the width and height w_{fg}, h_{fg} for front grating, w_{bg}, h_{bg} for back grating, and period p.

For the numerical calculations we used the finite element method [28] in 2D (see also section 2.6.2). The optical constants of P3HT:PCBM are determined by spectroscopic ellipsometry previously shown in Fig. 3.15. Silver data is extracted from [29]. In order to excite plasmonic modes we mainly consider TM polarized light (one H component perpendicular to the plane), later in this chapter we also discuss TE results. In simulations only one unit cell is included with periodic boundary conditions applied to the lateral sides. A soft light source with monochromatic plane wave emission is implemented above these structures to mimic the sunlight incidence. The light source is capable of emitting light with different incidence angle to have the angular response of the proposed structure. The whole structure is enclosed by Perfectly Matched Layer (PML) upper and lower sides.

In addition, to reveal the Bloch modes of the gratings, we perform a Bloch mode analysis with the propagation constant along the x-axis. To have an over-

all figure of merit, we calculate the total absorption η_A^{tot}, which integrates the absorption spectrum over the wavelength range from 300 to 800nm weighted by the AM 1.5G solar spectrum as defined in Eq. 3.3. Finally, we also provide expected current densities (see Eq. 3.4) for these structures.

4.2.2 Bright and dark modes

We first consider an easier reference structure, with only a flat silver substrate followed by a layer of P3HT:PCBM with 50nm thickness, forming a metal-dielectric-air (MDA) surface. The exact value of the SPP wave vector (k_{spp}) in this structure can be calculated numerically by solving a transcendental equation [30]

$$e^{2\gamma_2 d} = \frac{\left(\epsilon_1\gamma_2 - \epsilon_2\gamma_1\right)\left(\epsilon_3\gamma_2 - \epsilon_2\gamma_3\right)}{\left(\epsilon_1\gamma_2 + \epsilon_2\gamma_1\right)\left(\epsilon_1\gamma_2 + \epsilon_2\gamma_1\right)} \tag{4.1}$$

where $\gamma_i = \sqrt{k_{spp}^2 - k_0^2\epsilon_i}$, $i = 1, 2,$ and 3, and $\epsilon_i (i = 1,\ 2,\ 3)$ represent the permittivities of Ag, P3HT:PCBM and air, respectively. k_0 is the wave vector of light in air. It is known that there is a mismatch between the SPP wave vector and the in-plane wave vector (parallel to the silver substrate component) of light in air. As a result it is impossible to excite SPPs directly (see also section 2.3). Here by introducing gratings this mismatch can be overcome.

Due the scattering and the periodicity of the grating as discussed in chapter 2, light shining on the OSCs with gratings (front or back gratings) can be coupled to the SPP mode in the multilayered structure when satisfying the Bragg condition

$$k_{spp} = k_0 \sin\theta \pm NG = k_x \pm NG \tag{4.2}$$

where k_x is the in-plane light wave vector, θ is the light incidence angle with respect to the normal, N is any integer, $G = 2\pi/p$, and p is the grating period.

The SPP mode will be tuned if a periodic grating is introduced. However for shallow periodic perturbations, the SPP wave vector is still approximately according to Eq. 4.1. Here the OSCs with front, back or combined grating contain relatively large variations, so Eq. 4.1 is no longer valid. Therefore, to get the correct dispersion Bloch mode calculations are necessary.

As shortly described in chapter 2, a periodic perturbation will introduce a SPP bandgap due to the separation of the mode into two different modes, namely a bright and a dark mode. Here we look into these possible Bloch modes in the grating structures, calculated via the eigen-frequency solver implemented in COMSOL [28]. Figure 4.2 shows the calculated electric field distributions for bright and dark modes for gratings with period 490nm. Surface charge (sign '$\oplus$' and '$\ominus$' denote positive and negative charges respectively) distributions at the metallic reflector are also sketched, derived from the electric field distribution. The left column (a), (c) and (e) correspond to the bright modes of front, back

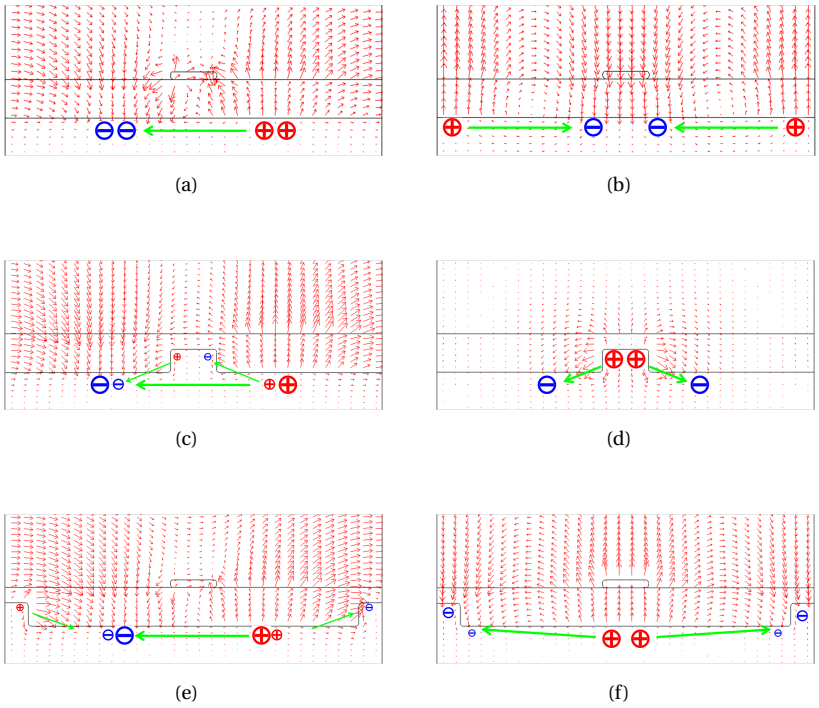

Figure 4.2: Schematics of electric field (red arrows) and surface charges (signs '⊕' and '⊖' denote positive and negative charges respectively) distribution for bright and dark modes. The left column (a), (c) and (e) correspond to the bright modes of front, back and combined grating respectively. The right column (b), (d) and (f) are the dark modes. Only the surface charges at metal reflector are considered. Due to the symmetry and charge conservation at the metal reflector the left column only yields non-zero net dipole along x-axis (parallel to reflector interface), while the right column yields non-zero net dipole along y-axis (perpendicular to reflector interface). In these figures, front gratings have a size of w_{fg} = 60nm, h_{fg} = 10nm, back grating with w_{bg} = 60nm, h_{bg} = 30nm, and period 490nm.

and combined grating respectively. The right column (b), (d) and (f) are the dark modes. Due to the symmetry and charge conservation at the metallic reflector the left column yields a non-zero net dipole moment along the x-axis, while the right column has a non-zero net dipole moment along the y-axis. Therefore, for TM incident light the net dipole of a bright mode can always couple with the incident light, since it has an overlap with the incident electric field. In contrast, for the dark mode with net dipole along the y-axis, it can only be excited with tilted light.

Figure 4.2 also indicates that for a constant period the size of the gratings will influence the resonance positions of SPP Bloch modes. Indeed, these geometrical parameters will influence the distance between the surface charges, which consequently changes the response of surface charges to the incoming light. As examples figure 4.3 shows the size dependence of the bright and dark modes in bare front and back gratings. For instance increasing the width of the front grating will separate the negative and positive charges further away leading to a red-shift of the bright mode. Increasing the height will bring the surface charges closer effectively resulting in a blue-shift of the bright mode, because of increased coupling between the front grating and metallic reflector. Whereas for the back grating increasing the width will decrease the effective distance between charges due to the more gentle deformation of the surface of metallic reflector; this results in a blue-shift of the bright mode. Increasing the height will induce a red-shift of the bright mode because of increased deformation of the surface.

A similar analysis can be done for the dark modes. However, note that the above analysis is not rigorous especially for the back grating. Since the deformation of the surface of the reflector will dramatically change the properties of Bloch modes. For example with a large width of back grating the geometry becomes grooves instead of ridges (the case considered here), and the properties of the Bloch modes in these two cases are very different [1].Therefore from these considerations the grating sizes have to be chosen carefully, in order to make the SPP Bloch mode contribute to the light harvesting.

4.3 Optimization for OSCs with a single grating

For the combined gratings there are five parameters to optimize, width and height of front and back gratings, w_{fg} and h_{fg}, w_{bg} and h_{bg} respectively and period p. To simplify the problem and reveal the influence of bare front or back grating on the performance it is necessary to investigate the OSCs with a single

[1] Further investigation shows that the frequency of the bright mode is larger than that of the dark mode for ridges, while for grooves it is the other way around. Meanwhile the corresponding size dependence is also different.

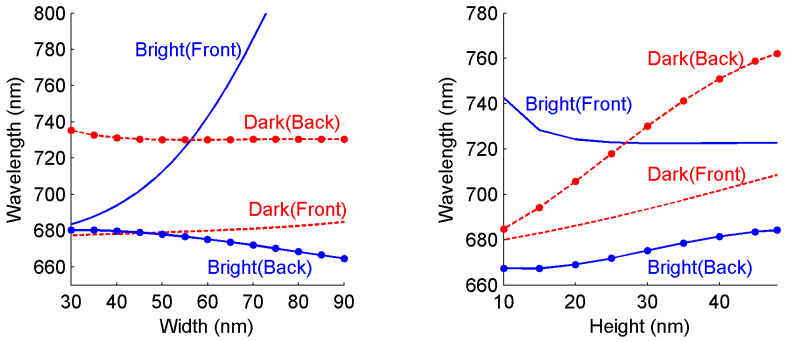

(a) (b)

Figure 4.3: Size dependence of bright and dark modes in bare front and back gratings. (a) Width dependence (w_{fg} or w_{bg}). For the front grating the height is fixed at 10nm, while back is 30nm. (b) Height dependence (h_{fg} or h_{bg}). For both the front and back gratings the width is fixed at 60nm. Dot marked lines for back grating, while no marker lines for front grating. Blue solid lines for bright modes, while red dash lines for dark modes. The period is fixed at 490nm.

grating, front or back. The figure of merit used to assess the influence of the gratings is the total absorption η_A^{tot} (see Eq. 3.3, wavelength range from 300nm to 800nm) in the active layer (P3HT:PCBM). Note that as a reference the total absorption in the planar reference structure without any grating (only a 50nm thick layer of P3HT:PCBM on top of reflector) is 48%.

The optimization is performed in a broad range of periods from 200nm to 600nm for each grating. Figure 4.4 (a) shows the maximum total absorption in the period range of 200–600nm versus different width for different particular front grating heights. The maximum total absorption is around 61% with height of 10nm or 15nm and width of 50nm to 70nm. To have more insight on the dependence of total absorption on the size of gratings, the data in (a) are plotted again in (c) with different x-axis. Comparing (a) with (c) one sees that the total absorption is relatively sensitive to the width of front grating for OSCs with bare front grating. Figures (b) and (d) show the maximum total absorption for back grating in the same way for front grating. The maximum total absorption 60% is achieved with 30nm height and 60nm width and is more sensitive to the height of the back grating.

Figure 4.5 shows the map of absorption versus wavelength and period for OSCs with bare front grating (a) and bare back grating (b). The sizes of gratings are w_{fg} = 60nm, h_{fg} = 10nm for front and w_{bg} = 60nm, h_{bg} = 30nm for back.

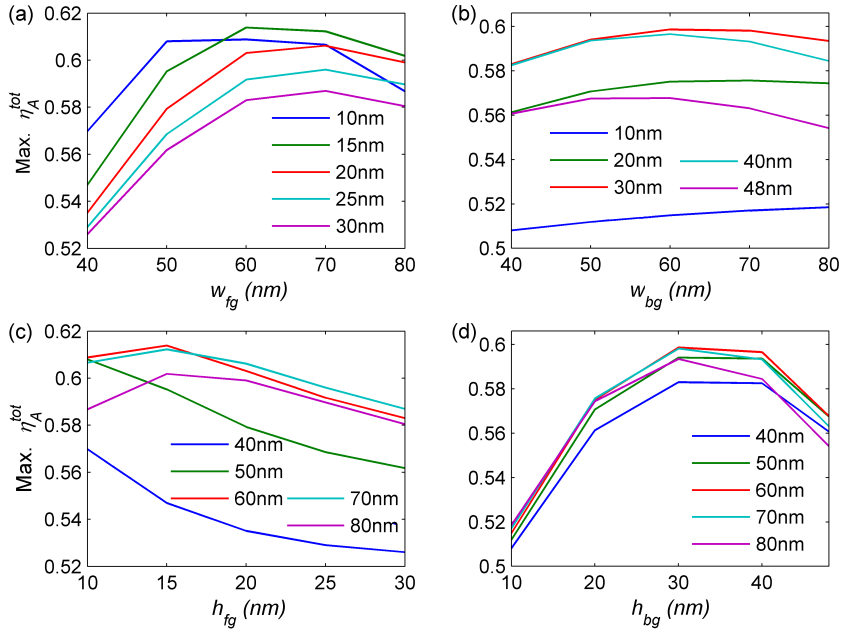

Figure 4.4: Maximum total absorption in the period range of 200nm–600nm in active layer versus width of front (a) and back (b) grating in OSCs with a single grating. Data on (c) and (d) are the same as (a) and (b) respectively but presented in different ways to have an impression of the sensitivity of absorption on width and height of grating.

Notice that peaks show up for period larger than 350nm at 700–800nm wavelength range in (a) for bare grating. These peaks correspond to the surface plasmon at the reflector/active layer interface (will be verified in Fig. 4.6), which are coupled from incident light by the scattering of the front grating. While the surface plasmon peaks for the bare back grating tend to excite at low wavelengths near 600nm with relatively weak intensity. This may be due to the ridge of the back grating not being a good scatterer [31].

Figure 4.6 (a) shows the absorption spectra for OSCs with bare front and back grating together with that of the planar reference structure. Note that the front grating tends to enhance absorption at large wavelengths, while the back grating enhances at small wavelengths (range 330–700nm). To get more insight the corresponding field distributions of the peaks (at 740nm and 670nm for front and back grating respectively) are shown in (b)–(e). A mixture between localized (LSP) and propagating (SPP) character is observed [21]. From the H magnitude we indeed see a strong coupling between the front grating element and the back silver interface (see Fig. 4.6 (b)). From the E magnitude on the

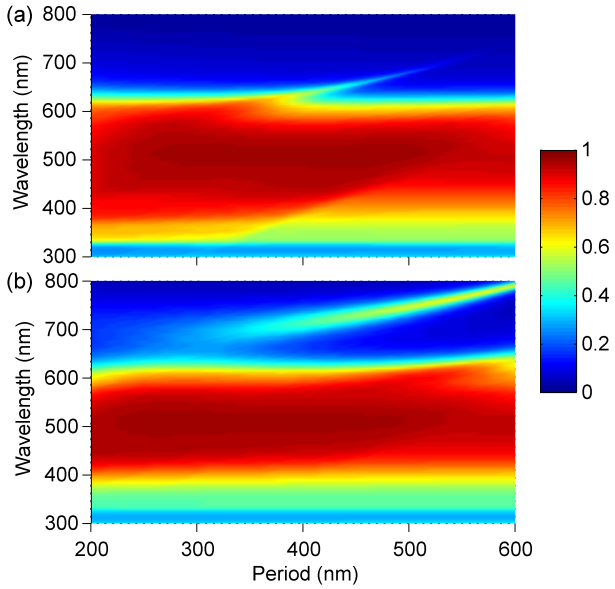

Figure 4.5: Maps of absorption in active layer vs. wavelength and period for OSCs with (a) bare front (w_{fg} = 60nm, h_{fg} = 10nm) and (b) bare back grating (w_{bg} = 60nm, h_{bg} = 30nm).

other hand we see a strong contribution from the localized excitation of the front element (see Fig. 4.6 (c)). It seems that the front grating is more favorable for SPP excitation. The excited SPP has a much stronger field intensity for the front grating. Stronger interaction between the front and reflector is observable. In contrast the back grating has a large interruption on the SPP along the surface because of its abrupt change of the surface continuity.

4.4 Combined grating structure

4.4.1 Optimizing the size of the geometry

Previously, sensitive parameters turned out to be the width of the front elements and the height of the back elements. Although the front grating with 15nm height gives somewhat larger absorption in the bare single front grating case, our exhaustive investigations show that 10nm height gives a better performance in the combined grating case. Therefore here we will fix the height of the front grating at 10nm, while the width of the back grating is 60nm. We only perform optimizations for the width (w_{fg}) of the front grating, the height (h_{bg}) of the

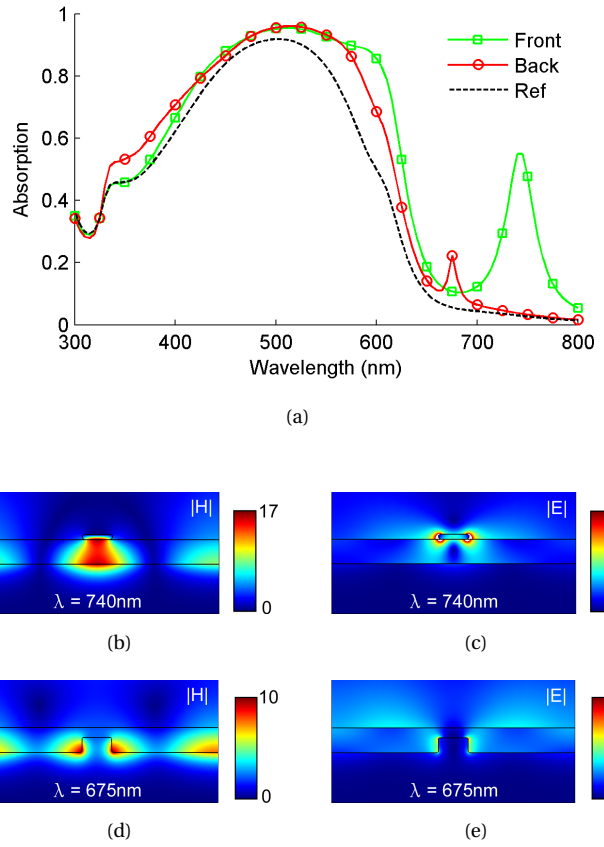

Figure 4.6: (a) Typical absorption spectrum in active layer (period = 490nm). The green (square marker) and red (circle marker) solid lines are the absorption in OSCs with bare front (w_{fg} = 60nm, h_{fg} = 10nm) and bare back (w_{bg} = 60nm, h_{bg} = 30nm) grating, respectively. The black dashed line is absorption in the reference structure without any grating. (b) and (c) is the magnitude distribution (normalized by the incident field) of electric and magnetic field for OSCs with bare front grating at wavelength 740nm (the surface plasmon peak of green curve) respectively. While (d) and (e) is that for OSCs with bare back grating at wavelength 670nm (the small surface plasmon peak of red curve).

back grating and the period. Figure 4.7 shows the maximum total absorption (with optimized period) for different combinations of w_{fg} and h_{bg}. The overall optimized total absorption is achieved with a width of 30nm for the back grating, a width of 60nm for the front grating and the period 490nm. With these parameters the total absorption is boosted from 48% (for reference structure) to 65%, thus an enhancement factor of 1.35. In the following sections we will focus on these optimized grating sizes (w_{fg} = 60nm, h_{fg} = 10nm, w_{bg} = 60nm, h_{bg} = 30nm and period 490nm) to have more insight.

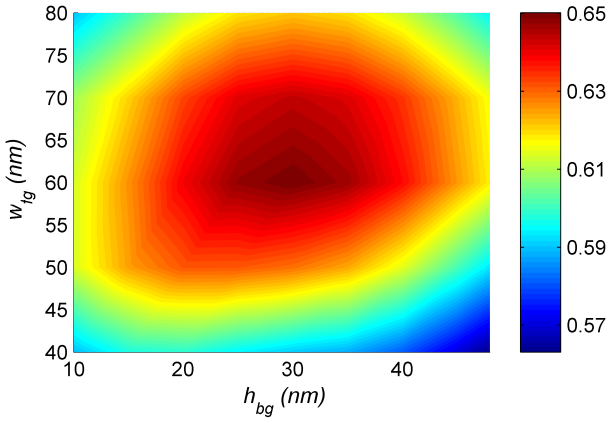

Figure 4.7: Maximum total absorption (with optimized period) in active material versus the width of front grating and the height of the back grating. The height of front grating is fixed at 10nm whereas the width of back grating is 60nm. The optimization is performed for the period for each combination of width w_{fg} of front grating and height h_{bg} of back grating.

4.4.2 Perpendicular incidence

We consider the optimized period of 490nm (value determined in the previous subsection), and examine the absorption in the organic layer for perpendicular TM incidence, see Fig. 4.8(a). Here the spectrum is indicated for four structures: the planar reference structure without gratings, the front grating case with a flat back surface, the back grating case with a flat air-organic interface, and finally the full combined grating case.

Examining the combined spectra in Fig. 4.8(a) provides insight in the particular contributions. First, we notice the big peak around 740nm and the shoulder around 600nm in both the front grating and the combined grating case. In contrast, the shoulder of the combined case around 350nm fits well with the back

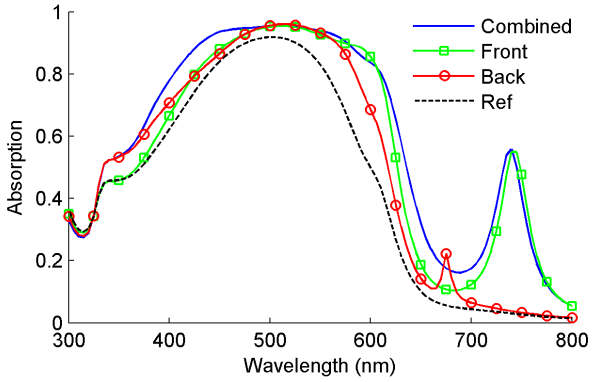

(a)

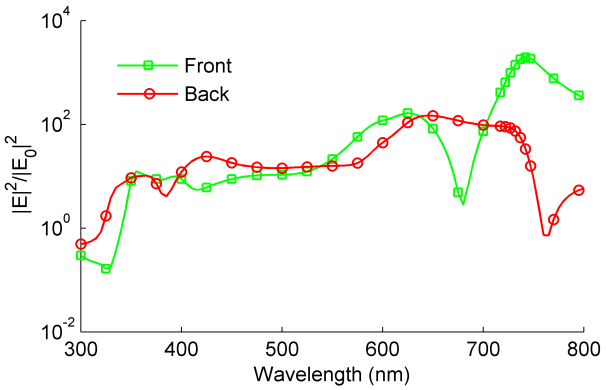

(b)

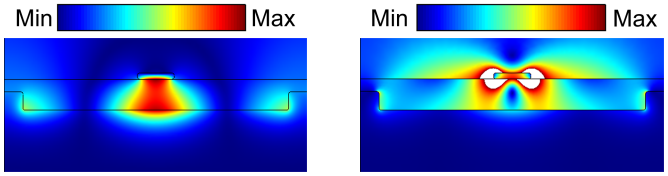

(c) (d)

Figure 4.8: (a) The absorption spectra of the organic layer with combined grating (blue solid line), front grating only (green dash-dotted), back grating only (red dashed) and planar reference structure without grating (black dotted). (b) Intensity enhancement spectrum at a point close to a lower corner of front grating (blue solid line) and at a point close to an upper corner of back grating (red dashed line) for combined grating, normalized by the incident field. (c) and (d) show the E and H amplitude profile at wavelength 740nm for the combined case.

grating absorption. In addition, the small peak around 675nm of the back grating case seems to help the combined case in that range. Thus, the back and the front gratings make fairly independent contributions to different wavelength ranges and one arrives at a broadband enhancement from 350nm to 800nm in the combined grating structure.

The broadband enhancement is attributed to the enhanced field intensity in the vicinity of gratings due to the excitation of LSPs and SPPs at different wavelengths. To verify this, Fig. 4.8(b) shows the intensity enhancement in the organic layer in the vicinity of the front and back teeth for combined grating structures. The intensity enhancement is the intensity ratio at a certain point between the cell with a combined grating and the incident field. We notice the strongly enhanced intensity at larger wavelengths ($\lambda > 600$nm), but the point of largest ratio (near front or back grating) depends on the particular wavelength range.

To better understand the property of the main peak at 740nm, electric E and magnetic H field magnitude distributions are shown Fig. 4.8(c) and (d). Here similar to the field distributions for bare front and back grating (Fig. 4.6 (b)–(e)) a mixture between localized (LSP) and propagating (SPP) character is still observed, in spite of a much stronger perturbation. Moreover the field distribution looks like a superposition of SPP fields (although peaks are not at the same wavelength) in Fig. 4.6 (b)–(e), indicating that the coupling between the front and back gratings is relatively small at this optimized period.

4.4.3 Period dependence

The period has a strong influence on the grating behavior. Therefore, we consider here the dependence on the period for the combined grating structure, see Fig. 4.9(a) for normal TM incidence.

For periods larger than 350nm there is an important absorption peak showing up at larger wavelengths ($\lambda > 650$nm), already discussed in the previous section. This plasmonic resonance red-shifts as the period increases, and finally leaves the absorption tail of the organic material. The strong absorption in the wavelength range 400 to 650nm for periods between 300nm and 600nm is due to more localized grating intensity enhancements, as they are quasi-independent of the period (but more dependent on the grating teeth size, not shown). As the period decreases below 300nm, the filling factor of the gratings gets large, leading e.g. to strongly increased reflection. All of these factors together result in the relatively small absorption in the period range 200–300nm and the wavelength range 400–650nm.

These trends are reflected in Fig. 4.9(b) for the total absorption. At first more light reaches the active layer, leading to a strong absorption increase. After the

appearance of the large peak plasmonic mode a wide optimal plateau (with maximum at 490nm) is reached, after which the mode shifts out of the absorption tail and absorption decreases.

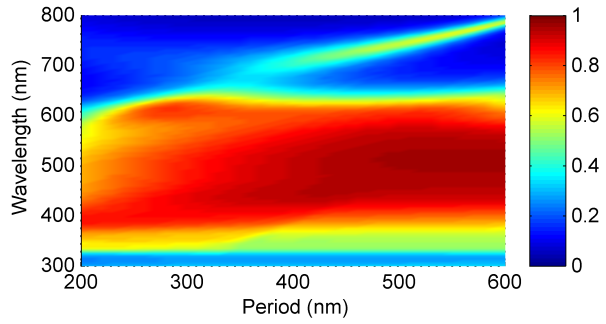

(a)

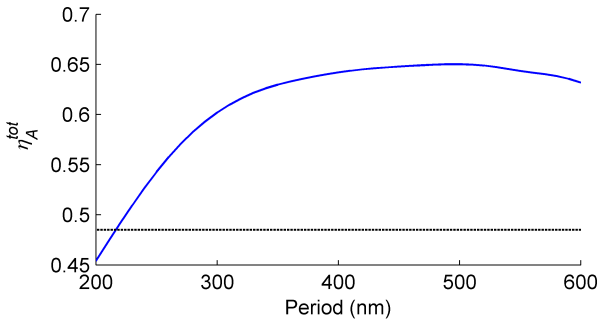

(b)

Figure 4.9: (a) Map of absorption in the organic layer versus the wavelength of incident light and the grating period. (b) The period dependence of total absorption (blue solid line). The value for the reference structure is indicated by the black dotted line.

4.4.4 Angular dependence

For practical reasons it is important to explore the angular performance of cells with plasmonic gratings. In addition, these studies give insight into the plasmonic modes, and even provide further opportunities for optimization. Fig. 4.10 maps the absorption in the active layer versus wavelength and light incidence angle for the previously introduced structures: combined, front, back and planar case, respectively.

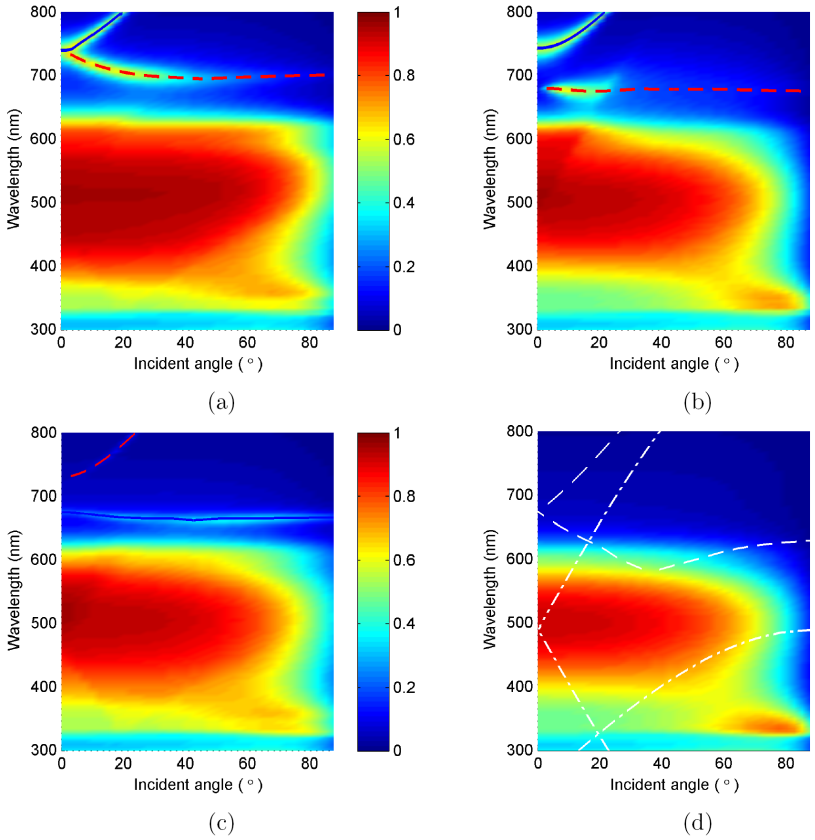

Figure 4.10: Angular dependence of absorption with (a) combined grating, (b) front grating, (c) back grating, (d) planar device. Blue solid and red dashed lines superimposed in (a)–(c) are calculated Bloch mode dispersion curves. White dashed and dash-dotted lines in (d) are folded dispersion lines of the planar reference structure (SPP mode) calculated by Eqs. 4.1 and 4.2 and the folded air light line, respectively.

In Fig. 4.10(d) we superimpose the folded dispersion of the SPP mode in the planar structure (white dashed line). In addition, we add the folded light line in air (white dash-dotted line). The light line weakly influences the features in Fig. 4.10(a)–(c), as observed before [19]. The folded SPP dispersion is useful to predict mode (or bandgap) positions at normal incidence when a grating perturbation is introduced. The position of bandgaps around 680nm for the front and back grating case corresponds well, for the combined case the gap has a redshift. In our case the grating perturbation is relatively large, but there is still a decent prediction for the mode bandgaps at perpendicular incidence.

To better understand the properties and splitting of the plasmonic modes we performed Bloch mode calculations with varying propagation constant along the horizontal x-axis k_x. We superimpose the dispersion of two Bloch modes on the absorption map in Fig. 4.10(a)–(c): a bright mode (solid blue line) and a dark mode (dashed red line). We observe very good fits between the Bloch modes and the peaks in the absorption map, although these are different types of calculations, verifying the importance of the Bloch modes for absorption enhancement. We also see that the bright mode in the combined case corresponds well with the front grating case; however, the dark mode of the combined case is shifted. The back grating seems to have a strong influence on the dark mode of the combined case, leading to a very small bandgap. Finally, remark that for each grating structure one of the branches has a flat dispersion curve, indicating a more localized character.

To view the nature of the modes, we plot the H magnitude distribution for Bloch modes at $k_x = 0$ in Fig. 4.11. The '+' and '-' signs indicate π phase differences in the field profiles. We observe that the left column (Fig. 4.11(a), (c), (e)) and the right column (Fig. 4.11(b), (d), (f)) have a different symmetry with respect to the plane in the middle of the structure. This leads to the bright and dark character of the modes, meaning that they can or cannot be excited by perpendicularly incident light, respectively. As discussed in section 4.2.2 the symmetry of dark modes leads to a zero overlap with the incoming plane wave, or to a zero net dipole moment [1, 23]. The dark mode can only be excited when there is an asymmetry introduced into the system by means of tilting the light incidence or by breaking the symmetry of the geometry. As a consequence, we only observe the dark modes in Fig. 4.10(a)-(c) for non-perpendicular incidence. Notice that the combined case modes, both bright and dark, look like superpositions of the separate front and back modes, corresponding with the qualitatively similar dispersion curves.

Figure 4.12 shows the angular dependence of the integrated absorption. Notice that the total absorption for TM reaches its maximum at 10° incidence for the combined grating case, because of the influence of the dark mode. At normal incidence the combined grating cell reaches around 65%, an enhancement

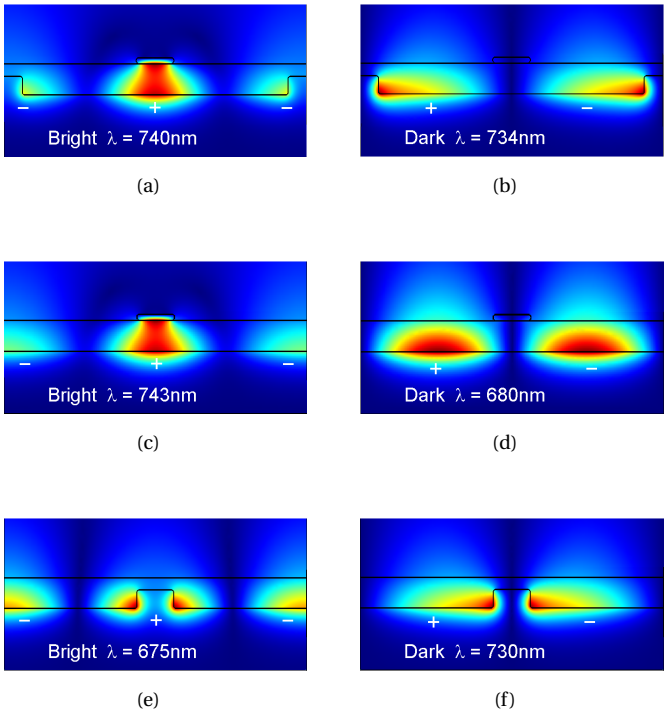

(a) (b) (c) (d) (e) (f)

Figure 4.11: H field magnitude distribution of Bloch modes. Left column shows bright modes, right column are dark modes. (a) and (b) combined grating, (c) and (d) front grating, (e) and (f) back grating case. The '+' and '-' signs denote π phase differences in the field profiles.

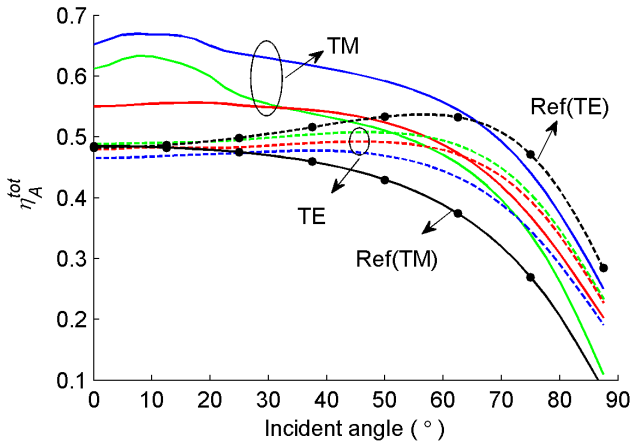

Figure 4.12: Total absorption versus incidence angle for TM (solid lines) and TE (dashed) polarizations. Blue: combined grating; green: front grating; red: back grating. The dot marked lines (both dashed and solid) for the planar structure.

factor of about 1.35 compared with the 48% of a planar cell, as discussed previously. The dark mode effect at 10° leads to a further 67% absorption. Enhancement is quite angle insensitive and observed over a large angular range. Up to around 70° the TM absorption is still larger than that of the reference at normal incidence. We can also see that the combined grating case dominates over the front and back single grating cases. Although our structures were mainly optimized for perpendicular incidence, we remark that the dark modes provide an important extra route towards enhancement.

As a final step we should consider the TE polarization performance, also shown in Fig. 4.12. For TE it is not possible to excite plasmonic modes, so in this case the silver grating works as absorber and scatterer. Only a very small enhancement near perpendicular incidence for the front grating case is observed. A small decrease of absorption for the back and combined cases is seen for perpendicular incidence, because the presence of the back grating reduces the active material. So for unpolarized perpendicular light, gratings can still enhance the absorption with an average, relatively good enhancement factor of around 1.2.

Another important parameter which assesses the overall electronic performance is the current density. Figure 4.13 shows the current density according to Eq. 3.4 with the assumption that the internal quantum efficiency is 1. Under TM-polarized normal incidence the reference has a current density of 11.6mA/cm^2, while the combined grating can enhance the current density to

16.5mA/cm^2 with an enhancement factor of 1.42. The current density reaches its maximum 17.1mA/cm^2 with a small incident tilt of around 10°.

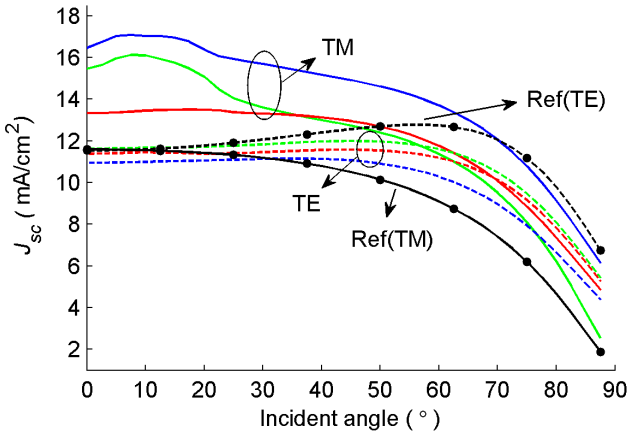

Figure 4.13: Current density versus incidence angle for TM (solid lines) and TE (dashed) polarizations. Blue: combined grating; green: front grating; red: back grating. The dot marked lines (both dashed and solid) for the planar structure.

4.5 Organic solar cells with disk arrays

4.5.1 Geometry and simulation setup

Here we consider a 2D version of the front grating structure as shown in 4.14. A more concrete model consisting of ITO coated glass and buffer layer PEDOT:PSS is employed. The nano-disk array with square lattice is enclosed inside the buffer layer in direct contact with ITO. Both the reflector and disk are chosen to be silver. Refractive indices of the other layers are plotted in Fig. 3.15 (b). The thickness of ITO and P3HT:PCBM are constants throughout, 100nm and 50nm respectively. The buffer layer thickness depends on the nano-disk height as it is always 2nm thicker than the nano-disks to avoid direct contact between nano-disk and active layer.

We only consider the x-polarized incident light since it is insensitive to the polarization under normal incidence. In simulations only quarter of a unit cell is used by applying appropriate boundary conditions (PEC to side boundaries perpendicular to x-axis, PMC to side boundaries perpendicular to y-axis). The structure performance is assessed by the current density compared with that of the reference structure, as defined in Eq. 3.4. Note that the current density

for the reference structure varies slightly for different buffer layer thicknesses. The size of the nano-disks is not intensively investigated. We only show three different sizes to demonstrate the feasibility of the disk array.

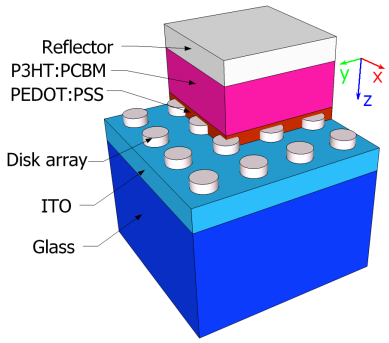

Figure 4.14: Schematic figure of OSCs with a disk array in the PEDOT:PSS layer.

4.5.2 Results

Figure 4.15 shows the current density enhancement (ratio of J_{sc} of OSCs with to without nano-disks) for three different disk sizes. In section 4.3 we noticed that for the 1D front grating 10nm thickness and 60nm width is almost the optimal one. However here due to the higher refractive index and absorption of the surrounding, optimal parameters differ. Also the optimal period shortens due to the larger effective refractive index in the layer structure. From the three different sizes of nanodisk shown in Fig. 4.15, disk with diameter 60nm, height 28nm and period 270nm give the best current density enhancement factor of around 1.21, boosting from 9.6mA/cm^2 to 11.7mA/cm^2.

Figure 4.16 shows the absorption spectra for the optimal size of the nano-disk array together with the reference. The enhancement is mainly around 600–650nm. The absorption enhancement in this range is plotted in (b) with a high peak observable. In addition a small peak at 470nm is present. To have more insight Figure 4.17 (a) and (b) show the electric and magnetic field distributions at wavelength 630nm. Similar to the 1D front grating here a mixture between localized and propagating characters can be observed. But the SPP mode is weakly excited due to reduced coupling between disk and reflector resulting from the presence of a buffer layer. A guided mode character is noticed in the OSCs layers from the electric field distribution in (c), which is responsible for the small peak at 470nm in Fig. 4.16 (a).

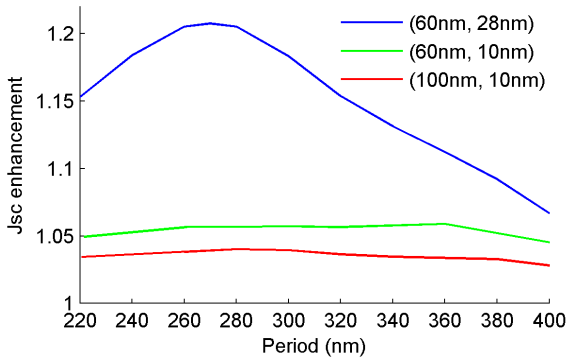

Figure 4.15: Current density enhancement versus period for various disk sizes (diameter, height).

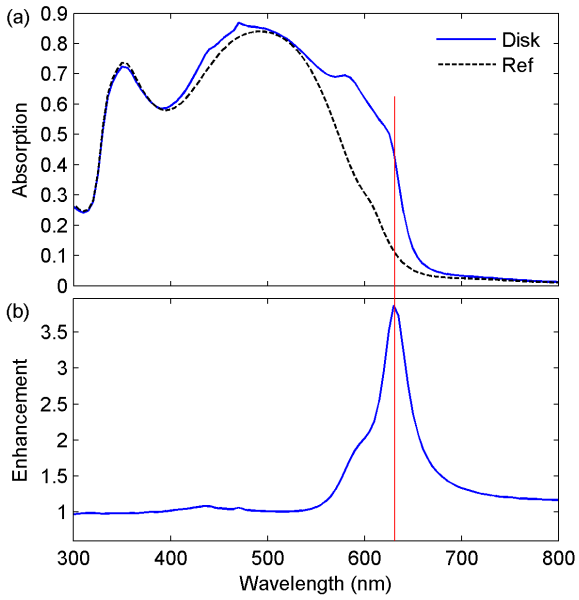

Figure 4.16: (a) Absorption spectra for OSCs with and without disks. The disk array period is 270nm. (b) Spectral absorption enhancement, the ratio of the absorption in OSCs with to without disks in (a).

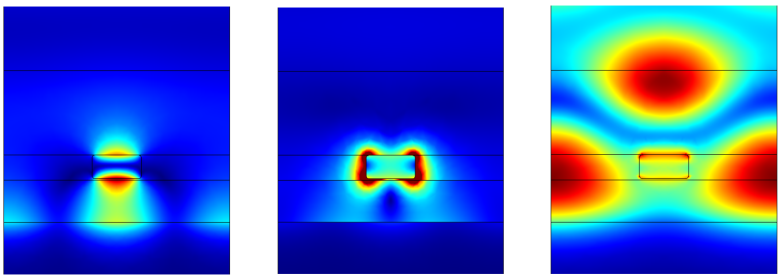

(a) (b) (c)

Figure 4.17: The magnitude distributions of magnetic (a) and electric (b) fields in the xz-plane at wavelength 630nm corresponding to the absorption enhancement in Fig. 4.16(b). (c) shows the magnitude distribution of electric field in the yz-plane at wavelength 470nm corresponding to the small peak in Fig. 4.16(a). In these three figures the bottom layer is the reflector (inverse of Fig. 4.14).

4.6 Conclusion

In conclusion, we investigated the influence of combined gratings on the absorption in the active layer of organic solar cells. A broadband absorption enhancement over a large angular range observed. With an optimal period factors of 1.35 and 1.42 are respectively reached for absorption and current density enhancements for TM polarized perpendicular light. The current density is boosted from 11.6mA/cm^2 to 16.5mA/cm^2 and reaches its maximum 17.1mA/cm^2 at a light incidence angle of 10°. The enhancements are traced back to modes in the individual front or back grating cases, so the structures function semi-independently. Detailed Bloch dispersion calculations present the mixed character of localized and propagating plasmonic modes, and the bright and dark character. The dark modes provide a mechanism for absorption over a large angular range. We find that the TE component of the solar light will not decrease the observed enhancement strongly.

For the OSCs with disk arrays we also see a decent current density enhancement factor of about 1.21, enhancing from 9.6mA/cm^2 to 11.7mA/cm^2. Meanwhile it is not sensitive to the polarization of the incoming light. Similarly both guided modes and a mixture of localized and propagating character are observed and responsible for the enhancement.

References

[1] A. Abass, H. Shen, P. Bienstman, and B. Maes. *Angle insensitive enhancement of organic solar cells using metallic gratings.* Journal of Applied Physics, 109(2):023111–023111, 2011.

[2] M. G. Kang, T. Xu, H. J. Park, X. Luo, and L. J. Guo. *Efficiency enhancement of organic solar cells using transparent plasmonic Ag nanowire electrodes.* Advanced Materials, 22(39):4378–83, 2010.

[3] C. Min, J. Li, G. Veronis, J. Y. Lee, S. Fan, and P. Peumans. *Enhancement of optical absorption in thin-film organic solar cells through the excitation of plasmonic modes in metallic gratings.* Applied Physics Letters, 96(13):133302, 2010.

[4] M. A. Sefunc, A. K. Okyay, and H. V. Demir. *Plasmonic backcontact grating for P3HT:PCBM organic solar cells enabling strong optical absorption increased in all polarizations.* Optics Express, 19(15):14200–9, 2011.

[5] M. A. Sefunc, A. K. Okyay, and H. V. Demir. *Volumetric plasmonic resonator architecture for thin-film solar cells.* Applied Physics Letters, 98(9):093117, 2011.

[6] K. Tvingstedt, N. K. Persson, O. Inganäs, A. Rahachou, and I. V. Zozoulenko. *Surface plasmon increase absorption in polymer photovoltaic cells.* Applied Physics Letters, 91(11):113514, 2007.

[7] W. Bai, Q. Gan, G. Song, L. Chen, Z. Kafafi, and F. Bartoli. *Broadband short-range surface plasmon structures for absorption enhancement in organic photovoltaics.* Optics Express, 18(S4):A620–30, 2010.

[8] H. Shen and B. Maes. *Combined plasmonic gratings in organic solar cells.* Optics Express, 19(106):A1202–A1210, 2011.

[9] Y. Liu and J. Kim. *Polarization-diverse broadband absorption enhancement in thin-film photovoltaic devices using long-pitch metallic gratings.* Journal of Optical Society America B, 28(8):1934–1939, 2011.

[10] V. E. Ferry, L. A. Sweatlock, D. Pacifici, and H. A. Atwater. *Plasmonic nanostructure design for efficient light coupling into solar cells.* Nano Letters, 8(12):4391–7, 2008.

[11] V. E. Ferry, M. A. Verschuuren, H. B. T. Li, R. E. I. Schropp, H. A. Atwater, and A. Polman. *Improved red-response in thin film a-Si:H solar cells with soft-imprinted plasmonic back reflectors.* Applied Physics Letters, 95(18):183503, 2009.

[12] V. E. Ferry, M. A. Verschuuren, H. B. T. Li, E. Verhagen, R. J. Walters, R. E. I. Schropp, H. A. Atwater, and A. Polman. *Light trapping in ultrathin plasmonic solar cells.* Optics Express, 18(S2):A237–45, 2010.

[13] A. Abass, K. Q. Le, A. Alù, M. Burgelman, and B. Maes. *Dual-interface gratings for broadband absorption enhancement in thin-film solar cells.* Physical Review B, 85(11):1–8, 2012.

[14] R. A. Pala, J. White, E. Barnard, J. Liu, and M. L. Brongersma. *Design of plasmonic thin-film solar cells with broadband absorption enhancements.* Advanced Materials, 21(34):3504–3509, 2009.

[15] C. C. Chao, C. M. Wang, and J. Y. Chang. *Spatial distribution of absorption in plasmonic thin film solar cells.* Optics Express, 18(11):11763–71, 2010.

[16] W. Bai, Q. Gan, F. Bartoli, J. Zhang, L. Cai, Y. Huang, and G. Song. *Design of plasmonic back structures for efficiency enhancement of thin-film amorphous Si solar cells.* Optics Letters, 34(23):3725–7, 2009.

[17] E. Battal, T. A. Yogurt, L. E. Aygun, and A. K. Okyay. *Triangular metallic gratings for large absorption enhancement in thin film Si solar cells.* Optics Express, 20(9):9458–9464, 2012.

[18] S. C. Kitson, W. L. Barnes, and J. R. Sambles. *Full photonic band gap for surface modes in the visible.* Physical Review Letters, 77(13):2670–2673, 1996.

[19] W. L. Barnes, T. W. Preist, S.C. Kitson, and J. R. Sambles. *Physical origin of photonic energy gaps in the propagation of surface plasmons on gratings.* Physical Review. B, 54(9):6227–6244, 1996.

[20] W. L. Barnes, S. C Kitson, T. W. Preist, and J. R. Sambles. *Photonic surfaces for surface-plasmon polaritons.* Journal of Optical Society of America A, 14(7):1654–1661, 1997.

[21] A. Christ, T. Zentgraf, S. Tikhodeev, N. Gippius, J. Kuhl, and H. Giessen. *Controlling the interaction between localized and delocalized surface plasmon modes: experiment and numerical calculations.* Physical Review B, 74(15):1–8, 2006.

[22] W. L. Barnes, A. Dereux, and T. W. Ebbesen. *Subwavelength optics.* Nature, 424:824–830, 2003.

[23] P. Nordlander, C. Oubre, E. Prodan, K. Li, and M. I. Stockman. *Plasmon hybridization in nanoparticle dimers.* Nano Letters, 4(5):899–903, 2004.

[24] A. Hibbins, W. Murray, J. Tyler, S. Wedge, W. Barnes, and J. Sambles. *Resonant absorption of electromagnetic fields by surface plasmons buried in a multilayered plasmonic nanostructure.* Physical Review B, 74(7):1–4, 2006.

[25] S. R. K. Rodriguez, A. Abass, B. Maes, O. T. A. Janssen, G. Vecchi, and J. G. Rivas. *Coupling bright and dark plasmonic lattice resonances.* Physical Review X, 1(2):021019, 2011.

[26] P. Bermel, C. Luo, L. Zeng, L. C. Kimerling, and J. D. Joannopoulos. *Improving thin-film crystalline silicon solar cell efficiencies with photonic crystals.* Optics Express, 15(25):16986–17000, 2007.

[27] J. N. Munday and H. A. Atwater. *Large integrated absorption enhancement in plasmonic solar cells by combining metallic gratings and antireflection coatings.* Nano Letters, 11(6):2195–201, 2011.

[28] Comsol Multiphysics. *http://www.comsol.com.*

[29] E. D. Palik. *Handbook of Optical Constants of Solids.* Academic, New York, 1985.

[30] S. A. Maier. *Plasmonics: Fundamentals and Applications.* Springer Verlag, 2007.

[31] G. Brucoli and L. Martín-Moreno. *Comparative study of surface plasmon scattering by shallow ridges and grooves.* Physical Review B, 83(4):045422, 2011.

5

Metallic gratings with tapered slits

5.1 Introduction

For a single aperture in a perfectly conducting thin metal film, the transmission is approximately proportional to $(r/\lambda)^4$ (r is the radius of the aperture and λ the wavelength) as predicted by Bethe's theory [1]. The transmission drops fast in the subwavelength range. However in 1998 Ebbesen *et al.* [2] demonstrated remarkable transmissions, which are termed as extraordinary optical transmission (EOT), through a thin Ag film with 2D arrays of holes, beyond that of a single hole predicted by Bethe's theory. Subsequently tremendous investigation has been dedicated to its mechanisms, both theoretically and experimentally [2–7]. In general it is believed that the excitation of surface plasmons due to the periodicity of the array plays an important role. A related EOT phenomenon is observed in a simpler 1D metallic grating with straight slits [8–10], where the peaks are known to be the Fabry-Perot resonance in the slits [11, 12].

For a single slit with any width there always exists a guided TEM mode, which is a plasmonic mode in the so-called metal-insulator-metal (MIM) waveguide [13]. In contrast, a mode in a subwavelength diameter aperture decays exponentially into the hole, the mode being below cut-off. Therefore the mechanisms behind EOT of 1D metallic gratings and hole arrays are different. For the 1D metallic gratings the peaks can be predicted by the FP resonances in the slits. In contrast for a thin metal film with holes with square lattice, the position

of transmission peaks due to surface plasmons are approximately determined by [3]:

$$\lambda = \frac{p}{i^2 + j^2}\sqrt{\frac{\epsilon_m \epsilon_d}{\epsilon_m + \epsilon_d}}, \tag{5.1}$$

where ϵ_m and ϵ_d is the dielectric constant of metal and interface medium, respectively, p is the period of grating (the lattice constant), i and j are integers.

EOT offers strongly localized field enhancements in addition to a large transmission, with potential applications in nonlinear optics, Raman spectroscopy [14], sensing [15–17], light harvesting [18] etc. However, due to the resonant Fabry-Perot mechanism involved often a relatively narrow bandwidth is affected, which is unsuitable for some applications. On the other hand, broadband transparency has been achieved in related structures, e.g. using oblique incidence TM polarization [10, 19], or by connecting rectangular apertures with narrower slits [20]. In the latter example the thin gratings operate at wavelengths beyond the FP resonances of plasmonic modes in the slits. In [10] broadband high transmission was explained as impedance matching between the slit and the surrounding at oblique incident angle, which is termed as the plasmonic Brewster angle in [19].

Here, we propose metallic gratings with tapered slits for TM polarized light, which offer a much broader transmission window. Similar structures have been investigated experimentally and numerically [21–23]. However they focused on the short wavelength range and relatively large periods, with the aim to maximize the resonances. Here we investigate at longer wavelengths and with smaller periods, in order to achieve non-resonant and broadband transmission. We employ both FEM and a semi-analytic method for investigations. By gradually varying the impedance from input to output plane, we effectively destroy the Fabry-Perot type resonant conditions of plasmonic modes in the slit, yielding a non-resonant and thus broadband and wide-angle large transmission in the infrared. In addition, the localization of the field is confined to one plane of the structure, instead of over the whole lossy waveguide as in the traditional structures with straight sidewalls. Furthermore in section 5.3 we demonstrate polarization insensitive 2D gratings with tapering. These grating structures with enhanced and broadened transmission could be useful for solar cells e.g. as transparent electrodes.

5.2 1D gratings

5.2.1 Structure and simulation setup

The grating under investigation is shown in Fig. 5.1. It consists of tapered slits on top of a substrate, characterized by the thickness t, period p, and widths

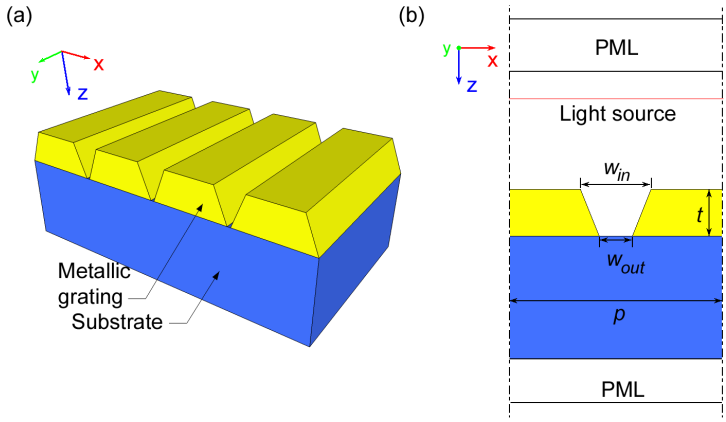

Figure 5.1: (a) Schematics of 1D metallic grating with tapered slits. (b) Model with one unit cell used in simulations together with size characterization. Periodic boundary conditions are used for the dash-dot lines. A light source is implemented inside the cell with monochromatic wave generation. The upper and lower domains are set to be perfectly matched layers to absorb reflected and transmitted light.

w_{in} and w_{out} at the entrance and exit of the slit, respectively. In a first approach, analysis is performed with rigorous calculations (finite element method - FEM [24], see also section 2.6). The schematic model with one unit cell is shown in Fig. 5.1(b). Only one period is used in simulations by applying Floquet periodic boundary conditions to the sides with TM-polarized (H field parallel to y-axis) monochromatic plane waves impinging on it. The light source is introduced inside the model by using assembly in COMSOL [24], which can give a soft source. For the upwards and downwards direction PML domains are set to absorb the reflected and transmitted light. The simulations are carried out in a wavelength range of $0.3 - 10\mu$m. The metal grating is assumed to be silver [25].

In addition to the numerical simulations a semi-analytic method (transmission line theory - TL [19]) is also applied here to have a better understanding. Other more complex models and theories were proposed for EOT [26, 27], but under certain conditions the efficient TL model provides effective characterization.

5.2.2 TL model for gratings

We introduce now the employed TL approach, which was originally developed for non-tapered slits [19]. The grating with straight sidewalls, together with a semi-infinite substrate and surrounding (Fig. 5.2(a)), can be modeled as a two-port network terminated by two semi-infinite TLs at the input and output.

Surrounding and substrate are modeled as semi-infinite TLs characterized by a wavenumber (β_{in}, β_s, respectively) and a characteristic impedance per unit length (Z_{in}, Z_s, respectively), see circuit in Fig. 5.2(a). The wavenumbers in these two semi-infinite free spaces are given by:

$$\beta_u = k_u \cos\theta = k_0 n_u \cos\theta, \tag{5.2}$$

whereas the characteristic impedances are given by:

$$Z_u = Z_0 p \cos\theta / n_u, \tag{5.3}$$

where n_u is the refractive index with $u = in$ (input), s (substrate), k_0 the wavenumber in vacuum, $Z_0 = \sqrt{\mu_0/\epsilon_0}$ the vacuum impedance and p the period. (Here we only use the model for the normal incidence, so the emergence angle in the substrate is also equal to zero. Note that for the straight wall grating this model gives a good agreement with numerical simulations [19].)

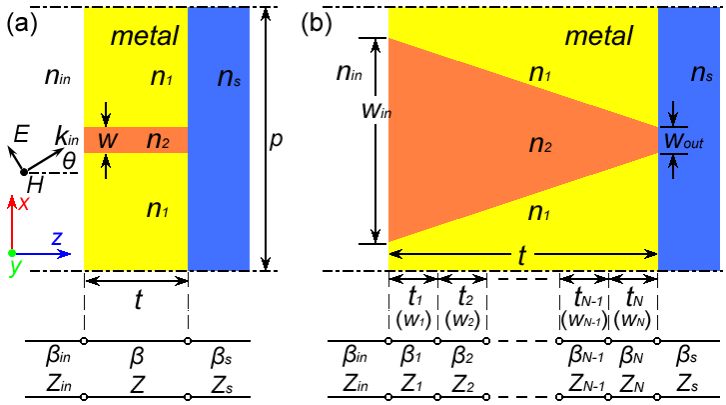

Figure 5.2: Schematics of 1D metallic grating with (a) straight slits, and (b) linearly tapered slits, respectively. Together with illustrations of the TL model underneath. The gratings are periodic in the x-direction. For a more general consideration the slit is filled with a medium with refractive index n_2.

The grating layer is treated as a TL characterized by β and Z with finite length t. Given that the metal width d ($= p - w$) is large enough to avoid coupling between slits, the wavenumber β is determined by the dispersion relation of a metal-insulator-metal waveguide [13]:

$$\tanh\left(\sqrt{\beta^2 - {k_0}^2 {n_2}^2}\, w/2\right) = -\frac{\sqrt{\beta^2 - {k_0}^2 {n_1}^2}\, {n_2}^2}{\sqrt{\beta^2 - {k_0}^2 {n_2}^2}\, {n_1}^2}, \tag{5.4}$$

which is the dispersion relation for the even mode in MIM (odd mode is not excited here). Then the characteristic impedance per unit length can be expressed as [19]

$$Z = \frac{w\beta}{\omega\epsilon_0}. \tag{5.5}$$

The tapered grating is modeled as a series of cascaded TLs, with a staircase multilayer characterized by local widths w_i and thicknesses t_i (circuit in Fig. 5.2(b)). For each multilayer section we can model it as a two-port network as above yielding cascaded two-port networks. To calculate the reflection R and transmission T of the cascaded network one can use *ABCD* parameters (also known as transfer matrix approach) [28]. The *ABCD* parameters (M) of the whole network are a multiplication of each TL in the network:

$$M = \begin{bmatrix} A_{tot} & B_{tot} \\ C_{tot} & D_{tot} \end{bmatrix} = \prod M_i = \prod \begin{bmatrix} A_i & B_i \\ C_i & D_i \end{bmatrix} \tag{5.6}$$

where

$$\begin{aligned} A_i &= D_i = \cos(\beta_i t_i), \\ B_i &= jZ_i \sin(\beta_i t_i), \\ C_i &= jY_i \sin(\beta_i t_i), \end{aligned} \tag{5.7}$$

with $Y_i = 1/Z_i$, $(i = 1, 2, \cdots, N)$. Therefore R and T are expressed respectively by:

$$R = \left| \frac{m_1 Y_{in} - m_2}{m_1 Y_{in} + m_2} \right|^2 \tag{5.8}$$

$$T = \frac{4|Y_{in}|^2 Re(Y_s)}{|m_1 Y_{in} + m_2|^2 Re(Y_{in})} \tag{5.9}$$

where $m_1 = A_{tot} + B_{tot} Y_s$, $m_2 = C_{tot} + D_{tot} Y_s$, $Y_u = 1/Z_u$, $u = in, s$.

Upon derivation of Eq. 5.5 uniform electric fields in the slit and negligible coupling between the slits is assumed [19], so the TL model works well with small slit widths (w) and large enough metal widths (d). In addition, diffraction in the surrounding and substrate, and surface modes at the grating planes are not considered in the TL model, so the period of the grating cannot be larger than the wavelength.

5.2.3 Results

Enhanced transmission

To start with illustrating the effects of tapering, here we assume surrounding, substrate and material in the slit to be air. Figure 5.3 shows the calculated

TM transmission T with normal incidence ($\theta = 0$) for grating structures with different sizes, with both FEM and TL calculations. For the gratings with straight sidewalls FP resonance peaks in (a) and (b) are observed almost at the same wavelengths. This indicates the peaks are mainly related to the size of the slits given that coupling between slits is small. Increasing thickness produces more peaks analogous to a FP cavity as shown in (c).

For various parameters, the tapered grating leads to a dramatic enhancement of the transmission over a broadband wavelength range, comparing the straight sidewall case (Fig. 5.3, blue curves) with the tapered cases. In addition, we notice that the tapered transmission seems to average the FP resonant peaks for the non-tapered geometry, leading to nonresonant transmission. This averaging effect is clear for the smaller wavelengths, and becomes more pronounced for larger w_{in} (more 'open' gratings). Although the averaging effect makes the peak transmission smaller by tapering, as a return a large transmission is available at wavelengths above the original resonance.

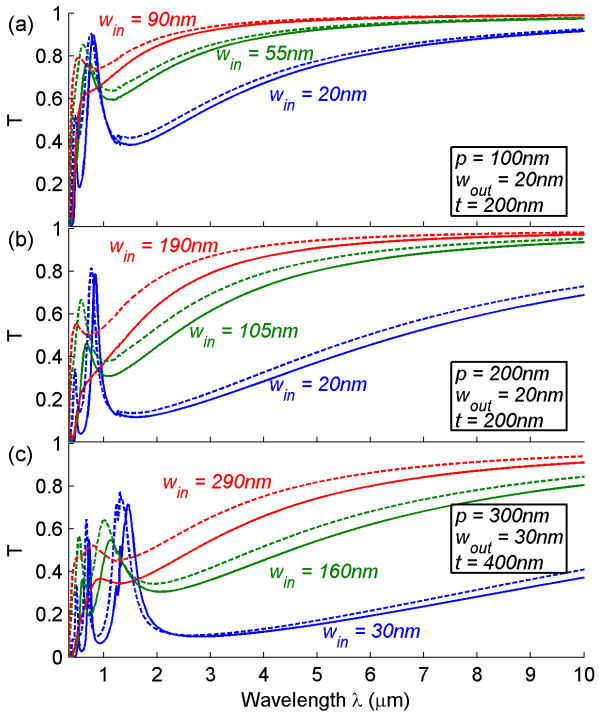

Figure 5.3: Transmission T for gratings with different sizes (i.e. different slit width w_{in} and w_{out}, grating period p, slit thickness t). The solid lines are from numerical simulation by FEM. The dashed lines are from the TL model.

The plots in Fig. 5.3 show a good agreement between the rigorous full-wave FEM simulations and the TL model. Here, in the TL model 10 layers are used and already provide a good convergence. More in detail, agreement is better for small periods (Fig. 5.3(a)), and for straight slits (blue curves in Fig. 5.3(a), (b) and (c)). The deviation is mainly caused by plasmon modes at the slit corners, which are not taken into account in the TL model. Deviation increases when w_{in} increases, since the coupling between slits becomes stronger, and uniformity of the E field in the slits diminishes. However, the TL model still predicts the trend of T very well, except for an overestimation at smaller wavelengths.

The increased transmission can be understood as the impedance at the entrance of the slit is much closer by tapering to the impedance in the input medium. Considering the impedance per unit length defined by Eq. 5.5, $Z = w\beta/(\omega\epsilon_0)$, obviously it can be tuned by the width w (β is also a function of w as seen in dispersion relation, Eq. 5.6). To illustrate figure 5.4 shows the normalized impedance per unit length in the slit to that in surrounding as a function of the distance away from the exit of slit for a wavelength of 5μm. It is clear that as the entrance is more open the impedance difference between the entrance of the slit and the surrounding becomes smaller. As a consequence more light is funneled.

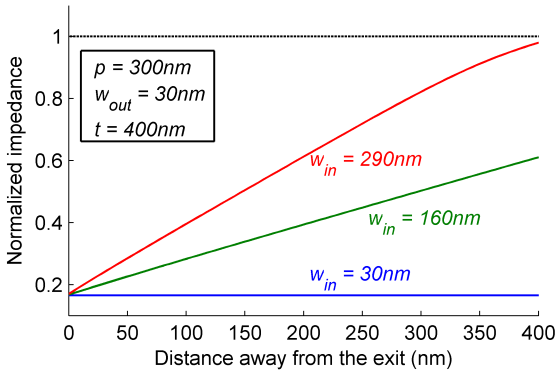

Figure 5.4: Normalized impedance in the slit as a function of the distance away from slit exit at $\lambda = 5\mu$m for different w_{out} with grating period $p = 300$nm, slit thickness $t = 400$nm, and $w_{in} = 30$nm. (Normalized to the impedance per unit length in the surrounding defined by Eq. 5.3.) Non-varying impedance for $w_{in} = 30$nm is due to the straight sidewall with constant width. For $w_{in} = 160$nm, and 290nm impedances increase towards the entrance, getting close to the impedance in surrounding.

Field enhancement

Based on the large transmission enhancement by tapering we can imagine that the light is slowly squeezed from the entrance of the taper on to the narrower exit slit. Therefore the field is expected to be gradually enhanced. To confirm we plot the electric field spatial distribution (Fig. 5.5) at wavelength 5μm for gratings corresponding to Fig. 5.3(b). For other grating sizes the field spatial distribution profiles are very similar. We notice indeed that the E amplitude gradually increases towards the exit of the slit by tapering, contrast (a) to (b) and (c). In addition, the fields reach their maximum exactly at the exit of the tapered slit, and the maximum value is much larger than in the straight sidewall case.

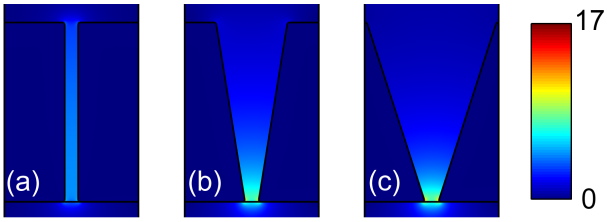

Figure 5.5: E field amplitude (normalized by the incident field amplitude E_0) distribution at $\lambda = 5\mu$m for gratings ($t = 400$nm, $w_{out} = 30$nm, $p = 300$nm) with (a) $w_{in} = 30$nm, (b) $w_{in} = 160$nm, (c) $w_{in} = 290$nm.

To examine the field enhancement properties Fig. 5.6 shows the average normalized electric field as a function of wavelength at the slit exit (same gratings as in Fig. 5.5). Broadband field enhancement is obtained, and it increases as the taper becomes wider (increasing w_{in}). Meanwhile the spectrum of the normalized field is similar to the corresponding transmission spectrum (Fig. 5.3(b)). The mechanism behind this is similar to EOT, light is coupled into SP modes before converting back to radiative light in free space [10, 29]. Therefore the near-field at the exit of the slit and the transmission have a similar spectrum, with deviations from evanescent wave components. In addition, for larger wavelengths we notice that the normalized electric field arrives quite close to the dash-dotted line, which is the ratio of p/w_{out}, similar to [20]. The average field decreases towards smaller wavelengths, since there is less light transmitted. However, by tapering it is still possible to obtain a local field enhancement far beyond the ratio of p/w_{out}, instigated by the sharp corner at the exit of the slit, as the field maxima show in Fig. 5.5. Therefore tapering offers a strong control over the field enhancement profile, by tailoring the transmission spectrum, the value of p/w_{out} and the corner sharpness.

Angular incidence response

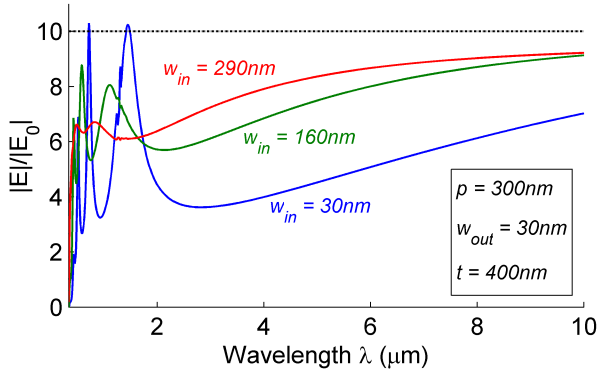

Figure 5.6: Average E field amplitude (normalized by the incident filed amplitude E_0) versus wavelength at the exit of slit for gratings (t = 400nm, w_{out} = 30nm, p = 300nm) with different widths: w_{in} = 30nm (blue), w_{in} = 160nm (green), and w_{in} = 290nm (red).

We compare the angular response of the straight sidewall gratings (Fig. 5.7(a)) with the tapered gratings (Fig. 5.7(b)). For the straight sidewall (Fig. 5.7(a)) we observe that the transmission gradually increases with the angle, and reaches its maximum near the dashed line around 80°, which is the brewster angle θ_B determined by impedance matching between the surrounding and the straight slit when [19]:

$$\cos\theta_B = \frac{\beta w}{k_0 p}. \tag{5.10}$$

This equation yields from equality between Eqs. 5.3 and 5.5 (impedance matching between the mode propagating in straight sidewall slit and light in the surrounding air) which is the requirement for no reflection, i.e. setting Eq. 5.8 to be zero.

For the tapered case (Fig. 5.7(b) and (c)) we see that the overall transmission is significantly larger, which benefits from the gradually reduced impedance towards the entrance. In addition, we still observe brewster angle behavior, i.e. the transmission increases with incident angle, as an extra impedance matching benefit by tilting the incident light.

Substrate influence

In experimental realizations a different substrate may be necessary. Our calculations show the validity of the tapering idea for $n_s \neq n_i$, except that the transmission at larger wavelength is determined by that of light through a semi-infinite surrounding and substrate according to Fresnel's law (T =

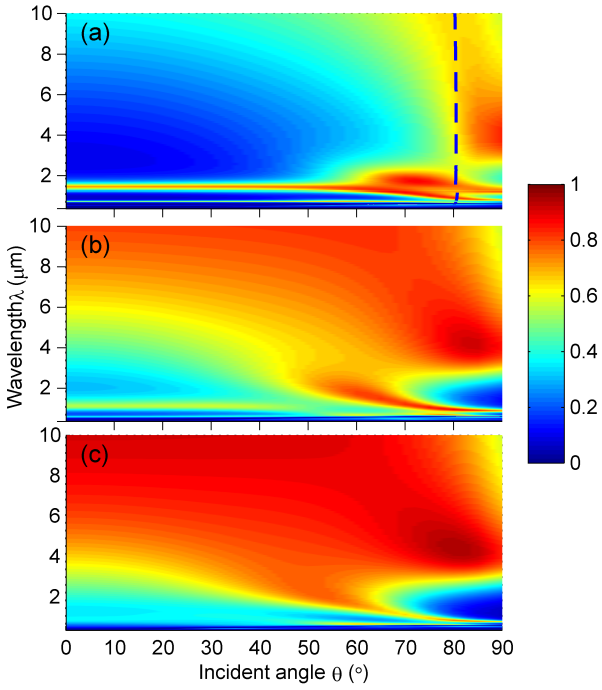

Figure 5.7: Angular response for gratings (t = 400nm, p = 300nm, w_{out} = 30nm) with (a) w_{in} = 30nm (straight sidewalls), (b) w_{in} = 160nm and (c) w_{in} = 290nm (tapered sidewalls). The dashed line in (a) is the plasmonic brewster angle.

$4n_s n_{in}/(n_s + n_{in})^2$). To illustrate Fig. 5.8 shows an example with the refractive index of substrate equal to 2 for a grating: p = 100nm, t = 200nm, w_{out} = 20nm. The transmission increases with increasing entrance slit width. Meanwhile the three transmission curves approach the dashed line, which is the transmission value between two semi-infinite free spaces.

5.3 2D gratings

In some applications, like photovoltaics, polarization independence is always desired. However for the 1D grating considered above, EOT is only observed under TM-polarized illumination. To make it independent from polarization we have to consider 2D gratings. Mimicking the 1D grating above, two different classes are produced, one is a metal film with hole array, the other is an array with some isolated metal (e.g. as depicted in Fig. 5.9). As introduced in section 5.1, there is always a cutoff wavelength for a single hole. Although peri-

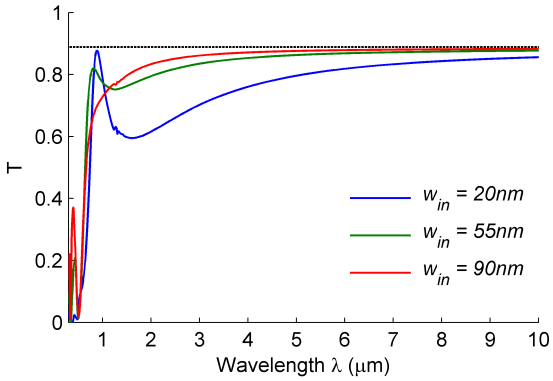

Figure 5.8: Transmission for gratings (t = 200nm, p = 100nm, w_{out} = 20nm) on a substrate with refractive index 2 with different w_{in} = 20nm, 55nm, and 90nm. The dashed line is transmission through an interface between air and a substrate with refractive index 2. The dashed line defines the maximum of the transmission via Fresnel reflection.

odicity will enhance the transmission at EOT peaks, from Eq. 5.1 one derives for the maximum peak positions λ

$$\lambda = \frac{p}{i^2 + j^2}\sqrt{\frac{\epsilon_m \epsilon_d}{\epsilon_m + \epsilon_d}} < p\sqrt{\epsilon_d} = n_d p, \tag{5.11}$$

so that the peaks will not appear for larger wavelengths, transmission will decrease. Therefore here we only give a 2D grating example without cutoff as shown in Fig. 5.9.

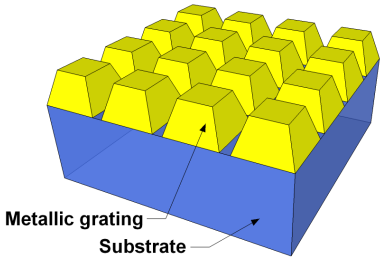

Figure 5.9: Schematics of 2D metallic grating with perpendicular tapered slits, which is insensitive to the light polarization.

Here we only consider normal incidence. The two directions of slits have the same size parameters as the 1D slits of the previous section. Only one polarization parallel to the slits is investigated because of the polarization insensitivity

under normal illumination. The simulation setup is similar to the 1D silver grating except that 3D models are used here. Figure 5.10 shows transmission T for 2D gratings with crossing slits with different sizes and substrates. It is clear that the tapering effects are still valid. Meanwhile the maximum transmission is also limited by the value through the interface between air and substrate.

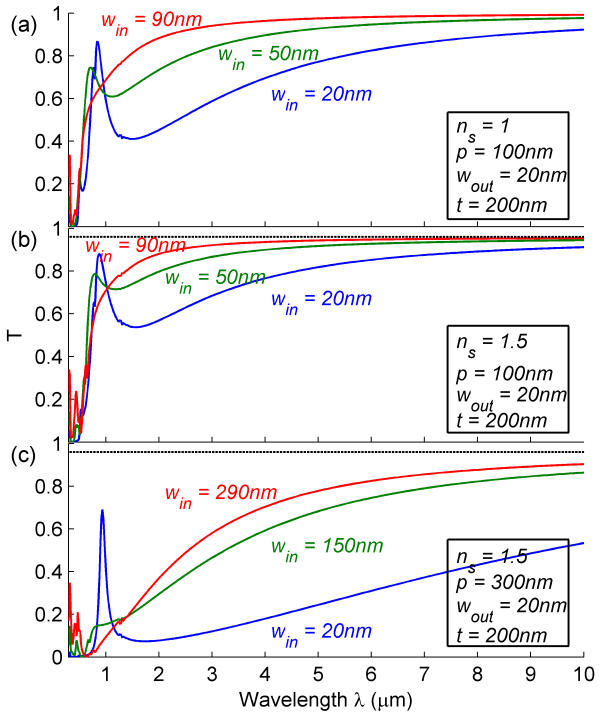

Figure 5.10: Transmission T for 2D gratings with crossing slits with different sizes and substrates (i.e. different slit width w_{in} and w_{out}, grating period p, slit thickness t, substrate refractive index n_s). (a) and (b) are the same gratings but with different substrates, $n_s = 1$ for (a), $n_s = 1.5$ (glass) for (b). The dashed lines in (b) and (c) are the limits imposed by Fresnel's law between air and glass.

5.4 Conclusion

In summary, we demonstrate the concept of tapering in metallic gratings to achieve broadband and wide-angle transmission. The broadband transmission can be explained by impedance matching between the tapered slit entrance and the surrounding. In addition, the taper provides a strong enhancement and lo-

calization of light at the exit of the slit, useful for applications such as nonlinear optics, light harvesting, sensing, emission enhancement etc. The TL model gives a very efficient characterization of the tapering effect, therefore it can be used to assist more complex designs, e.g. with parabolic shapes. The transmission at smaller wavelengths is further improved by tilting the incident light, giving rise to a plasmonic Brewster type effect. Finally we also demonstrate a polarization independent 2D grating with normally crossing slits, where the tapering effects are still valid.

References

[1] H. A. Bethe. *Theory of diffraction by small holes.* Physical Review, 66(7-8):163–182, 1944.

[2] T. W. Ebbesen, H. J. Lezec, H. F. Ghaemi, T. Thio, and P. A. Wolff. *Extraordinary optical transmission through sub-wavelength hole arrays.* Nature, 391(14):667–669, 1998.

[3] H. Ghaemi, T. Thio, D. Grupp, T. Ebbesen, and H. Lezec. *Surface plasmons enhance optical transmission through subwavelength holes.* Physical Review B, 58(11):6779–6782, 1998.

[4] L. Martín-Moreno, F. J. García-Vidal, H. J. Lezec, K. M. Pellerin, T. Thio, J. B. Pendry, and T. W. Ebbesen. *Theory of extraordinary optical transmission through subwavelength hole arrays.* Physical Review Letters, 86:1114–1117, 2001.

[5] K. J. K. Koerkamp, S. Enoch, F. B. Segerink, N. F. Van Hulst, and L. Kuipers. *Strong influence of hole shape on extraordinary transmission through periodic arrays of subwavelength holes.* Physical Review Letters, 92(18):183901, 2004.

[6] K. L. Van der Molen, K. J. K. Koerkamp, S. Enoch, F. B. Segerink, N. F. Van Hulst, and L. Kuipers. *Role of shape and localized resonances in extraordinary transmission through periodic arrays of subwavelength holes: experiment and theory.* Physical Review B, 72(4):045421, 2005.

[7] A. Degiron and T. W. Ebbesen. *The role of localized surface plasmon modes in the enhanced transmission of periodic subwavelength apertures.* Journal of Optics A: Pure and Applied Optics, 7(2):S90–S96, 2005.

[8] J. Porto, F. García-Vidal, and J. Pendry. *Transmission resonances on metallic gratings with very narrow slits.* Physical Review Letters, 83(14):2845–2848, 1999.

[9] Q. Cao and P. Lalanne. *Negative role of surface plasmons in the transmission of metallic gratings with very narrow slits.* Physical Review Letters, 88(5):3–6, 2002.

[10] X. R. Huang, R. W. Peng, and R. H. Fan. *Making metals transparent for white light by spoof surface plasmons.* Physical Review Letters, 105(24):1–4, 2010.

[11] F. Yang and J. Sambles. *Resonant transmission of microwaves through a narrow metallic slit.* Physical Review Letters, 89(6):5–7, 2002.

[12] J. Suckling, A. Hibbins, M. Lockyear, T. Preist, J. Sambles, and C. Lawrence. *Finite conductance governs the resonance transmission of thin metal slits at microwave frequencies.* Physical Review Letters, 92(14):1–4, 2004.

[13] E. N. Economou. *Surface plasmons in thin films.* Physical Review, 182:539–554, 1969.

[14] A. G. Brolo, E. Arctander, R. Gordon, B. Leathem, and K. L. Kavanagh. *Nanohole-enhanced Raman scattering.* Nano Letters, 4(10):2015–2018, 2004.

[15] A. G. Brolo, R. Gordon, B. Leathem, and K. L. Kavanagh. *Surface plasmon sensor based on the enhanced light transmission through arrays of nanoholes in gold films.* Langmuir, 20(12):4813–4815, 2004.

[16] R. Gordon, D. Sinton, K. L. Kavanagh, and A. G. Brolo. *A new generation of sensors based on extraordinary optical transmission.* Accounts of Chemical Research, 41(8):1049–1057, 2008.

[17] M. Schnell, P. Alonso-González, L. Arzubiaga, F. Casanova, L. E. Hueso, A. Chuvilin, and R. Hillenbrand. *Nanofocusing of mid-infrared energy with tapered transmission lines.* Nature Photonics, 5:283–287, 2011.

[18] H. A. Atwater and A. Polman. *Plasmonics for improved photovoltaic devices.* Nature Materials, 9:205–214, 2010.

[19] A. Alù, G. D' Aguanno, N. Mattiucci, and M. Bloemer. *Plasmonic brewster angle: broadband extraordinary transmission through optical gratings.* Physical Review Letters, 106(12):1–4, 2011.

[20] G. Subramania, S. Foteinopoulou, and I. Brener. *Nonresonant broadband funneling of light via ultrasubwavelength channels.* Physical Review Letters, 107(16):1–5, 2011.

[21] T. Søndergaard, S. I. Bozhevolnyi, S. M. Novikov, J. Beermann, E. Devaux, and T. W. Ebbesen. *Extraordinary optical transmission enhanced by nanofocusing.* Nano Letters, 10(8):3123–8, 2010.

[22] J. Beermann, T. Søndergaard, S. M. Novikov, S. I. Bozhevolnyi, E. Devaux, and T. W. Ebbesen. *Field enhancement and extraordinary optical transmission by tapered periodic slits in gold films.* New Journal of Physics, 13(6):063029, 2011.

[23] T. Søndergaard, S. I. Bozhevolnyi, J. Beermann, S. M. Novikov, E. Devaux, and T. W. Ebbesen. *Extraordinary optical transmission with tapered slits: effect of higher diffraction and slit resonance orders.* 29(1):130–137, 2012.

[24] Comsol Multiphysics. *http://www.comsol.com.*

[25] E. D. Palik. *Handbook of Optical Constants of Solids.* Academic, New York, 1985.

[26] F. Medina, F. Mesa, and R. Marqués. *Extraordinary transmission through arrays of electrically small holes from a circuit theory perspective.* IEEE Transactions on Microwave Theory and Techniques, 56(12):3108–3120, 2008.

[27] V. Delgado and R. Marqu. *Surface impedance model for extraordinary transmission in 1D metallic and dielectric screens.* Optics Express, 19(25):25290–25297, 2011.

[28] D. M. Pozar. *Microwave Engineering.* J. Wiley, 12005.

[29] W. L. Barnes, A. Dereux, and T. W. Ebbesen. *Subwavelength optics.* Nature, 424:824–830, 2003.

6

Conclusions and perspectives

6.1 Conclusions

Metallic nanostructures have the ability to concentrate and manipulate light at the nanoscale. In this work we have investigated the potential of using metallic nanostructures to boost light harvesting in OSCs.

We performed systematic numerical studies on the effects of small particles in absorbing devices. To take advantage of the dipolar localized plasmon mode in metallic nanoparticles, it is better to embed them directly in the active layer, since the scattering effects of small particles are negligible. Based on a 2D model for organic solar cells with metallic nanowires, we analyzed the influence of particle spacing and size. With optimized size and density a best enhancement factor around 1.56 for absorption (from 30% to 47%) and 1.63 for current density (from 6.7mA/cm^2 to 10.9mA/cm^2) is achievable, bringing the thin solar cell close to the performance of a much thicker cell without nanowires. Enhancement is mainly due to the near-field enhancement concomitant with the localized plasmon mode excitation. Meanwhile, the interaction between nanowires has a strong influence on the near-field mode profile. To avoid direct contact between metal and the active material, a coating buffer will be needed. We noticed that a silica coating strongly declines the absorption enhancement as the coating thickness increases. However other researchers have shown that this may be alleviated by using a higher index coating material [1].

Since metallic nanowires are sensitive to the polarization of light (LSP mode can only be excited with TM polarization), we studied 2D particle arrays embedded in the active layer, resulting in significant absorption and current density enhancements. Material studies for the spherical particles concluded that Al and Ag provide comparable absorption and current density enhancements. In contrast, Au particles give a small enhancement; its localized plasmon is excited at larger wavelengths, and one observes large losses in the particles due to interband transitions. Experiments carried out by colleagues at imec with small molecules (CuPc and SubPc) have confirmed that the near-field enhancement of small Ag particles boosts the light harvesting, in agreement with our simulations.

Many experiments in the literature have particles embedded in the buffer layer (PEDOT:PSS), next to the active layer. From the viewpoint of optics, our studies point to a reduction in absorption, instead of an efficiency enhancement observed in some experiments. Therefore these enhancements with particles in a buffer layer should be attributed to electronic effects, and various experiments point to similar findings.

We also demonstrated the feasibility of scattering by larger MNPs to enhance the efficiency of OSCs. We introduced Ag NP arrays with a square lattice on top of OSCs. Light can be effectively trapped inside the active layer, improving the light harvesting. Further improvement can be achieved by filling the space between particles in the NP array with a medium.

Another aspect associated with metallic nanostructures is the excitation of surface modes, which also provides pathways ways for extra light harvesting. We investigated the influence of combined 1D gratings, composed of both front and back gratings, on the absorption in the active layer of OSCs. To achieve a superposition of contributions from front and back gratings we introduced a half period offset between the gratings. The modes in these devices are of mixed character, comprising both localized and propagating properties. With an optimal period and grating geometry, enhancement factors of 1.35 and 1.42 are respectively reached for absorption and current density enhancements for TM polarized normal incident light. Two different kinds of Bloch modes, namely bright and dark modes (symmetrical versus asymmetrical magnetic field profile), exist in the grating structures due the periodicity. The dark mode can only be excited with tilted incident light, which leads to a mechanism for absorption over a larger angular range. The absorption and current density enhancements are boosted further with tilted incident light around 10°. Furthermore, we found that with TE polarized light the combined gratings do not decrease the observed enhancement strongly. Finally, we also performed investigations on 2D Ag nanodisk arrays in the buffer layer, to obtain a polarization insensitive structure. A considerable current density enhancement factor around 1.21 was observed.

To further explore nanostructured electrodes, we studied metallic gratings with tapered openings. There are always modes available in slits with straight sidewalls, however these often lead to narrow Fabry-Perot type resonances. By tapering the slits we observe a broadband and wide-angle transmission, which is attributed to impedance matching between the tapered slit entrance and the surrounding, and is efficiently described by a transmission line model. In addition, the taper provides a strong enhancement and localization of light at the exit of the slit, useful for applications such as nonlinear optics, light harvesting, sensing, emission enhancement etc. The transmission at smaller wavelengths is further improved by tilting the incident light, giving rise to a plasmonic Brewster type effect. Finally, we demonstrated these tapering ideas in a polarization independent 2D grating with normally crossing slits.

6.2 Perspectives

In this work theoretical studies have shown the promise of incorporating metallic structures into solar cell devices. However, the required nanoscale precision makes fabrication difficult to control.

For the use of particles for light harvesting, somewhat easier geometries to fabricate should be considered in future work. One possible way is to employ the particles as scatterers at the front or back, leading to larger sizes which are necessary for prominent scattering. We have demonstrated this configuration in chapter 3 by introducing large NP arrays on the top surface of OSCs, however the enhancement factor is still not optimized completely. Meanwhile there are still other shapes of particles not yet investigated here. These configurations have been investigated in silicon thin-film solar cells with considerable light harvesting improvement [2–4]. However, for this kind of thin-film cells the active layer thickness is usually not smaller than 300nm, thus scattered light can be coupled to the guided modes in the layer structure. For organic solar cells one needs a thinner layer thickness, and one is confronted with a lower refractive index reducing the amount of guided modes. In the end, strongly confined plasmonic light enhancement will become useful when very thin organic layers are considered, which is for current fabrication methods still state-of-the-art or beyond. We remark also that the electronic properties of metallic nanostructures inside solar cells offer another pathway for future research and optimization.

Other promising configurations could employ the hybrid element approach, like the combined gratings we proposed. Indeed, combining benefits at various wavelength ranges from different structures would further boost the overall light harvesting, leading closer towards the ultimate device absorption.

Non-resonant devices, such as the tapered structures, present a comple-

mentary, and less studied, approach to enhance the light-matter interaction. Instead of adding resonances to the spectrum, here one aims to have a relatively feature-less, but broadband response, which is achievable in selected geometries, and still needs further investigation.

References

[1] J. Y. Lee and P. Peumans. *The origin of enhanced optical absorption in solar cells with metal nanoparticles embedded in the active layer.* Optics Express, 18(10):10078–87, 2010.

[2] Y. A. Akimov, W. S. Koh, and K. Ostrikov. *Enhancement of optical absorption in thin-film solar cells through the excitation of higher-order nanoparticle plasmon modes.* Optics Express, 17(12):10195–205, 2009.

[3] Y. A. Akimov and W. S. Koh. *Design of Plasmonic Nanoparticles for Efficient Subwavelength Light Trapping in Thin-Film Solar Cells.* Plasmonics, 6(1):155–161, 2010.

[4] F.-J. Tsai, J.-Y. Wang, J.-J. Huang, Y.-W. Kiang, and C. C. Yang. *Absorption enhancement of an amorphous Si solar cell through surface plasmon-induced scattering with metal nanoparticles.* Optics Express, 18(102):A207–20, 2010.